The Effects of Implant-Associated Tissue Reactions on Implantable Glucose Sensor Performance

by

Matthew Thomas Novak

Department of Biomedical Engineering
Duke University

Date:_____

Approved:

_____
William M. Reichert, Supervisor

_____
Fan Yuan

_____
David F. Katz

_____
Charles S. Wallace

_____
Mark H. Schoenfisch

Dissertation submitted in partial fulfillment of
the requirements for the degree of Doctor
of Philosophy in the Department of
Biomedical Engineering in the Graduate School
of Duke University

2014

ABSTRACT

The Effects of Implant-Associated Tissue Reactions on Implantable Glucose Sensor Performance

by

Matthew Thomas Novak

Department of Biomedical Engineering
Duke University

Date:_____
Approved:

_____
William M. Reichert, Supervisor

_____
Fan Yuan

_____
David F. Katz

_____
Charles S. Wallace

_____
Mark H. Schoenfisch

An abstract of a dissertation submitted in partial fulfillment of the requirements for the degree of Doctor of Philosophy in the Department of Biomedical Engineering in the Graduate School of Duke University

2014

Abstract

As an increasingly prevalent chronic disease, diabetes represents one of the fastest growing health burdens to both the developed and developing world. In an effort to improve the management and treatment of diabetes, implantable sensors that continuously monitor glucose levels have become popular alternatives to patient-administered finger prick measurements of blood glucose. However, following implantation, the performance of these implants suffers from inaccurate and erratic readings that compromise their useful lives. As a result, implantable glucose sensors remain limited as a platform for the reliable management of diabetes. While the interaction between the sensor and its surrounding tissue has been posited as a culprit for erroneous *in vivo* sensor performance, there remains little evidence to support that theory.

This dissertation describes the effects that implant-associated tissue reactions have on implantable sensor function. Since tissue response to an implant changes over time, the overall effect of these tissue reactions is broken into two temporal phases: (1) the phase of weeks to months following implantation when a mature foreign body capsule is present around the sensor and (2) the phase of days to weeks immediately following sensor implantation when a provisional matrix of proteins and inflammatory cells envelops the sensor.

Late stage sensor responses to implantation are marked by both an attenuated sensor signal and a significant time lag relative to blood glucose readings. For this later stage of sensor response, a computational model of glucose transport through the interstitial space and foreign body capsule was derived and implemented. Utilizing physiologically relevant parameters, the model was used to mechanistically study how each constituent part of the capsular tissue could affect sensor response with respect to signal attenuation and lag. Each parameter was then analyzed using logarithmic sensitivity analysis to study the effects of different transport variables on both lag and attenuation. Results identified capsule thickness as the strongest determinant of sensor time lag, while subcutaneous vessel density and capsule porosity had the largest effects on attenuation of the sensor signal.

For the phase of early stage tissue response, human whole blood was used as a simple *ex vivo* experimental system. The impacts of protein accumulation at the sensor surface (biofouling effects) and cellular consumption of glucose in both the biofouling layer and in the bulk (metabolic effects) on sensor response were assessed. Medtronic Minimed SofSensor glucose sensors were incubated in whole blood, plasma diluted whole blood, and cell-free platelet poor plasma (PPP) to analyze the effects of different blood constituents on sensor function. Experimental conditions were then simulated using MATLAB to predict the relative impacts of biofouling and metabolic effects on the observed sensor responses. It was found that the physical barrier to glucose transport

presented by protein biofouling did not hinder glucose movement to the sensor surface. Instead, glucose consumption by inflammatory cells was identified as the major culprit for generating poor sensor performance immediately following implantation.

Lastly, a novel, biomimetic construct was designed to mimic the *in vivo* 3D cellular setting around the sensor for the focused *in vitro* investigation of early stage effects of implantation on glucose sensor performance. Results with this construct demonstrate similar trends in sensor signal decline to the *ex vivo* cases described above, suggesting this construct could be used as an *in vitro* platform for assessing implantable glucose sensor performance.

In total, it may be concluded from this dissertation that instead of sensors "failing" *in vivo*, as is often reported, that different physiological factors mediate long term sensor function by altering the environment around the implant. For times immediately following implantation, sensor signals are mediated by the presence of inflammatory macrophages adhered on the surface. However, at longer times post-implantation, sensor signals are mediated not by the consumptive capacity of macrophages, but instead by the subcutaneous vessel density surrounding the sensor as well as the porosity and thickness of the foreign body capsule itself. Taken in concert, the results of this dissertation provide a temporal framework for outlining the effects of tissue response on sensor performance, hopefully informing more biocompatible glucose sensor designs in the future.

To my father, Thomas, and my mother, Debra.

Contents

List of Tables

List of Figures

List of Abbreviations

LPS – Lipopolysaccharide

PMA - Phorbol Myristate Acetate

PRP-Platelet Rich Plasma

PPP-Platelet Poor Plasma

FBC-Foreign Body Capsule

FDA-Food and Drug Administration

PBS-Phosphate Buffered Saline

VEGF – Vascular Endothelial Growth Factor

ROS – Reactive Oxygen Species

RNS – Reactive Nitrogen Species

DMEM – Dulbecco's Modified Eagle's Medium

2-NBDG - 2-[N-(7-nitrobenz-2-oxa-1,3-diazol-4-yl) amino]-2-deoxy-D-glucose

TNF-α – Tumor Necrosis Factor Alpha

IFN-γ – Interferon Gamma

IL-1 – Interleukin 1

IL-4 – Interleukin 4

IL-10 – Interleukin 10

IL-13 – Interleukin 13

IL-23 – Interleukin 23

H&E – Hematoxylin and Eosin

SEM – Scanning Electron Microscopy

ECM – Extracellular Matrix

ANCOVA – Analysis of Covariance

Acknowledgements

It's been said that it takes a village to raise a child. If those ballpark numbers are correct and it does indeed take a village to raise a child, then it probably takes a midsize metropolitan area to raise a graduate student…or at least this graduate student. This acknowledgements section is as close as I'll ever come to an Academy Awards thank you speech and though I will never get a nice gold statue for my efforts on glucose sensors, at least I know I won't be cut off mid-sentence. So, to quote assistant greenskeeper, Carl Spackler, "I got that goin' for me…which is nice."

I've been a student here at Duke my entire adult life and, in that time, the rolodex of people who should share in this degree with me could fill the lengths of this dissertation and then some.

My dissertation committee deserves recognition for giving me a surplus of positive feedback and valuable recommendations. A special thanks to my advisor, Monty Reichert, for taking a chance on me. Thanks also to Fan Yuan, for being an accessible resource and helpful mentor. Lastly, thanks to David Katz, a polymath and true scholar who has always treated me as though I was his student and provided me with unwavering support and guidance.

An inestimable thank you to the old timers…Rob Schutte, Charles Anamelechi, and Steve Wallace. These people can still remember a clean shaven Monty, a nine team

ACC, and the very day that I decided I was becoming one of them by going to graduate school. With a dose of good humor, you taught me the right way to do things, and for that, I'll be forever grateful.

To the Katz lab…Marcus Henderson, Jenny Peters, Mike DeSoto, Bonnie Lai and Anthony Geonnotti. When I showed up on my first day in grad school without a desk, you provided me with one and allowed me to overstay my welcome for over two years. Despite being an interloper, you all took me in and treated me as though I was a member of the lab. In a field where people cavalierly apply the term "engineering" to anything they do, the Katz lab defines what real biomedical engineering is.

To Rob Kirkton…singularly one of the great people I'll ever have the pleasure to meet. A guy who, despite the otherworldly expectations heaped upon him, always, always, always has time to lend an encouraging word or a helpful hand to a friend. A guy who, in a department of self-promoters, is humble despite his laundry list of accomplishments. And a guy who can quote every single line of "Caddyshack."

To Alice Brochu, Andy Simnick, Nima Badie, Luke McSpadden, John Stroncek, Neil Terry, Sarah MacEwan, Mark Juhas, Chris Grigsby, Andy Adler, Stephanie Eyerly, Ryan Hill, Adrienne Blount and Stuart Webb, for being fantastic colleagues and even better friends.

To Kathy Barbour, Joyce Franklin, Susan Story, Kristen Rivers, and Ned Danieley for keeping this department running on a daily basis while being able to answer any and all questions with a smile.

To Stuart, Shirley and Jeffrey, the familiar faces of the CIEMAS building who have always been able to bring cheer to my day.

To my girlfriend, Caslin Gilroy, who is a superlative personified. You are the most generous, patient, gracious, kind and caring person I've ever met. The last two years that I have known you have been by far the happiest of my life. To paraphrase Clark W. Griswold in "National Lampoon's Christmas Vacation", if the next chapter of our life together is half as good as this one's been, I think we're all in for a big treat. I love you and look forward to everything we will share together.

To my brother, Gregory, the toughest, as well as funniest person I have ever, or will ever, come across. Whether it's playing me a riff of a Dire Straits song or just shooting the breeze, you've always been able to put me in a good frame of mind.

To the original doctors in the family: my mother, Debra, and my father, Thomas. You have always supplied me with a seemingly endless amount of encouragement. Everything I am and everything I've accomplished is a direct consequence of your sacrifices and efforts as parents. Thank you.

.

Chapter 1. Research Objectives

1.1 Significance of Research

There has been a significant thrust in the diabetes management community to create a viable, long term, continuously measuring glucose sensor to improve patient point of care. In order to achieve these continuous measurements, the majority of designs have revolved around implantable platforms. However, both the biocompatibility of these implants and the subsequent tissue effects on sensor performance have not been well characterized. While it has been accepted in the parlance of the diabetes community to state that sensors fail when implanted, a growing body of research suggests that instead of sensors actually failing, that tissue interactions with the indwelling sensor may inhibit local sensing capabilities. This dissertation will address the modes with which tissue reactions to implantation affect sensor response. Specifically, we will examine two different scenarios: (1) the effect of a mature foreign body capsule surrounding the sensor (late stage tissue response) and (2) the effect of early stages of implant-associated inflammation upon sensor function (early stage tissue response).

Both stages are of interest in improving long term sensor viability within the body. An increased awareness of long term tissue effects on sensor functionality will inform more rational surface designs for combating foreign body encapsulation. Similarly, as the useful clinical life of these sensors is frequently less than one week

when implanted, it is instructive to assess what early stage biological processes within that time window are affecting the local milieu, thereby limiting sensor capability *in vivo*. Because each stage has a different geometry and biological components, they are considered separately in how they impact sensor response.

To assess how these early and late stage tissue responses will affect the local sensing environment, we will examine the interaction between the sensor and implantation tissue through both computational and experimental models, ultimately presenting an *in vitro* construct for assessing sensor biocompatibility for improved *in vivo* performance. The specific aims of this dissertation are as follows:

1.2 Specific Aims

1.2.1 Specific Aim 1: Numerical Characterization of the Influences of Late Stage, Fully Formed Capsular Tissue on Implanted Glucose Sensor Function

As the long term tissue effects to sensor implantation have a stable number of components and geometry, they can be numerically modeled. A computational transport model of diffusion of glucose out of surrounding capillaries and through fully formed capsular tissue will be constructed to assess which aspects of the tissue contribute most to a depleted sensor response and increased time lag. Physiologically relevant values of capsule diffusion coefficient, capsule porosity, cellular glucose consumption, capsule thickness and subcutaneous vessel density will be used as inputs to create simulated sensor traces that mimic experimental instances of time lag and

signal attenuation for a given blood glucose profile. Once the model is constructed and validated, it will be run for a range of values for each of the above parameters, and using logarithmic sensitivity analysis, the relative contributions of each parameter in affecting sensor lag and attenuation will be calculated. With this model, it is hypothesized that decreased long term sensor response as manifest through increases in lag time and signal attenuation are promoted by the effects of inflammation/wound healing vis-à-vis the formation of a foreign body capsule.

1.2.2 Specific Aim 2: Characterization of the Early Stage Effects of Implantation on Glucose Sensor Performance

The environment immediately surrounding an implanted sensor contains both fouling protein layers as well as metabolically active inflammatory cell types like neutrophils and macrophages, all of which have been purported as potential culprits in affecting acute sensor response. Using commercially available Medtronic Minimed SofSensor implantable glucose sensors, we will recreate early tissue/sensor interactions *in vitro* by incubating sensors in whole blood as well as different constituents of whole blood, such as platelet poor plasma. Reported sensor trends will be corroborated by secondary blood glucose measurements to offer concrete observations of how glucose concentrations change during the period of sensor incubation. Additionally, a computational model of glucose transport through initial inflammatory tissue will present further evidence of how these early tissue responses will affect sensor performance. It is hypothesized that the presence of blood constituents such as

inflammatory macrophages proximal to the sensor surface create a depleted environment for glucose sensing via the consumption of glucose, rendering the detection ability of the glucose oxidase enzyme useless.

1.2.3 Specific Aim 3: Development of a Novel Biomimetic Construct of the *In Vivo* 3D Cellular Setting around the Sensor for the Focused *In Vitro* Investigation of Early Stage Effects of Implantation on Glucose Sensor Performance

To further investigate the role that the presence of adhered inflammatory macrophages on the sensor surface has on sensor function soon after implantation, we propose the construction of a novel biomimetic construct that accurately recapitulates the *in vivo* 3D protein and cellular milieu around the sensor. To make this construct as physiologically relevant as possible, it will be comprised of fibrin, which is the primary component of the protein biofouling layer that adsorbs to implanted sensors *in vivo.* Macrophages will be embedded into the gel at a concentration similar to concentrations observed around implants *in vivo*. These constructs will then be subsequently wrapped around otherwise functioning sensors to analyze the effects of adhered inflammatory cell presence on sensor performance. To ensure that any decrease in signal is a function of cell-mediated uptake of glucose, sensors surrounded by macrophage-embedded gels will be compared against readings of both bare sensors and sensors surrounded by acellular gels. To examine how activation of macrophages into pro-inflammatory phenotypes will impact sensor output, macrophages will be stimulated with both lipopolysaccharide (LPS) and phorbol myristate acetate (PMA). Experimental results of

sensor decline will be compared against those of a computational model of the experimental setup to ensure that the observed trends can be reasonable predictors of sensor performance. If successful, this *in vitro* system could serve as a robust and useful method to investigate the functional effects of implantation on not only glucose sensors, but any implantable biosensor.

1.3 Organization and Presentation of Dissertation

The objective of this dissertation is to analyze the impacts of both short and long term tissue reactions to implantation on glucose sensor function. Chapter 3 focuses exclusively on the effects that long term tissue reactions to implantation will have on sensor function. Chapter 4 details an *ex vivo* system for evaluating the effects that short term tissue reaction will have on sensor function. Building on the findings of Chapter 4, Chapter 5 features the design and characterization of a novel biomimetic system that can recapitulate the *ex vivo* results of the previous chapter for the assessment of glucose sensor performance. Finally, Chapter 6 summarizes the current findings and suggests future avenues for continuing this research.

Chapter 2: Background

2.1 Disease Burden of Diabetes and the Role of Implantable Glucose Sensors in Improved Disease Management

According to Center for Disease Control estimates from 2011, 25.8 million Americans have diabetes. Of this group, over 200,000 people die each year due to disease-related complications, making diabetes the seventh leading cause of death in the United States [1]. Those afflicted also live with an increased risk of heart disease, stroke, high blood pressure, blindness, kidney failure and neurological disorders [1]. Additionally, the disease represents a significant strain on health care, as the American Diabetes Association estimates that indirect and direct costs due to diabetes totaled over $174 billion in 2007 [2]. Both at home and clinically, one method for minimizing diabetes related pathologies is the constant management of blood glucose changes. The most traditional method for the monitoring of blood glucose levels is the "finger prick" technique, though reports have shown that only 30% of type 1 diabetics and 20% of type 2 diabetics on insulin treatment check blood glucose levels more than once a day [3].

Given both the insufficient adherence to glucose monitoring suggestions and the inability for the finger prick method to identify rapid hyperglycemic events, there exists the need for continuous glucose sensors. Ultimately, the hope of continuous sensors is that they will be able to interface with external insulin pumps, thereby creating a feedback loop that will supply insulin in real time based upon a patient's current blood

glucose levels. Continuous invasive routes for glucose measurement have already been introduced to the public market by companies like Medtronic and Cygnus.

While current invasive glucose sensor technology has shown both high selectivity and sensitivity, obstacles still exist in making it a viable option in a clinical setting. The Food and Drug Administration (FDA) has yet to approve invasive technologies for longer than a week. Medtronic's current measurement paradigms, the implantable REAL-Time™ system and the new MiniMed 530G system, have only been approved for three day and six day use by the FDA, respectively [4-7]. Similarly, sensing designs from Abbott Labs and DexCom have only been approved for five and seven days, respectively [6, 7]. While failure of the sensor itself may contribute to such a short working life, an increasing body of research has suggested that interaction between the implanted tissue and the sensor is the main culprit in short sensor life [8-13].

2.2 Tissue Response to Implanted Objects

In order to develop a sensor that can measure analyte concentrations with high sensitivity for a prolonged amount of time, the interaction between the sensor and the surrounding tissue must be considered. Once implanted, no sensor will exist as an inert object in the body since all implants will alter the surrounding environment. However, minimizing the effects of the sensor on the tissue will reduce errors associated with

inflammation. A more thorough account of tissue response to implanted materials is presented by Anderson [14].

When a foreign body is implanted, there will be injury to vascularized tissue. With this injury comes the exudation of blood borne proteins, fluid and cells to the site of implantation. The convection of blood borne proteins induces an initial coagulation cascade where fibrin is formed from the cleavage of fibrinogen by thrombin. This fibrin network will then coalesce around the implant to form a provisional matrix or biofouling layer. In addition to the fibrin skeleton, the provisional matrix contains a number of different factors that contribute to the formation of an inflammatory response. First, it contains adhesive molecules such as fibronectin and thrombospondin that will allow for inflammatory cell attachment and migration. Secondly, the provisional matrix contains a number of cytokines and growth factors that will coordinate the extent and pace of immune reaction [14]. These glycoproteins establish chemotactic gradients within the matrix that attract inflammatory cells to the site of injury. Binding of cytokines to specific cellular membrane receptors triggers second messenger cascades that immediately induce alterations in gene expression and eventually affect cellular behavior.

Once the biofouling layer has been established, inflammatory cells, guided by chemotactic gradients, changes in vascular flow, and the presence of adhesion molecules, will begin to infiltrate the site of inflammation. Neutrophils will initially

interrogate the injured tissue and attempt to phagocytose the implanted sensor. However, given the size of implants relative to cells, neutrophils will recruit macrophages to the site of injury to attempt phagocytosis. Additionally, macrophages will release cytokines, chemokines and growth promoting factors to encourage the recruitment of even more cell types. If neutrophils and macrophages cannot dispose of the foreign body, fibroblasts will migrate to the injury via the release of cytokines by macrophages. Fibroblasts generate collagen and proteoglycans to deposit around the site of injury. The extracellular matrix constituents produced by these cells forms the basis for the foreign body capsule. This capsule will grow in both size and density as the chronic inflammatory process persists. Figure 1 presents an idealized time course for tissue effects to sensor implantation.

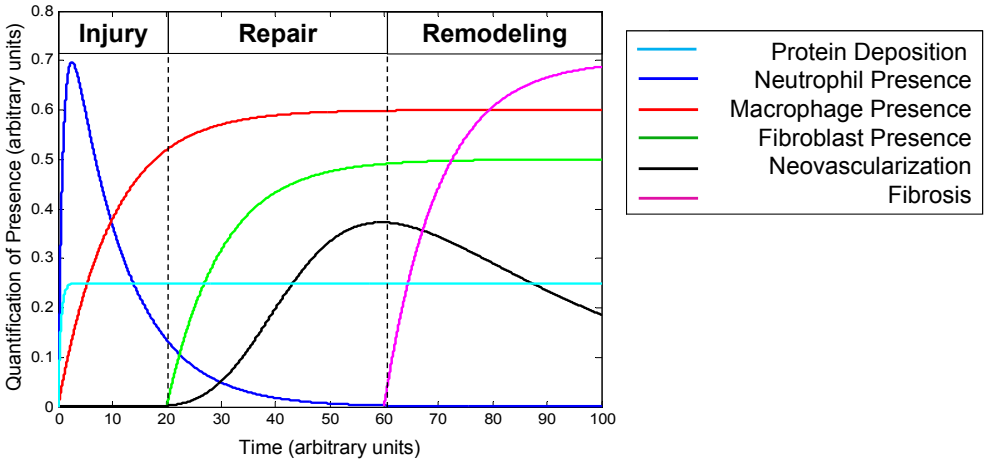

Figure 1: Idealized time course of tissue response to implantation

2.3 Effects of the Foreign Body Capsule on Implanted Sensor Performance

The foreign body capsule has long been considered to be a main cause for the short *in vivo* shelf life of implantable sensors [8, 12, 15]. Many have postulated different possible effects that the foreign body capsule would have upon sensor performance. Capsular tissue has been posited to decrease sensor effectiveness in many different ways, depending on its stage of development. Fully developed and well defined capsular tissue has been thought to decrease sensor function through the presence of underdeveloped microvascular networks for limited glucose delivery, local analyte consumption by metabolically active inflammatory cells, and decreased diffusion through the dense, collagen-rich capsule [13, 16-18]. A growing body of research has also investigated the ways in which early stage tissue response affects sensors as well. Table 1 outlines the different methods by which tissue effects are hypothesized to affect sensor function. As such, researchers have developed different surface treatments to avoid specific aspects of the inflammatory process. Examples include the following: 1.) coating surfaces in materials that resist protein adsorption such as Nafion, surfactants, and hydrogels, 2.) controlled release of anti-inflammatory therapeutics and growth factors such as VEGF, dexamethasone and nitric oxide, to steer the tissue to a more stable state and 3.) development of textured surfaces that will encourage angiogenesis proximal to the sensor [9, 17, 19, 20].

Table 1: Methods by which tissue response could alter sensor behavior

Proposed Effect	Description	Citation
Short Term (<1 week post-implantation)		
Formation of provisional matrix	Coagulation cascade induces the formation of fibrin matrix clots. These clots have been posited as a barrier for glucose diffusion to sensor and as an initial substrate for cell adhesion downstream.	[8, 21-24]
Signal interference by small molecules	Ascorbate, urea and acetaminophen oxidize at similar voltages to hydrogen peroxide, causing interference with the sensor signal.	[25-27]
Effects of inflammatory cells	Inflammatory cell types are present around sensor surface. They release reactive oxygen species and proteolytic enzymes, and consume local glucose and oxygen at elevated rates, thereby altering sensing environment.	[16, 17, 21, 28]
Changes in microvascular patterns	After implantation, blood is shunted to more patent pathways, potentially limiting access to oxygen and glucose.	[21]
Long Term (>1 week post-implantation)		
Deposition of extracellular matrix	Fibroblasts recruited to the area of implantation deposit a dense, avascular layer of extracellular matrix around the sensor, potentially providing a diffusive barrier to transport.	[13, 18]
Limited vascular presence	The avascular barrier increases distances between the sensor and vessels, as well as decreasing angiogenesis.	[13, 17]

2.4 Medtronic MiniMed SofSensor Continuous Glucose Monitoring

All experiments described in this document will utilize Medtronic MiniMed SofSensor glucose sensors. There are three electrodes present within each sensor (Figure 2b). The counter electrode dissipates electrons from the sensing process back into the environment. The working electrode consists of multiple layers of different materials and is where the actual sensing of glucose occurs (Figure 2a). The active sensing layer contains the enzyme glucose oxidase immobilized with human serum albumin at a 1:1 ratio. The actual sensing mechanism is a two step process. First, glucose oxidase catalyzes the oxidation of interstitial glucose to gluconic acid and hydrogen peroxide (Eq. 1, Figure 2b). Secondly, a voltage is applied across the working electrode to decompose the hydrogen peroxide into electrons, hydrogen and oxygen (Eq. 2). The generated current is then correlated by the sensor to interstitial glucose concentration. The top most layer of the working electrode is an exclusion membrane of polyurethane that allows for glucose diffusion while inhibiting the diffusion of interfering molecules such as ascorbic acid, uric acid, acetaminophen, and cysteine. These molecules oxidize at voltages similar to hydrogen peroxide, and can obstruct sensor performance vis-à-vis false readings [25, 26].

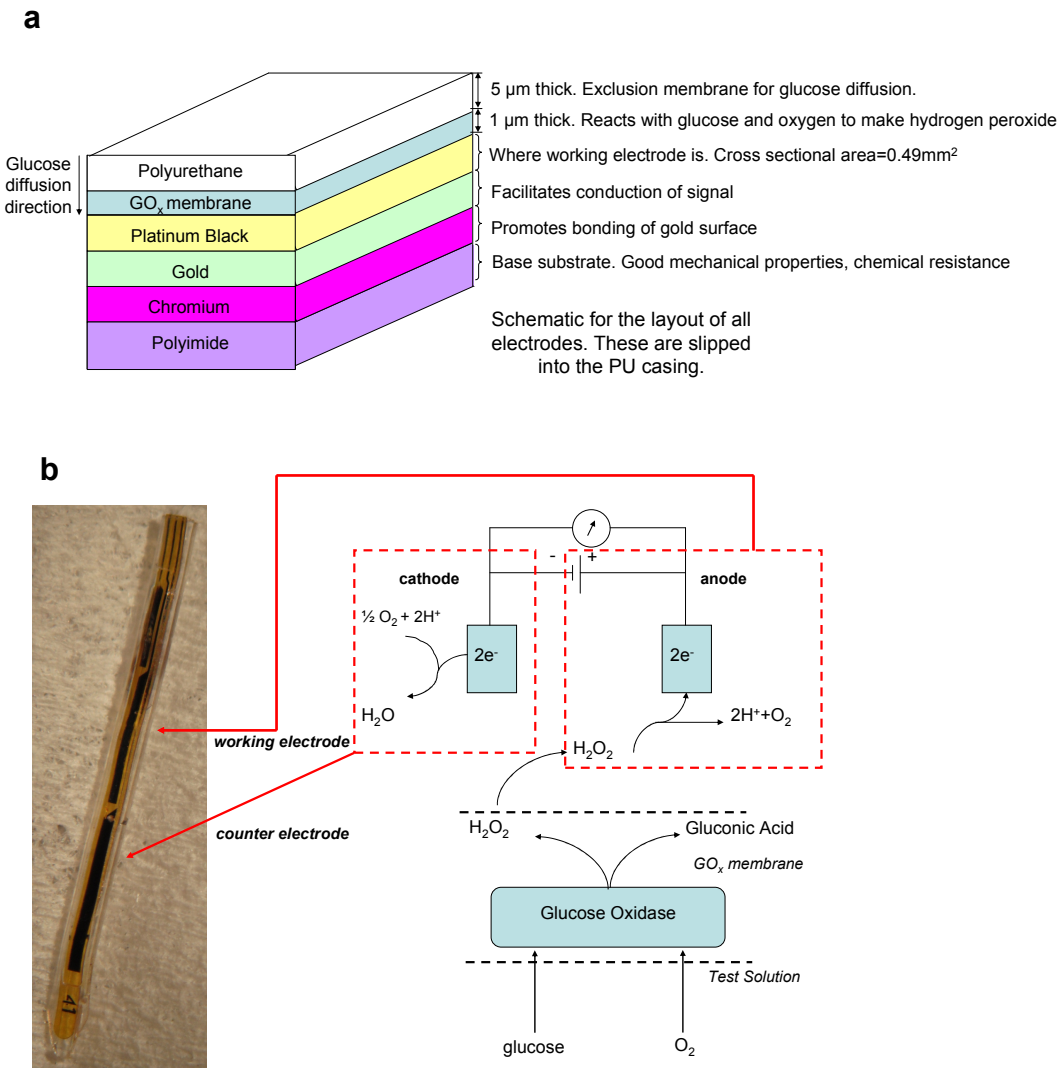

Figure 2: (a) Schematic of layers of working electrode of the sensor. (b) Visual description of sensor electrode.

$$\text{Glucose} + O_2 \xrightarrow{\text{Glucose Oxidase}} \text{Gluconic acid} + H_2O_2 \qquad (1)$$

$$H_2O_2 \xrightarrow{\text{Voltage}} 2e^- + O_2 + 2H^+ \qquad (2)$$

The reference electrode maintains a constant potential between itself and the working electrode. The SofSensor is connected to the Medtronic MiniLink, which

powers the sensor, collects sensor readings and wirelessly transmits data to a computer. The MiniLink processes the continuous signal from the sensor itself and averages it every one to five minutes to produce one electrical signal that correlates with interstitial glucose concentrations at that time.

2.5 Inflammatory Cell Consumption of Glucose and Oxygen

Though the effects of the implant-associated inflammatory cascade have long been seen as a diffusive barrier of small molecule transport to sensors, it is important to note that these stages also serve as bioactive barriers, as there are cells that consume small molecules. Indeed, it is now being posited that inflammatory cells must reprogram their metabolism to increase their uptake to perform functions such as phagocytosis during periods of immune response [29-31]. As glucose and oxygen are necessary inputs for glucose oxidase activity, it is important to understand how cellular affinity for each is affected by implantation. One of the most effective ways in which inflammatory cells like neutrophils and macrophages combat foreign objects is through what is known as an "oxidative attack" [32, 33]. During this process, inflammatory cells will generate reactive oxygen species (ROS) and reactive nitrogen species (RNS) [34]. Specifically, ROS are generated through a "respiratory burst" in which the uptake of glucose and oxygen is increased to promote the production of species like the superoxide anion through NADPH phagosome oxidase activity. In macrophages, the energy necessary to power NADPH phagosome oxidase activity is provided through the

increased metabolism of extracellular glucose [28, 35, 36]. As a result, there are increased numbers of glucose surface transporters that facilitate more pathways for transport into the cell for metabolism.

The effects of *in vivo* macrophage activation can be mimicked *in vitro* through the treatment of potent activators. Both LPS and PMA serve to supply macrophages with the extracellular signals necessary to activate them to pro-inflammatory phenotypes [37]. LPS simulates bacterial activation of macrophages, while PMA mimics intracellular signaling functions of diacylglycerol [38, 39]. While each has a unique pathway to activation, they have been shown to produce pro-inflammatory cytokines through the NF-κB pathway [40, 41]. As a result of activation, both LPS and PMA treatment serve to upregulate glucose uptake by inflammatory cells to help them meet the large metabolic requirements necessary for immune response. Both Fukuzumi, et al. and Gamelli, et al. showed increased levels of glucose uptake through the GLUT-1 transporter in LPS-stimulated murine peritoneal macrophages [42, 43]. Functionally speaking, Sherry, et al. demonstrated the increased need for extracellular glucose during activation by showing that TNF-α production in LPS-stimulated macrophages from diabetic mice was dependent on extracellular glucose concentrations [44]. Past studies have also shown that treatment of a RAW 264.7 murine monocyte/macrophage cell line with the pro-inflammatory differentiator PMA increases cellular affinity to extracellular glucose [36, 45]. With documented cases of increased cellular consumption of glucose, it is possible

that ancillary effects of implant-associated inflammation are inducing an environment that is not conducive for sensing.

Chapter 3. Numerical Characterization of the Influences of Late Stage, Fully Formed Capsular Tissue on Implanted Glucose Sensor Function

3.1 Synopsis

Little is known mechanistically about why implanted glucose sensors lag behind blood glucose levels in both the time to peak sensor response and the magnitude of peak sensor response. A mathematical model of glucose transport from capillaries through surrounding tissue to the sensor surface was constructed to address how different aspects of the tissue affect glucose transport to an implanted sensor. Physiologically relevant values of capsule diffusion coefficient, capsule porosity, cellular glucose consumption, capsule thickness and subcutaneous vessel density were used as inputs to create simulated sensor traces that mimic experimental instances of time lag and concentration attenuation relative to a given blood glucose profile. Using logarithmic sensitivity analysis, each parameter was analyzed to study the effect of these variables on both lag and attenuation. Results identify capsule thickness as the strongest determinant of sensor time lag, while subcutaneous vessel density and capsule porosity had the largest effects on attenuation of glucose that reaches the sensor surface. These findings provide concrete insight for the rational design of sensor modifications that may alleviate the deleterious consequences of long term tissue reactions on implanted sensor performance.

3.2 Introduction

In order to develop a sensor that can measure glucose concentrations with high sensitivity for a prolonged amount of time, the interaction between the sensor and the surrounding tissue must be considered. Once implanted, no sensor will exist as an inert object in the body since all implants will alter the surrounding environment. However, minimizing the effects of the sensor on the tissue will reduce errors associated with inflammation.

Figure 3a is a histological image from Yu et al. showing blood vessels embedded in a foreign body capsule that formed around an implanted glucose sensor two weeks post-implantation [18]. Hematoxylin and Eosin (H&E) staining shows the presence of red stained blood vessels, blue stained cells (mostly fibroblasts) and pink stained extracellular matrix. Relative to cells and extracellular matrix (ECM), blood vessels typically occupy only a small percentage of the total tissue area surrounding an implant [13]. Figure 3b is an image from Koschwanez et al. showing a Masson's trichrome stain of fibrous tissue that surrounded a glucose sensor three weeks post-implantation, with blue stained ECM, red stained cells, and no apparent evidence of vascularity [17]. Of particular note is the distinct layer of what are most likely inflammatory cells that lined the sensor surface. While no two encapsulation tissues exhibit the exact same histology, they do share some common characteristics: 1.) a porous network dominated by the

extracellular matrix network, 2.) little to no blood vessels, and 3.) the presence of metabolically active cells.

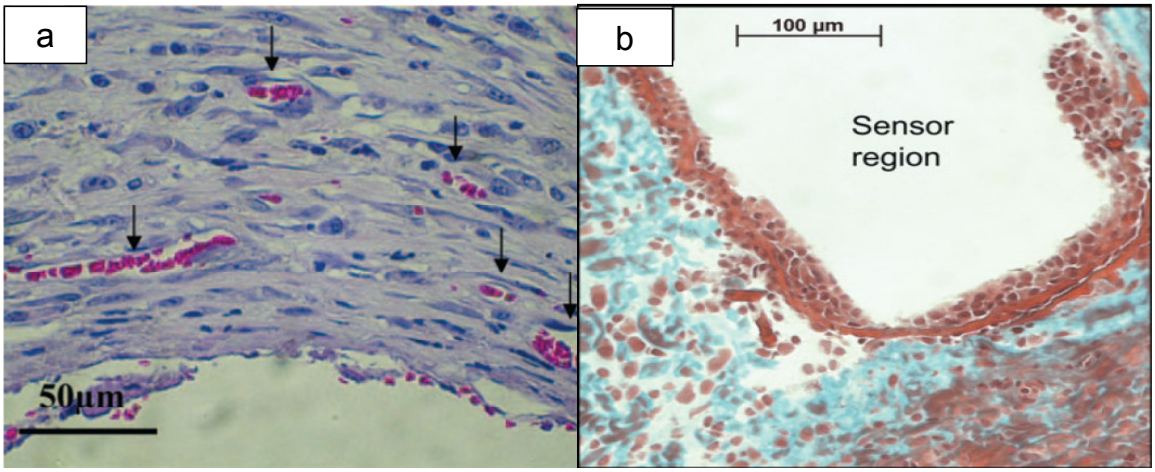

Figure 3: (a) Histological image of a foreign body capsule that has formed around an implanted glucose sensor at 14 days post-implantation. H&E staining demonstrates lack of vasculature (red) relative to cells (blue) within capsule. Image borrowed from [18]. (b) Masson's trichrome stain of a cross section of fibrous tissue 3 weeks post-implantation. Shows presence of extracellular matrix (blue) as well as cells (red) within capsule tissue. Provides basis for modeling capsule as dense, avascular network composed of inflammatory cells and extracellular matrix. Image borrowed from [17].

Glucose sensors implanted or inserted in subcutaneous tissue measure interstitial glucose, which causes the glucose concentrations measured by the sensor to inherently lag behind the peak blood glucose concentration both in terms of time and amount. However, these effects of lag and attenuation become exacerbated over the *in vivo* lifetime of an implant. Sensor lag time and attenuation have been thought to be attributable to the foreign body capsule through a number of physiological mechanisms, such as the presence of underdeveloped microvascular networks for limited glucose delivery, local glucose consumption by metabolically active inflammatory cells, and

decreased diffusion through the dense, collagen-rich capsule [13, 16-18]. There has also considerable speculation that the initial biofouling protein layer plays a significant role in limited sensor performance [8, 24].

Different sensor surface modifications and drug release schemes have been developed to resist biofouling, attenuate inflammation, increase vascular density, and/or minimize foreign body capsule thickness [17, 19, 20]. However, all of these treatments have been developed in the absence of mechanistic understanding of how different aspects of the foreign body reaction affect glucose transport to the sensor surface.

A computational model is presented that examines the effects of the characteristic aspects of fully formed encapsulation tissue on the transport of glucose from the microvessels to the surface of a subcutaneously implanted sensor after a bolus injection of glucose into the systemic circulation. While others have modeled glucose transport through capsular tissue, the tissue has always been treated as a passive diffusive barrier [46, 47]. In reality, the foreign body capsule is a perfused material comprised of a complex porous network that is both a diffusive barrier and a bioactive consumer of glucose that is subject to the influence of at least five variables: foreign body capsule thickness, foreign body capsule porosity, blood vessel density, density of glucose-consuming cells and the capsular diffusion coefficient of glucose. Greater understanding of these effects should lead to a more effective design of surface treatments intended to extend sensor performance.

3.3 Computational Methods

3.3.1 Two Compartment Model

Glucose transport through the tissue that encapsulates an implanted sensor was modeled as a two compartment, uni-dimensional diffusion-reaction problem (Figure 4). The first outer compartment modeled native subcutaneous tissue as a porous environment rich in blood vessels and resident mesenchymal cells (e.g. adipocytes and fibroblasts). The second inner compartment modeled fibrous tissue, representing an avascular, porous environment with a presence of inflammatory cells. The layer of adsorbed protein at the sensor surface was neglected in this analysis.

The governing equation for glucose concentration in the outer native subcutaneous tissue (C_{tis}) is a non-linear, uni-dimensional diffusion-reaction equation in cylindrical coordinates through a porous medium (Eq. 3).

$$\frac{\partial C_{tis}(r,t)}{\partial t} = \frac{D_{tis}}{r}\frac{\partial}{\partial r}\left(r\frac{\partial C_{tis}(r,t)}{\partial r}\right) + \Phi_b - Q_{tis}(r,t) \tag{3}$$

Φ_b and Q_{tis} represent the rate of glucose transport from the lumen of microvessels to the interstitial space of the subcutaneous tissue and the consumption rate of glucose by native adipocytes in the subcutaneous space. Φ_b is defined as the rate of glucose transport per unit volume from blood vessels into the interstitial space of the tissue, making it the source of glucose for the tissue compartment. It is described by a modified version of the Kedem-Katchalsky equation, where P is the microvascular

permeability of the vessel wall to glucose (cm/sec), $\frac{S}{V}$ is the density of blood vessels in terms of the microvessel surface area per unit volume of the tissue (cm^2/cm^3), C_p is the concentration of glucose in the blood (μmol/ cm^3), and ε_{tis} is the porosity of the native tissue (unitless) (Eq. 4) [48].

$$\Phi_b = \frac{PS}{V}\left(C_p(t) - \frac{C_{tis}(r,t)}{\varepsilon_{tis}}\right) \tag{4}$$

Q_{tis} is defined as the uptake of glucose by native adipocytes and is represented by Michaelis-Menten kinetics, where $V_{\max,tis}$ is the maximum rate of glucose consumption (μmol/(cell-sec)), $K_{M,tis}$ is the Michaelis constant (μmol/L), ε_{tis} is the porosity of the native tissue (unitless), and z_{cell} is the volume of a native cell (L/cell) (Eq. 5) [28]. This term represents a glucose sink, as uptake of the analyte by cells removes it from the system.

$$Q_{tis}(r,t) = \frac{V_{\max,tis}C_{tis}(r,t)}{K_{M,tis}\varepsilon_{tis} + C_{tis}(r,t)}\left(\frac{1-\varepsilon_{tis}}{z_{cell}}\right) \tag{5}$$

The inner fibrous capsule compartment was modeled as an avascular area, which is consistent with histological findings that show a decreased presence of blood vessels relative to native tissue [47]. As a result, the governing equation describing glucose concentration in the fibrous capsule (C_{FBC}) (Eq. 6) has no source term in addition to the

diffusion terms, and only a sink term to describe uptake by inflammatory macrophages that is similar to the uptake expression in the native tissue compartment.

$$\frac{\partial C_{FBC}(r,t)}{\partial t} = \frac{D_{FBC}}{r}\frac{\partial}{\partial r}\left(r\frac{\partial C_{FBC}(r,t)}{\partial r}\right) - Q_{FBC}(r,t) \tag{6}$$

Q_{FBC} is defined as the rate of glucose uptake by inflammatory macrophages in the capsule and is modeled by Michaelis-Menten kinetics, where $V_{\max,FBC}$ is the maximum rate of consumption (μmol/(cell-sec)), $K_{M,FBC}$ is the Michaelis constant (μmol/ L), ε_{FBC} is the porosity of the native tissue (unitless), and z_{cell} is the volume of an inflammatory cell (L/cell) (Eq. 7) [49]. This term represents a glucose sink in the capsule, as uptake of the analyte by cells removes it from the system.

$$Q_{FBC}(r,t) = \frac{V_{\max,FBC}C_{FBC}(r,t)}{K_{M,FBC}\varepsilon_{FBC} + C_{FBC}(r,t)}\left(\frac{1-\varepsilon_{FBC}}{z_{cell}}\right) \tag{7}$$

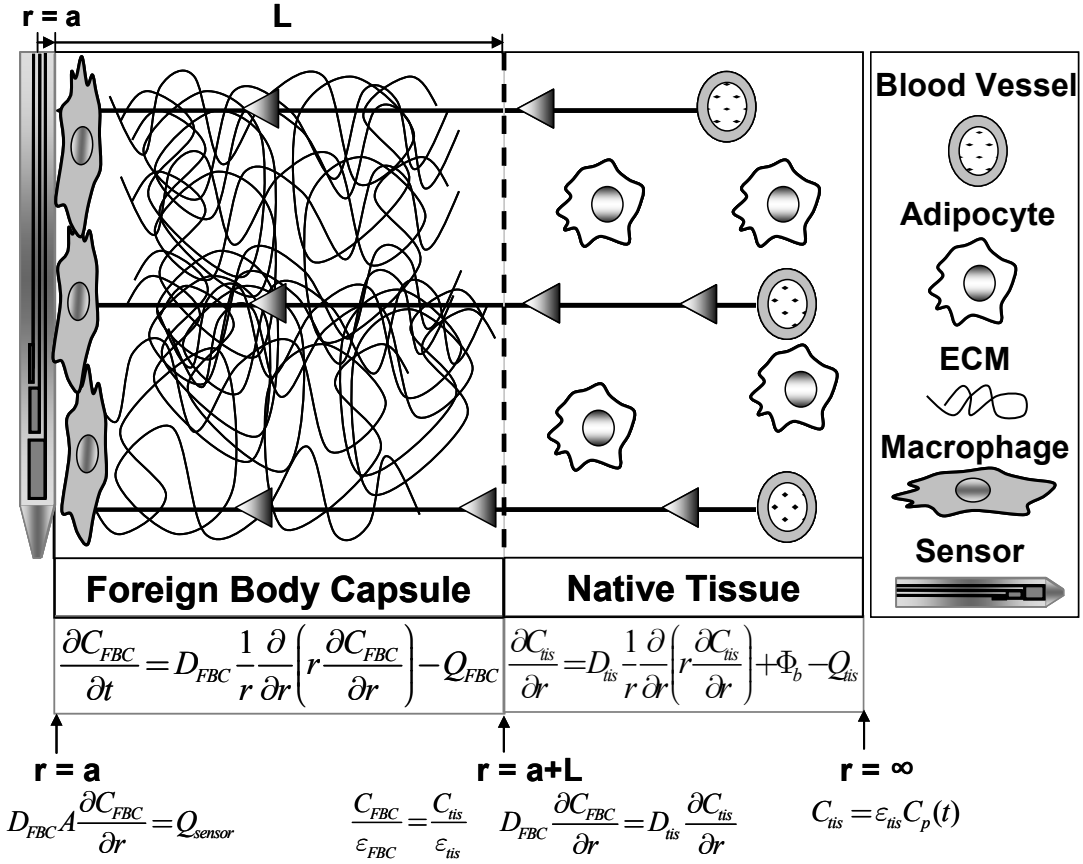

Figure 4: Schematic representation of model for diffusion of glucose through native tissue and the fibrous capsule.

3.3.2 Initial and Boundary Conditions

For the initial condition, it was assumed that the diffusion time in the tissue was much shorter than the time scale of simulation. The initial condition for the system was a vector that was output when running the simulation for a baseline input concentration before the fitted blood glucose bolus was input.

Boundary conditions were specified at the sensor surface (r=a), the interface between the tissue and capsule compartments (r=a+L), and a location far away from the

sensor (r→∞). At the sensor surface, the rate of glucose diffusion in the capsule compartment is equal to the rate of glucose uptake by the sensor, Q_{sensor} (Eq. 8). It was assumed that the consumption rate was proportional to the glucose concentration at the sensor surface with λ being the proportionality constant (mol/(mM-sec)). The sensitivity of the sensor to glucose may decay with time. To account for this occurrence, a nondimensional parameter, α, was introduced. It is defined as the sensor efficiency and ranges from zero to unity. For this case, the sensor is assumed to be perfectly efficient, with α=1. A_{sensor} is defined as the total surface area of the sensor available for glucose transport and a is the radius of the sensor [50].

$$D_{FBC} A_{sensor} \frac{\partial C_{FBC}}{\partial r}(r=a,t) = Q_{sensor} = \frac{\alpha \lambda C_{FBC}(r=a,t)}{\varepsilon_{FBC}} \tag{8}$$

At the interface between the tissue and capsule compartments, it is assumed that glucose is conserved and no glucose accumulates or disappears at the interface, so both concentrations and fluxes are matched (Eqs. 9 and 10).

$$\frac{C_{FBC}(r=a+L,t)}{\varepsilon_{FBC}} = \frac{C_{tis}(r=a+L,t)}{\varepsilon_{tis}} \tag{9}$$

$$D_{FBC} \frac{\partial C_{FBC}}{\partial r}\left(r=a+L,t\right) = D_{tis} \frac{\partial C_{tis}}{\partial r}\left(r=a+L,t\right) \tag{10}$$

In tissues far away from the sensor, it is assumed that the concentration in the tissue is the same as that in the blood (Eq. 11).

$$C(t, r \to \infty) = \varepsilon_{tis} C_p(t) \tag{11}$$

3.3.3 Blood Glucose Concentration

Blood glucose profiles used in simulations were numerical fits of actual experimental intravascular glucose infusion data taken from the published literature. The glucose infusion and sensor response data of Koschwanez et al. were employed to demonstrate that the program generated realistic dose-response behavior of a subcutaneously implanted sensor [17]. For parametric sensitivity analysis the glucose infusion data of Armour, et al. were employed because the blood glucose data are from an intravascular sensor that may measure instantaneous changes in blood glucose more reliably than data from a discrete finger prick test [51]. The raw infusion data from Armour et al. were fit to a sum of three Gaussian curves (Eq. 12). The fitted values for the constants in Eq. 12 are given in Table 2.

$$C_p(t) = a_1 e^{-\left(\frac{t-b_1}{c_1}\right)^2} + a_2 e^{-\left(\frac{t-b_2}{c_2}\right)^2} + a_3 e^{-\left(\frac{t-b_3}{c_3}\right)^2} \tag{12}$$

Table 2: Fitted parameters from raw data of Armour, et al. for blood glucose expression in Eq. 12 [51].

a (μM)			b (sec)			c (sec)		
a_1	a_2	a_3	b_1	b_2	b_3	c_1	c_2	c_3
2404.64	5678.23	6.2449×10^8	2482.8	3954	3.013×10^6	733.8	1303.8	8.562×10^5

3.3.4 Transport and Kinetic Parameters

In order to accurately mimic a fully formed capsule, the physiologically relevant values of model constants listed in Table 3 were used in numerical simulations.

However, it should be noted that chronic inflammation and wound healing processes may lead to changes in these values; a condition that was not considered in this study.

Diffusion coefficient values (D) were obtained from the study of glucose transport in subcutaneous tissue and the fibrous capsule, respectively. The $V_{\max}$ and K_M values in the capsule were based upon the data of macrophage uptake of glucose while those in the native tissue were based upon adipocyte uptake of glucose, thereby accounting for the fatty nature of the human subcutis. Capsule thicknesses (L) vary based upon the type of implant, how it is implanted, and what is classified as a foreign body capsule. Results for subcutaneously implanted sensors can vary anywhere from 30 to 750 μm, in extreme cases [12, 18, 47]. The thickness was chosen to be 75 μm since it was a typical value for a well formed capsule. The surface area of the sensor was measured for a Medtronic MiniMed sensor.

Table 3: List of all baseline model parameters. Values listed with * in the citation column are model assumptions while those listed with ** are calculated values with no previous citation.

Model Parameters	Parameter Values		
	FBC	Native Tissue	Citation
Diffusion Coefficient (D) (cm^2/sec)	$1.87x10^{-6}$	$3.5x10^{-6}$	[47]
Porosity (ε) (unitless)	0.5	0.6	*
Vessel Density (S/V) (cm^2/cm^3)	-	15.4	[50]
Capsule Thickness (L) (μm)	75	-	[12, 18, 47]
Michaelis Constant (K_M) (μM)	$6.13x10^3$	$6.2x10^3$	[28, 49]
Maximal rate of cellular glucose uptake (V_{max}) (μmol/(cell-sec))	$4.88x10^{-11}$	$3x10^{-11}$	[28, 49]
Vascular glucose permeability (P) (cm/sec)	-	$5x10^{-5}$	[48]
Conversion constant (λ) (mol/(mM-sec))	$2.574x10^{-14}$	-	**
Cell Volume (z_{cell}) (L/cell)	$9.5x10^{-13}$	$9.5x10^{-13}$	*
Glucose Sensor Radius (a) (cm)	0.07	-	[50]
Sensor Surface Area (A) (cm^2)	0.0058	-	[50]

3.3.5 Parametric Sensitivity Analysis

Aspects of the fibrous capsule that had the greatest effect on either time lag or sensor signal attenuation were determined by running the simulation for a range of values for each parameter, while keeping all other parameters constant. The parameters to be considered were capsule diffusion coefficient (D_{FBC}), capsule porosity (ε_{FBC}), vessel surface area per unit volume of subcutaneous tissue ($\frac{S}{V}$), maximum rate of glucose uptake by macrophages ($V_{\max,FBC}$) and capsule thickness (L). Table 4 shows the range of values that were input for the sensitivity study. For every simulation that was executed for a value of a given parameter, the model computed both an associated output lag time and an attenuation value. Therefore, for an input range of N values of a given parameter, there would be N associated lag times and N associated attenuation values.

The sensitivities of these output values to their input values of the model parameters were calculated using logarithmic sensitivity analysis [52]. The representative equation for a logarithmic sensitivity, S_i, of an output value, l, for a given input parameter, x, is given in Eq. 13.

$$S_i = \frac{\Delta l}{\Delta x}\frac{x_i}{l_i} \tag{13}$$

Δl is defined as the difference between outputs over the range of input values and Δx is defined as the difference between the input values. x_i is defined as the

midpoint of the input range, and l_i is the output associated with the input, x_i. For a range of input and output values, one could calculate a range of sensitivities by decreasing Δx. By calculating sensitivity in this way, the differences in absolute magnitude are not considered. Instead, only the relative change in response to the relative change in the input is considered.

For this specific series of simulations, ranges of values for the capsule diffusion coefficient (D_{FBC}), capsule porosity (ε_{FBC}), subcutaneous vessel density ($\frac{S}{V}$), cellular uptake of glucose ($V_{\max,FBC}$), and capsule thickness were entered into the model. When testing one parameter, all others were held constant to see how the changes within each parameter affect simulated sensor performance.

Table 4: Range of different parameters to be used for sensititivity analysis. Bolded values represent benchmark values from Table 3.

	Parameters				
	D_{FBC} (cm^2/sec)	ε_{FBC} (unitless)	$V_{max,FBC}$ (μmol/(cell-sec))	Vessel Density (cm^2/cm^3)	Capsule Thickness (μm)
1	$1.87x10^{-7}$	0.2	$4.88x10^{-12}$	2	15
2	$3.74x10^{-7}$	0.4	$2.44x10^{-11}$	5	**75**
3	$9.35x10^{-7}$	**0.6**	**$4.88x10^{-11}$**	**15.4**	150
4	**$1.87x10^{-6}$**	0.8	$9.76x10^{-11}$	60	375
5	$3.74x10^{-6}$	0.9	$2.44x10^{-10}$	120	750
6	-	-	$4.88x10^{-10}$	166.3	-

3.3.6 Assessing Glucose Sensor Performance

Lag times were calculated as the difference between the time at which glucose concentration peaked in the blood glucose profile and the time glucose concentration peaked at the sensor surface. Attenuation of glucose concentration due to capsule formation was calculated as one minus the ratio of the peak sensor surface value divided by the peak blood glucose value (Eq. 14).

$$Attenuation = 1 - \frac{\max\left\{C_{FBC}(t, r = a)\right\}}{\max\left\{C_P(t)\right\}} \tag{14}$$

3.3.7 Numerical Methods

The governing partial differential equations were discretized into a series of ordinary differential equations using the finite difference method. These discretized equations were then solved using the differential equation solver, ode15s, in MATLAB (The Mathworks, Natick, MA). Curve fitting for the blood glucose profile was performed using the Curve Fitting Toolbox in MATLAB.

3.4 Results

3.4.1 Numerical Approximation of *In Vivo* Experimental Sensor Data

The individual data points in Figure 5 are rat tail prick blood glucose values following a tail vein injection of 0.5 mL of 50% dextrose measured using a commercial blood glucose meter (●), and the corresponding values from a MiniMed sensor implanted for 24 hours in the dorsal subcutis of the same rat as reported by Koschwanez, et al. (■) [17]. The dashed line superimposed on the experimental blood glucose values (-·-) is the best fit of Eq. 12 to the blood glucose values, which was then used as a model input to generate the simulated glucose sensor response (--). This trace can then be compared to the solid line fitted to the experimental sensor data. Figure 5 also indicates the sensor time lag (Δt_{est}) and the sensor attenuation (ΔC_{est}) for the simulated data that was used in subsequent sensitivity analyses. The experimental lag (Δt_{exp}) and attenuation (ΔC_{exp}) from Koschwanez, et al. are also reported in Figure 5 [17].

Overall, Figure 5 shows that the program was able to approximate the temporal profile of the experimental data from the implanted sensor. The simulated sensor response has a lag time of ~3 minutes and the sensor signal was 76% of the blood glucose signal for a signal attenuation of 24% [17]. With regards to attenuation, the simulated trace only minimally overestimates attenuation, producing a peak that is 97% of the measured sensor peak. Lag times are less similar between the experimental and simulated data, with the simulated trace recording a lag of 2.87 minutes, underestimating the experimental lag of 5.28 minutes. It should be noted that attenuation and lag are less pronounced in this simulation because model parameters were based upon the local environment at 24 hours post-implantation, which is before a mature capsule has formed. While subsequent studies in this chapter will describe transport through a fully formed capsule, this example demonstrates the ability of the model to describe different temporal regimes of the post implantation environment when compared to experimental data.

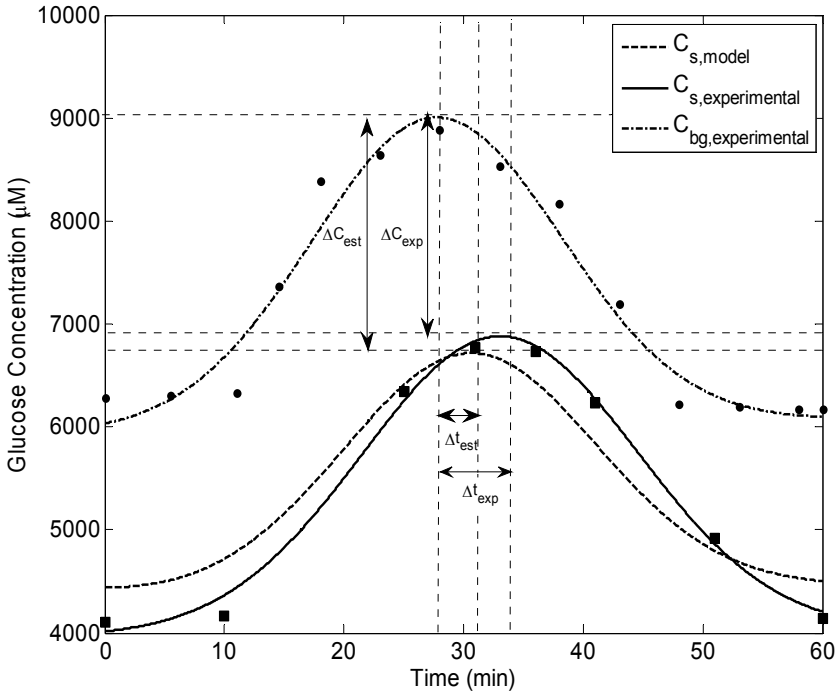

Figure 5: Simulated recreation of experimental glucose sensor traces. Raw blood glucose data (●) was fit to a continuous curve, $C_{bg,\exp erimental}$, (-●-) and then input into the model to give a simulated glucose sensor trace, $C_{s,\mathrm{mod}el}$, (--). This output was compared in shape to raw sensor data (■), which is fit by a solid line, $C_{s,\exp erimental}$. The simulated trace produced a lag time (Δt_{est}) and attenuation (ΔC_{est}) and a shape similar to data in Koschwanez, et al [17]. The lag time and attenuation from [17] are represented in Figure 5 by Δt_{exp} and ΔC_{exp}.

3.4.2 Sensor Lag Time and Attenuation of Glucose Concentration

Values of time lag and glucose attenuation were calculated using the physiologically representative literature values in Table 3 where five of these variables – capsule diffusion coefficient, capsule porosity, maximum cellular uptake rate for glucose in the capsule, vascular density in surrounding native tissue, or the capsule thickness – were allowed to vary independently as listed in Table 4. These calculations resulted in

the set of five plots presented in Figure 6. In each case, the results were normalized to the benchmark values of time lag and attenuation calculated using the Table 3 values. This normalization allowed direct comparison of the fractional effects of independently varying one of the five parameters listed in Table 4.

Figure 6 shows the relative effects of varying (a) the capsule diffusion coefficient, (b) the capsule porosity, (c) the vascular density in surrounding native tissue, (d) the cellular uptake of glucose in the capsule, and (e) the capsule thickness on sensor time lag and attenuation.

Increased capsule diffusion coefficient, capsule porosity, and vessel density all lessened attenuation of peak glucose concentration at the sensor surface. Conversely, increased cellular uptake of glucose in the capsule and capsule thickness both increased attenuation of peak glucose concentration at the sensor surface. In this case, changes in the diffusion coefficient and cellular uptake both had only modest effects. Lag times were found to increase with increases in porosity and capsule thickness as well as decreases in vessel density and diffusion coefficient. Changes in cellular uptake produced negligible changes in lag.

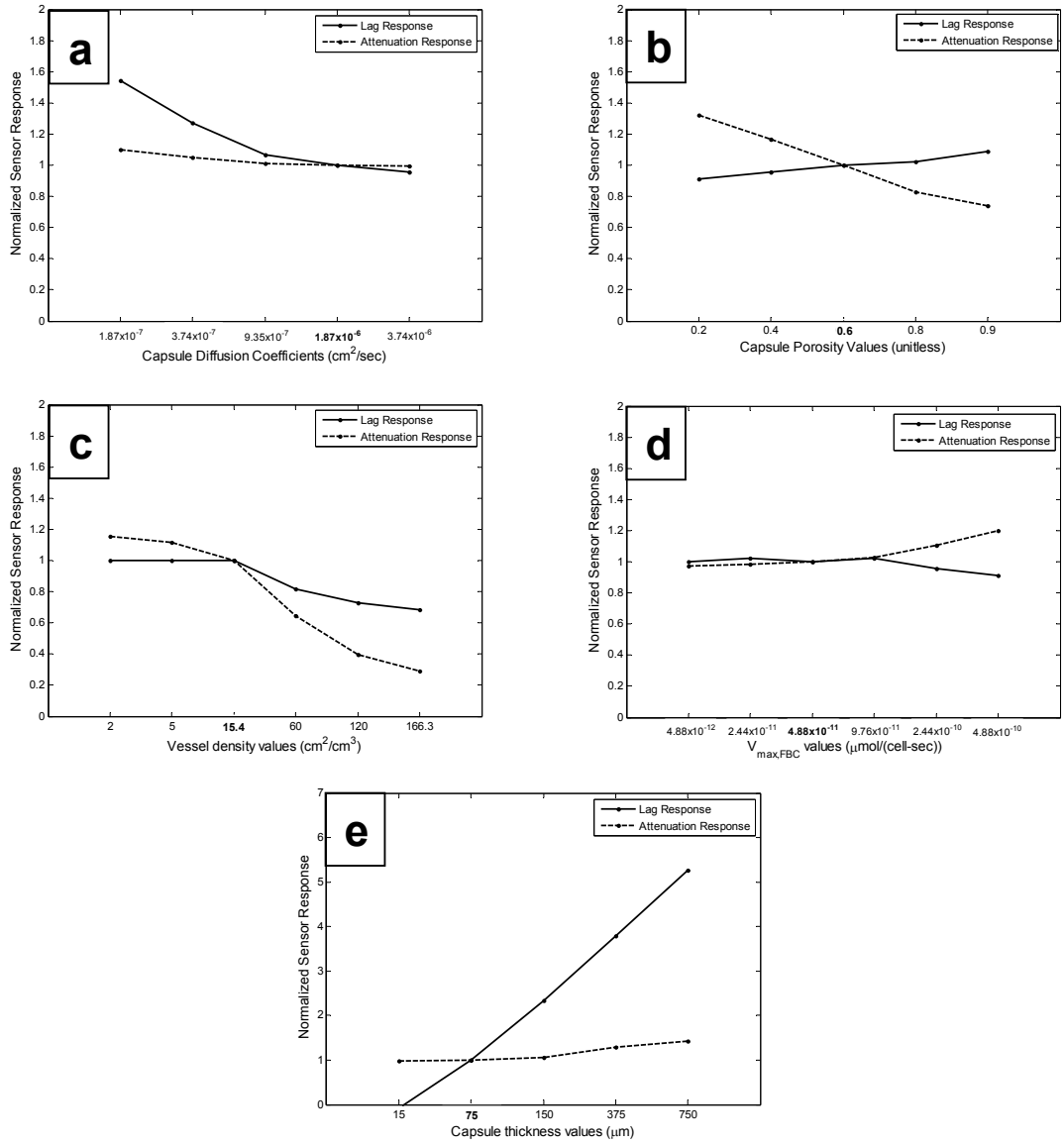

Figure 6: Effect of (a) capsule diffusion coefficient, (b) capsule porosity, (c) vascular density in surrounding native tissue, (d) cellular uptake of glucose in the capsule, and (e) the capsule thickness on sensor lag times (-●-) and attenuation (--●--) Results have been normalized to baseline values in Table 3.

3.4.3 Lag Time and Attenuation Sensitivity Analysis

Logarithmic sensitivity analysis was used to determine the sensitivity of a dependent variable, such as lag or attenuation, to variation in one independent variable while holding all other independent variables constant. Figure 7 shows box and whisker plots of logarithmic sensitivities for (a) normalized lag times and (b) normalized glucose attenuation values as functions of the five independent variables listed in Table 4.

Sensor lag time was shown to be highly sensitive to changes in capsule thickness, while only mildly sensitive to the other four variables. The minimum sensitivity due to capsule thickness change (0.4828) was more than twice that of the maximum sensitivity from the next highest value due capsule porosity change (0.2307).

The attenuation of blood glucose as it is transported to the sensor surface was most sensitive to two variables: the vessel density of the subcutaneous tissue and the capsule porosity. Glucose attenuation also appears to be mildly sensitive to capsule thickness, and essentially insensitive to capsule diffusion coefficient and cellular glucose uptake. Although vessel density did have the highest maximal sensitivity value of 1.01, it had a lower mean sensitivity than capsule porosity, and a minimum sensitivity value of 0.0515 that was similar in magnitude to the less sensitive parameters of capsule thickness, capsule diffusion coefficient and cellular glucose uptake.

Interestingly, increasing capsule thickness had a pronounced effect on increasing sensor lag time, but capsule thickness had only a modest effect on glucose attenuation;

whereas increasing either vessel density or capsule porosity had pronounced effects on decreasing glucose attenuation, but neither vessel density nor capsule porosity had appreciable effects on sensor lag time. Furthermore, both sensor lag time and glucose attenuation were essentially insensitive to cellular uptake of glucose.

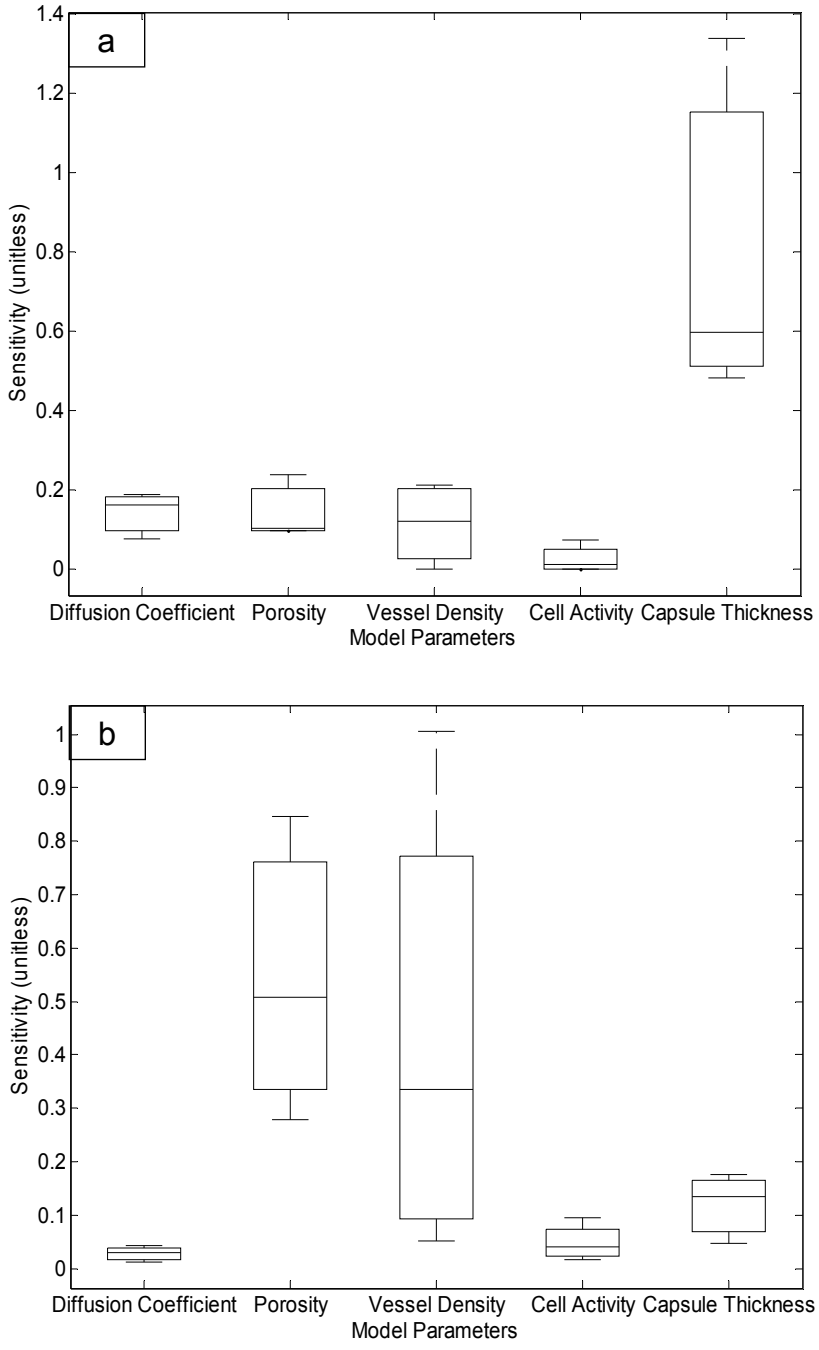

Figure 7: (a) Box and whisker plots of lag sensitivity to five different model parameters. (b) Box and whisker plots of attenuation sensitivity to five different model parameters. Sensitivities are represented as unitless values to allow for comparison across parameters.

3.5 Discussion

Experimental studies have shown that if an implanted glucose sensor can withstand the 7-14 days that it normally takes to form a stable fibrous capsule, then it is more likely to remain functional in the body for months [53]. The current study used a transport model to simulate the behavior of an implanted glucose sensor surrounded by a fibrous foreign body capsule. The primary advantage of the modeling approach over experimentation was the ability to evaluate the effects of individual physiological parameters on glucose sensor response.

The goal of this study was twofold: 1) demonstrate that the transport model accurately reproduces implanted glucose sensor response by incorporating physiologically relevant tissue parameters, and 2) use the model to gain insight into aspects of the fibrous capsule and the surrounding tissue that most affect sensor lag time and glucose signal attenuation.

The suitability of the transport model was demonstrated by generating a simulated implanted glucose sensor response using a blood glucose profile from Koschwanez et al. as the input (Figure 5) [17]. The simulated sensor output was compared to the actual implanted sensor response to the input blood glucose profile. The model was able to reproduce the shape of the implanted sensor trace with an attenuation and lag time that are comparable to experimental data.

Table 3 lists the physiological modeling parameters used to describe a mature fibrous capsule that would surround a sensor a few weeks following subcutaneous implantation. These values were used to generate a benchmark simulated sensor response for the sensitivity studies. Vessel densities were based on measured values at 3 weeks post implantation in the subcutaneous tissue of rats. Cell metabolic values were based on those of macrophages, which are the dominant cell type in the fibrous capsule at that time. Capsule thicknesses were similarly based upon reported values at 3 weeks post implantation, though thickness values vary considerably across the literature due to what is considered a capsule during experiments.

It should be noted that the biofouling layer was neglected in the simulations. Generally this stratum of protein and protein fragments ranges from 20 nm to 0.5 μm in thickness, which creates a negligible effect on transport, even when its permeability to glucose is drastically decreased (data shown in Chapter 4). These findings further support findings from Wisniewski et al. who found that the surrounding fully developed capsular tissue offered substantially greater resistance to glucose transport than the biofouling layer [8]. While many believe that the proteins and proteolyic enzymes within the biofouling layer can damage the glucose-sensitive membranes on sensor electrodes, those assertions are outside the scope of this study, which only considers biofouling from a transport perspective.

The transport model was utilized to examine how capsule formation affects the onset of lag times and signal attenuation. When exposed to a range of values for the five parameters of interest, lag times were most affected by changes to the thickness of the capsule. Lag times steadily increased in a linear fashion over a range of thicknesses. Such an effect upon lag time should be expected. First, a thicker capsule translates to larger length scale that allows for more random routes for transport of glucose molecules to the sensor surface [54]. Second, since the capsule was assumed to be avascular, the distance between source blood vessels and the target sensor has been increased. Therefore, capsule thickness cannot affect how much glucose is in the system but instead can only affect how fast the glucose reaches the sensor. By comparison, changes in lag time were not affected appreciably by changes in capsule porosity, capsule diffusion coefficient, or cellular uptake of glucose. From a biological perspective, this implies that the physical thickness of the capsule mattered more to inducing the lag time than did changes in the constituent parts of the capsule.

With respect to attenuation, capsule porosity and vessel density were found to have the largest effects on sensor response, though these ranges of sensitivities exhibited greater spread than those values in the lag time study. Attenuation sensitivity to vessel density ranged from an essentially insensitive factor of 0.0515 for low vessel densities to the most highly impactful factor for all parameters of 1.01. This finding is intuitive as blood vessels in the subcutaneous tissue are the only source of glucose in the model;

therefore a reduction in the source of glucose translates into a decreased amount of glucose that can even reach the sensor. The vessel density findings corroborate those of Sharkawy and Koschwanez, who have found that the presence of vessels can extend the useful life of the sensor [17, 55].

Comparatively, the influence of capsule porosity on attenuation had a higher median sensitivity and narrower range of sensitivities, suggesting that it had a more consistent effect on attenuation than did vessel density. Low capsule porosity increased glucose attenuation because it reduced transport pathways, resulting in a diminished amount of glucose molecules reaching the sensor surface and an accumulation of glucose in the native tissue.

It is interesting to note that high vessel density and high porosity have similar effects on glucose attenuation: porosity exhibits high attenuation sensitivity at high porosities ($\varepsilon_{FBC} > 0.6$) and vessel density exhibits high attenuation sensitivity at high vessel densities ($S/V > 60 cm^{-1}$), both of which are likely to occur early following implantation. As capsule formation occurs, the capsule goes from a loosely organized protein and cell layer to a highly dense layer of cells and extracellular matrix. Therefore, the high sensitivity at high porosities denotes that capsule porosity has a large effect on attenuation at points early in the capsule formation process. Similarly, peak attenuation sensitivity occurs at vessel densities near pre-implantation values, which would indicate that it affects attenuation early in the capsule formation process as well. This finding

suggests an initial synergistic effect of both the changing porosity and changing vessel density on attenuating sensor response early in the capsule process. However, as vessel density decreases through capsule formation, so does its sensitivity to attenuation, reaching a minimum at 0.0515. Though sensitivity due to capsule porosity also decreases as the capsule forming process continues and porosity decreases, its minimum is still much higher (0.278) than the maximum values of other parameters. For later times in capsule formation, porosity continues to dominate attenuation sensitivity. So, attenuation sensitivity is initially affected by both vessel density and capsule porosity, with porosity dictating attenuation as the capsule continues to grow.

Ultimately, we are interested in the conditions that generate the best scenario for glucose transport to an implanted sensor. Figure 8 is a scatter plot that summarizes all of the lag time and glucose attenuation values generated for all of the conditions tested using the computational model. Vessel Density (green), capsule porosity (blue) and capsule thickness (red) were labeled to see the lag time and attenuation trends among the highly sensitive model parameters. The benchmark point determined using the baseline values in Table 3 is labeled in magenta and represents the intersection of all other points in the simulation.

The quadrant on the bottom left of Figure 8 represents low attenuation (<0.5) and low lag (<5 min). Of all the conditions entered into the model, only vessel density between 60 and 166.3 cm^2/cm^3 produced a low attenuation and low lag environment.

Attenuation dropped four fold from nearly avascular conditions to a highly vascular tissue typical of subcutaneous tissue. This finding demonstrates the importance that adequate vessel density has on effective implantable sensor readings *in vivo* and corroborates previous assertions by Ward et al. about the importance of vasculature in sensor performance [56]. The upper right quadrant represents the worst case scenario of high lag time and high attenuation. Only high capsule thicknesses generated this situation with lag times increasing steadily from nearly 0 sec to nearly 10 minutes with a 50-fold increase in capsule thicknesses, further showing the deleterious effects of a thick capsule on sensor performance. Most results resided in the upper left quadrant of low lag and high attenuation, suggesting that most of the conditions tested affected attenuation more than lag time. Thus, lag was attributed almost exclusively to capsule thickness, while attenuation was affected by multiple factors. No points resided in the lower right quadrant, suggesting that changes in the model parameters will not create a situation where a sensor will have a high lag time and low attenuation.

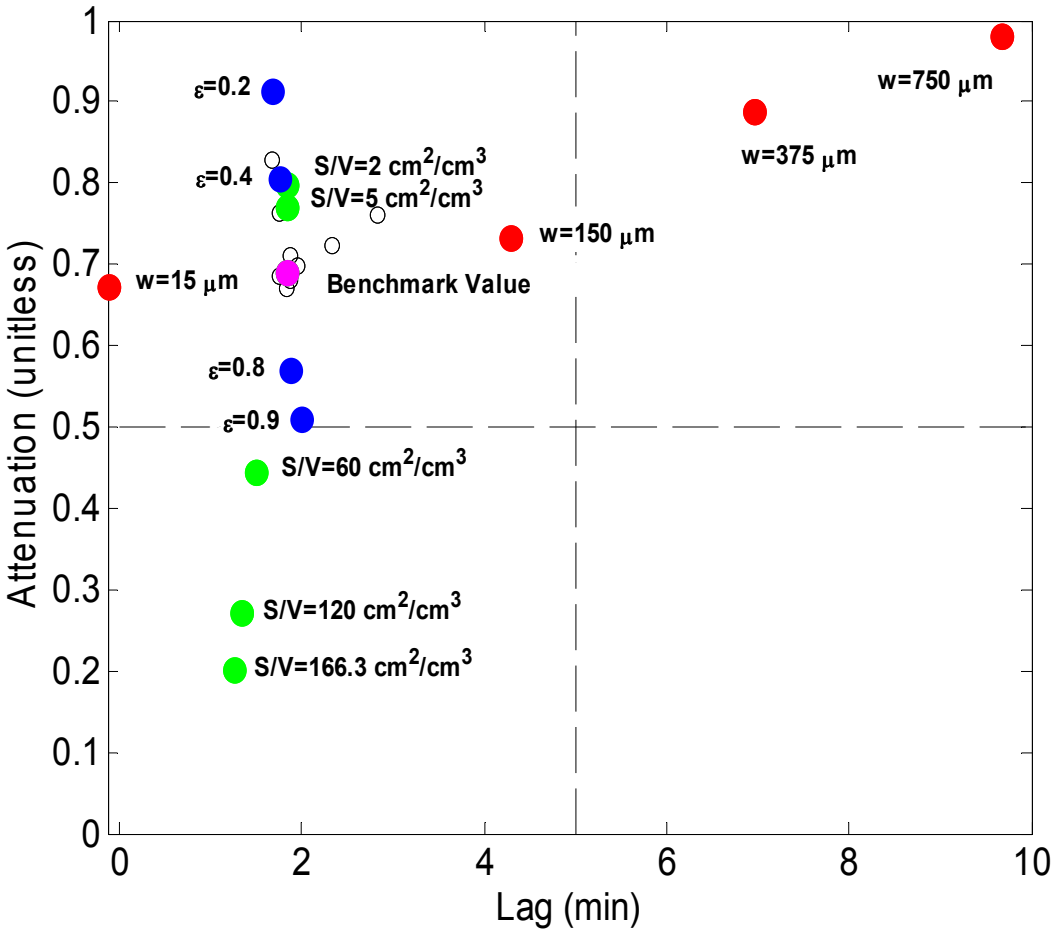

Figure 8: Scatter plot of sensor time lag v. glucose attenuation for all of the conditions simulated with the transport model. The three variables that showed the greatest sensitivity – capsule thickness, vessel density and capsule porosity – are represented by the red, green and blue circles, respectively. The benchmark value of time lag and attenuation calculated using the variables in Table 3 is labeled in magenta. This data point is common to all simulation trials. The open circles clustered around the benchmark value are the results obtained for the less sensitive variables of capsule diffusion coefficient and cellular glucose uptake.

Finally, this modeling study made two key assumptions: 1) that each parametric variable could be changed independently without affecting the others, and 2) that the system can be described as a straightforward two compartment transport model.

Clearly, the assumption of variable independence is problematic because a number of transport parameters are in fact interrelated. For example, the diffusion coefficient for the capsule is not just the diffusion coefficient of glucose in the void space of the capsule, but the effective diffusion coefficient of glucose in the capsule matrix that would be affected by altering the porosity or the cellular glucose uptake. However, this study is just asking what happens when one parameter is changed. This study is more concerned with what happens to the output when a parameter changes, not necessarily how it changes constituent parts.

The possible omission of additional mitigating variables from the model is also of concern. This finding may be most apparent in that most conditions yielded a lag time of approximately 2 minutes, except for cases of very thin or very thick capsules. Such a finding is in contrast to the 5 minutes or longer time lags typically reported in the literature for implanted glucose sensors, even in cases where the sensor has been implanted for short time periods before any fibrous capsule could form. This may suggest that factors like metabolic activity of inflammatory cells should be taken into greater account in future iterations. An additional factor that may help to account for time lag is the change in microcirculation patterns in tissues during inflammation and wound healing. Besides the obvious changes in vessel density, there is also a decrease in the length and diameter of vasculature in wound healing tissue as well as a decrease in red blood cell velocity [57]. Smaller diameters of the existing vessels in the tissue will

create a higher resistance to blood flow and may shunt blood flow to a different collection of vessels. Therefore, not only the number of patent blood vessels, but also the geometry of those vessels will affect the delivery of glucose to the subcutaneous space. Future computational studies will have to account for such changes to create a more complete portrait of the post-implantation environment.

3.6 Conclusions

This study describes a computational model of glucose transport through native tissue and across a mature foreign body capsule to a sensor surface that was used to examine how different transport parameters affect long term sensor time lag and attenuation of glucose to reach the sensor surface. Sensitivity analysis shows that when considering a fully formed capsule, sensor lag is mainly attributable to changes in capsule thickness and sensor attenuation is primarily affected by changes in vessel density and capsule porosity. Another interesting point was the observation that the capsule diffusion coefficient and cellular uptake of glucose did not affect the different modes of sensor failure once the capsule has been fully formed. To exclude certain features of capsule formation will allow for more focused designs and experiments in the future. Therefore, the work presented here should promote more rational design of modified sensor surfaces to control immune responses, ultimately extending the useful life of implantable glucose sensors.

Chapter 4. Characterization of the Early Stage Effects of Implantation on Glucose Sensor Performance

4.1 Synopsis

While the effects of fully formed capsular tissue on sensor response have been addressed in Chapter 3, there has been little done to understand how tissue interactions occurring before mature capsule formation hinder sensor performance. The goal of this chapter is to provide a mechanistic understanding of the effects of early stage tissue reactions on implanted glucose sensor function. When taken in concert with the results of Chapter 3, these findings will provide a more complete temporal profile of the interactions between the sensor and the surrounding tissue as well as consequential downstream outcomes on sensor response.

Upon insertion in subcutaneous tissue the sensor is bathed in blood. Using human whole blood as a simple *ex vivo* experimental system, the impacts of protein accumulation at the sensor surface (biofouling effects) and cellular consumption of glucose in both the biofouling layer and in the bulk (metabolic effects) on sensor response were assessed.

To this end, Medtronic Minimed SofSensor glucose sensors were incubated in whole blood, plasma diluted whole blood, and cell-free platelet poor plasma (PPP) to analyze the effects of different blood constituents on sensor function. Experimental conditions were then simulated using MATLAB to predict the relative impacts of biofouling and metabolic effects on the observed sensor responses.

It was found that the physical barrier to glucose transport presented by protein biofouling does not hinder glucose movement to the sensor surface. Moreover, the consumption of glucose by inflammatory cells, and not erythrocytes, proximal to the sensor surface had a substantial effect on sensor response and may be the main culprit for anomalous sensor behavior immediately following implantation.

4.2 Introduction

In order to bring a more complete description to sensor behavior in subcutaneous tissue, the author previously presented a computational transport model to elucidate the effects that constituent parts of fully formed capsular tissue have upon a transcutaneous sensor's ability to accurately measure glucose values in real time [58]. However, a more complete understanding of the effects of tissue interactions on sensor function should also include events that occur prior to mature capsule formation. Clinically, this time frame is of particular importance because it coincides with the 3-7 day window of FDA approval for all commercially available continuous glucose monitoring systems [6, 7, 59, 60].

Upon insertion these sensors are bathed in blood and the sensor surface becomes fouled with blood plasma proteins and blood borne cells. Klueh, et al. recently reported a series of experiments using sensors from both Abbott Diabetes Care and DexCom that examined this interaction by immersing transcutaneous sensors in unheparinized and heparinized whole blood. All of the sensors exhibited a temporal decay in glucose

signal, which they attributed to glucose consumption by erythrocytes accumulated at the sensor surface [23]. More recently, this group conducted *in vivo* studies on the role of erythrocyte embedded clots on sensor function in mice [61].

Similar to Klueh, et al., in the current study, the effects of protein biofouling and cellular accumulation were observed experimentally by recording the changes in response of commercially available Medtronic MiniMed SofSensors in heparinized whole blood and various blood constituents. Numerical simulations were then used to further predict physiological scenarios that could be used to explain the experimental observations.

4.3 Materials and Methods

4.3.1 Blood Sample Preparation

In accordance with IRB protocol 2257-08-1R17ER, samples of human blood from healthy volunteers were collected in 10 mL vacutainers containing EDTA to prevent immediate coagulation. Upon collection, samples were immediately used for studies, as platelet counts have been shown to decrease by over 50% after 72 hours *ex vivo* [62]. Extra measure was taken to further ensure that no coagulation takes place by adding a heparin sulfate stock solution at 100 U/mL in PBS (-/-) to the blood to achieve a final heparin concentration of 5 U/mL. This final concentration is higher than the recommended dosage for treatment of 0.4 U/mL to ensure a well-stirred solution for the subsequent long term studies [63].

Blood constituent samples were prepared through the fractionation of blood via centrifugation using an existing protocol from Weibrich, et al. to gather platelet rich plasma (PRP) and PPP for studies. PRP is the volume of blood that is absent erythrocytes and leukocytes but contains platelets, small molecules and plasma proteins. PPP, however, contains only small molecules and plasma proteins. PRP was obtained from centrifuging whole blood for 10 minutes at 1500 rpm and then removing the hematocrit. PPP was obtained from centrifuging PRP for 15 minutes at 3600 rpm to remove the platelets. By having different constituents of blood, the contributions of both the plasma and whole blood to sensor function could be delineated.

Plasma diluted blood was prepared as a 1:11 dilution of whole blood in its own plasma. This dilution produced a cell concentration of $5x10^5$ cells/mL, which is a common value for white blood cell concentrations in whole blood [64]. PPP was chosen for the blood diluent as it should not dilute the glucose concentration of the sample while diluting the cell concentration.

4.3.2 Glucose Sensor Calibration

Two Medtronic SofSensors (Medtronic Diabetes Care, Northridge, CA) were first immersed in a stirred PBS bath at 37°C initially at 0 mg/dL glucose. To calibrate each sensor, glucose was added to increase the concentration to 100 mg/dL and a baseline current was allowed to form. This step was then repeated for 200 mg/dL of glucose. From these three data points (0, 100, 200 mg/dL glucose), a linear calibration curve

relating glucose concentration to sensor output current could be made. Besides allowing for concentration readings, this calibration step served as a check that the sensors were properly working, as the sensors were reported by the manufacturer to have a linear response to glucose incursions for a range of 0-400 mg/dL glucose.

4.3.3 Whole Blood and PPP Studies

Once calibration was completed, the sensors were transferred from the PBS bath to one of two 10 mL samples of either gently stirred whole blood or PPP at 37°C. This incubation was carried out until a baseline was formed, which took about 10 hours. During the ten hour incubation, blood and PPP glucose concentrations were measured periodically via test strips (OneTouch Ultra, Johnson & Johnson, Milpita, CA) to ensure that the sensors were accurately recording trends in each test group. To examine whether blood and PPP allow sensors to behave in a stepwise, nonreactive fashion like PBS, glucose incursions were made to double the glucose in the system. Sensors were then allowed to gather a baseline over six hours and the process was repeated. Test strip measurements were made at the beginning and the end of each incursion to see if sensor response mimicked a direct blood glucose concentration measurement. After the blood incubation, both sensors were "post-calibrated" in a stirred PBS bath at 37°C using the same process as the pre-calibration. This study was repeated three times (n=3).

4.3.4 Whole and Dilute Blood Studies

To examine the effect of cell number and consumption upon sensor readings, sensors were immersed in both whole and dilute blood. After the same PBS calibration step described above in §4.3.2, two sensors were submerged in one of two test solutions. The first solution was heparinized whole blood prepared as described in §4.3.1. The second solution was blood diluted 1:11 in its own PPP, which should not dilute the glucose concentration of the sample while diluting the cell concentration. The sensor treatment protocol followed the same layout as in §4.3.2 and §4.3.3. This study was repeated three times (n=3).

4.3.5 Data Collection, Calibration and Statistical Analysis

All sensor signals were sorted and plotted using custom scripts written in MATLAB (The Mathworks, Natick, MA). Calibration curves were calculated as a linear fit by using the "polyfit" command in MATLAB. An analysis of covariance (ANCOVA) was performed in MATLAB to assess significant differences in the slopes of the linear portions of the sensor signal during incubation in different blood constituents ($p<0.05$).

4.3.6 Computational Modeling of Cellular Glucose Consumption

To complement experimental findings, a numerical simulation of the experimental setup above was derived and implemented using MATLAB. Figure 9 presents a schematic representation of the model used in this study, which was modified from the model presented in a previous article by this group [58]. Briefly, transport of

glucose through the environment surrounding the sensor was treated as a two compartment construct. The first compartment, the one closer to the sensor with respect to distance, was the biofouling layer (C_{layer}), a thin layer of proteins and adherent/entrapped cells that forms in within minutes of blood exposure. The second compartment (C_{bulk}) was the bulk blood surrounding the sensor and its biofouling layer. Values for all constants are defined in Table 5.

4.3.6.1 Governing Equations

The governing equation describing glucose concentration in the cellular region of the biofouling layer (C_{layer}) is a non-linear, uni-dimensional diffusion-reaction equation in cylindrical coordinates through a porous medium. It has a diffusion term and a sink term to describe uptake by adherent cells (Eq. 15).

$$\frac{\partial C_{layer}(r,t)}{\partial t} = \frac{D_{layer}}{r}\frac{\partial}{\partial r}\left(r\frac{\partial C_{layer}(r,t)}{\partial r}\right) - Q_{layer}(r,t) \tag{15}$$

Q_{layer} is defined as the rate of glucose uptake by cells in the layer and is modeled by Michaelis-Menten kinetics, where $V_{max,layer}$ is the maximum rate of consumption (μmol/(cell-sec)), $K_{M,layer}$ is the Michaelis-Menten constant (μmol/ L), ε_{layer} is the porosity of the biofouling layer (unitless), and z_{cell} is the volume of a cell within the layer (L/cell) (Eq. 16). In this model, the fibrin network and cells were assumed to be well mixed within the biofouling layer. Therefore, they were not considered separately.

$$Q_{layer}(r,t) = \frac{V_{\max,layer}C_{layer}(r,t)}{K_{M,layer}\varepsilon_{layer} + C_{layer}(r,t)}\left(\frac{1-\varepsilon_{layer}}{z_{cell}}\right) \tag{16}$$

The governing equation for glucose concentration in the bulk blood (C_{bulk}) is a non-linear, uni-dimensional diffusion-reaction equation in cylindrical coordinates through a porous medium (Eq. 17).

$$\frac{\partial C_{bulk}(r,t)}{\partial t} = \frac{D_{bulk}}{r}\frac{\partial}{\partial r}\left(r\frac{\partial C_{bulk}(r,t)}{\partial r}\right) - Q_{bulk}(r,t) \tag{17}$$

Q_{bulk} represents the consumption rate of glucose by native red blood cells in the bulk space and is modeled with Michaelis-Menten kinetics as well, where $V_{max,bulk}$ is the maximum rate of glucose consumption (μmol/(cell-sec)), $K_{M,bulk}$ is the Michaelis-Menten constant (μmol/L), ε_{bulk} is the porosity of the blood (unitless), and z_{cell} is the volume of a red blood cell (L/cell) (Eq. 18). This term represents a glucose sink, as uptake of the analyte by cells removes it from the system.

$$Q_{bulk}(r,t) = \frac{V_{\max,bulk}C_{bulk}(r,t)}{K_{M,bulk}\varepsilon_{bulk} + C_{bulk}(r,t)}\left(\frac{1-\varepsilon_{bulk}}{z_{cell}}\right) \tag{18}$$

4.3.6.2 Definition of Porosity of Biofouling Layer and Bulk Compartments

The porosity of the acellular biofouling layer (ε_{layer}) was calculated using the specific hydraulic permeability (k) of a fibrin network, which has been reported by Carr, et al. to be within the range of 2 to 7 x10^{-10} cm^2 [65]. For a network of randomly oriented fibers, the specific hydraulic permeability is calculated with Equations 19 and 20, where ε is ε_{layer} for the simplification of the equation description [66].

$$k = \frac{{r_f}^2\varepsilon^3}{4G(\varepsilon)(1-\varepsilon)^2} \tag{19}$$

$$G(\varepsilon)=\frac{2\varepsilon^3}{3(1-\varepsilon)}\left\{\frac{1}{-2\ln(1-\varepsilon)-3+4(1-\varepsilon)-(1-\varepsilon)^2}+\frac{2}{-\ln(1-\varepsilon)-\frac{\left[1-(1-\varepsilon)^2\right]}{\left[1+(1-\varepsilon)^2\right]}}\right\} \quad (20)$$

As the radius of a fibrin strand (r_f) is known to be 150 nm, ε_{layer} can be found for the range of reported k [67]. For the model, ε_{layer} was chosen to be 0.91 as it represented a midpoint of the calculated porosity values. The porosity of the bulk space, ε_{bulk} , was set to be 0.55, one minus the volume fraction occupied by the hematocrit (45 % of the volume of blood).

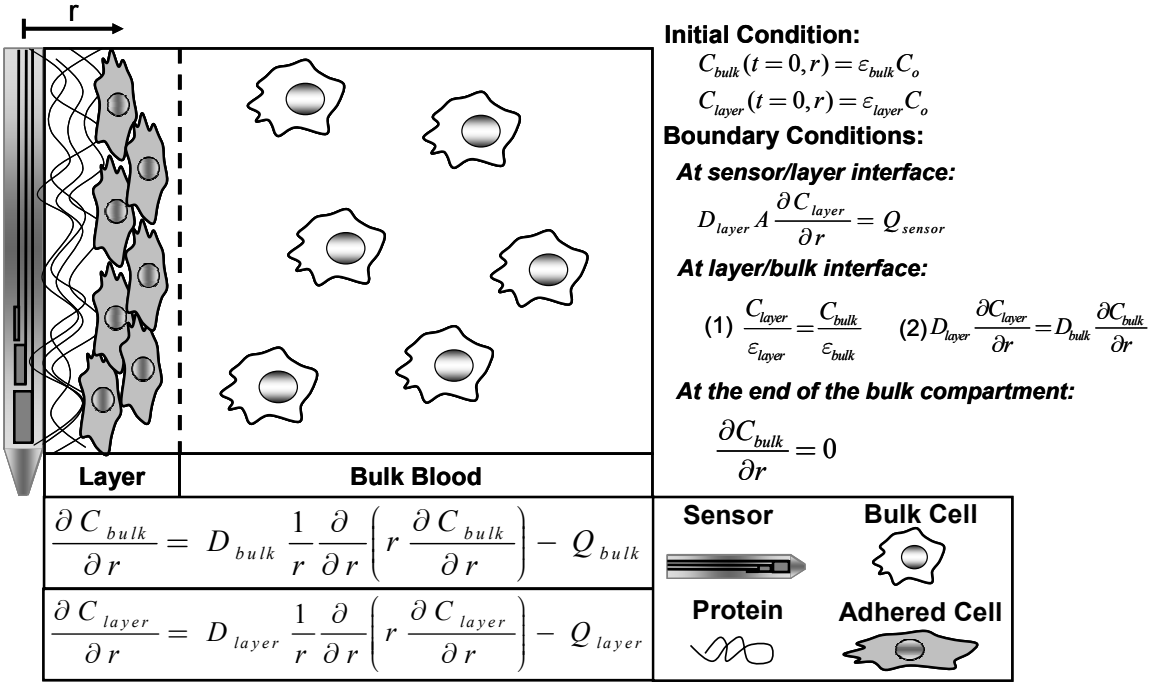

Figure 9: Schematic representation of diffusion through bulk blood and a layer of adsorbed proteins and cells.

Table 5: List of all baseline model parameters. Values listed with * in the citation column are model assumptions while those listed with ** are calculated values with no previous citation.

Model Parameters	Parameter Values		
	Biofouling Layer	Bulk Blood	Citation
Diffusion Coefficient (D) (cm^2/sec)	$1.87x10^{-6}$	$3.5x10^{-6}$	[58]
Porosity (ε) (unitless)	0.91	0.55	**
Layer Thickness (L) (μm)	75	-	[58]
Michaelis Menten Constant (K_M) (μM)	$6.13x10^{3}$	$4x10^{3}$	[28, 68]
Maximal rate of cellular glucose uptake (V_{max}) (μmol/(cell-sec))	$4.88x10^{-11}$ /$1.357x10^{-12}$	$1.357x10^{-12}$	[28, 68]
Permeability of biofouling layer (P_{layer}) (cm/sec)	$5x10^{-3}$	-	*
Conversion constant (λ) (mol/(mM-sec))	$2.574x10^{-14}$	-	[58]
Cell Volume (z_{cell}) (L/cell)	$9.5x10^{-13}$	-	[58]
Glucose Sensor Radius (a) (cm)	0.07	-	[58]
Sensor Surface Area (A) (cm^2)	0.0058	-	[58]

4.3.6.3 Initial and Boundary Conditions

For the initial condition, it was assumed that the diffusion time in the biofouling layer was much shorter than the time scale of simulation. Therefore, the initial condition for the system was a uniform glucose concentration (C_o) multiplied by the porosities of

each compartment when the sensor is inserted into the blood at t = 0 sec, a plausible assumption as there was no other intrinsic source of glucose once a sample of blood was taken for an experiment. The boundary condition at the sensor/layer interface was that the flux of glucose diffusion in the biofouling layer times the surface area (A) was equal to the rate of glucose uptake by the sensor, Q_{sensor}. At the interface of the biofouling layer and bulk regions, it was assumed that there was no consumption or accumulation of glucose, so the concentrations normalized by the porosities and fluxes were continuous across the interface. No flux boundary conditions were assigned to the outer boundary condition at the end of the bulk compartment because glucose could not move into or out of the boundary at the edge of the beaker, creating an insulating boundary and making the flux at the outer boundary equal to zero.

4.3.6.4 Glucose Uptake Parameters

Glucose uptake was considered an enzymatically mediated event, and was thus modeled using Michaelis-Menten kinetics [58]. These simulations assumed that the glucose consuming cells in the biofouling layer were, depending on the scenario, either inflammatory cells or erythrocytes while the cells in the bulk were erythrocytes. Thus the $V_{max,bulk}$ was set to 1.36×10^{-12} μmol/(cell-sec), the reported value of maximal glucose consumption rate for human erythrocytes, as reported by Yang, et al. [68]. The baseline $V_{max,layer}$ value used for these calculations was either 4.88×10^{-11} μmol/(cell-sec) as reported by Ahmed, et al. for glucose uptake by human macrophages during inflammation or the

erythrocyte value reported by Yang, et al.[28]. The V_{max} of the inflammatory cell was chosen to be that of a macrophage, but it is worth noting that other leukocytes such as lymphocytes and neutrophils, have similar glucose uptake kinetics [69, 70].

Five computational scenarios (Table 6) were examined to compare the effect of glucose consumption by different cell types (inflammatory cell or erythrocyte) within the biofouling layer and the bulk blood. The results of these simulations were then compared directly to two experimentally measured normalized sensor signals in whole blood from Figure 11 (the maximal decline following addition of the sensor and the minimal decline after a glucose addition to show a range of declines) to find which cell type had the dominant effect on decreased sensor signals. To investigate the ability for the proteins within the biofouling layer to act alone as a diffusive barrier for glucose transport to the sensor surface, the simulation was run with both $V_{max,layer}$ and $V_{max,bulk}$ set to zero, creating an *in silico* analog to the PPP studies.

Table 6: Outline of five different computational scenarios for glucose transport to an indwelling sensor. To represent these changes in cell type, the Michaelis-Menten kinetic values of V_{max} and K_m were changed accordingly.

	Biofouling Layer Cell Type	**Bulk Blood Cell Type**
Scenario 1	Macrophage	Erythrocyte
Scenario 2	Macrophage	None
Scenario 3	None	Erythrocyte
Scenario 4	Erythrocyte	Erythrocyte
Scenario 5	Erythrocyte	None

4.3.6.5 Modeling Biofouling Layer Glucose Depletion Zone Formation

To investigate the spatial effect of inflammatory cell aggregation and glucose consumption on sensor readings, glucose concentration profiles were plotted with respect to distance for different values of $V_{max,layer}$. The maximal glucose uptake rate of the cells in the layer ($V_{max,layer}$) was varied amongst four different values: (1) V_{max}=0: representative of only an acellular protein biofouling layer, (2) V_{max} for erythrocytes, (3) V_{max} for macrophages and (4) twice the V_{max} for macrophages. The last case was considered to assess the possible effect of increased cellular accumulation at the sensor interface.

4.3.6.6. Numerical Methods

Governing partial differential equations in the simulations were discretized into a series of ordinary differential equations using the finite difference method. Differential equations from all above studies were solved using the differential equation solver, ode15s, in MATLAB.

4.3.7 Scanning Electron Microscopy of Sensor Surface

The protocol for scanning electron microscopy (SEM) of the sensors was modified from Nurdin, et al. [71]. Clean Medtronic MiniMed SofSensors were incubated in freshly collected whole blood and PPP treated in the manner described in §4.3.3 for 24 hours at 37°C. After the end of the incubation period, the sensor tips were fixed in 1.5% glutaraldehyde in PBS for four hours at room temperature. The samples were subjected

to a series of dehydration steps in solutions of ethanol of increasing concentration before treatment with tetramethylsilane. The treated sensor underwent gold sputter coating to a thickness of 7 μm before being imaged on a scanning electron microscope (FEI XL30 SEM-FEG).

4.4 Results

4.4.1 Whole Blood, Dilute Blood and PPP Studies

Figure 10 shows the reproducibility of results from submerging sensors in whole blood. For both trials, signals initially declined upon immersion in whole blood. Moreover, when glucose is added to the system, the signal does not maintain a step increase like in the pre-calibration immersion in glucose-spiked PBS. Post-calibration steps verified that sensor functionality was maintained throughout the course of the immersion. This anomalous response in whole blood spurred further experiments where sensors were immersed in different blood constituents.

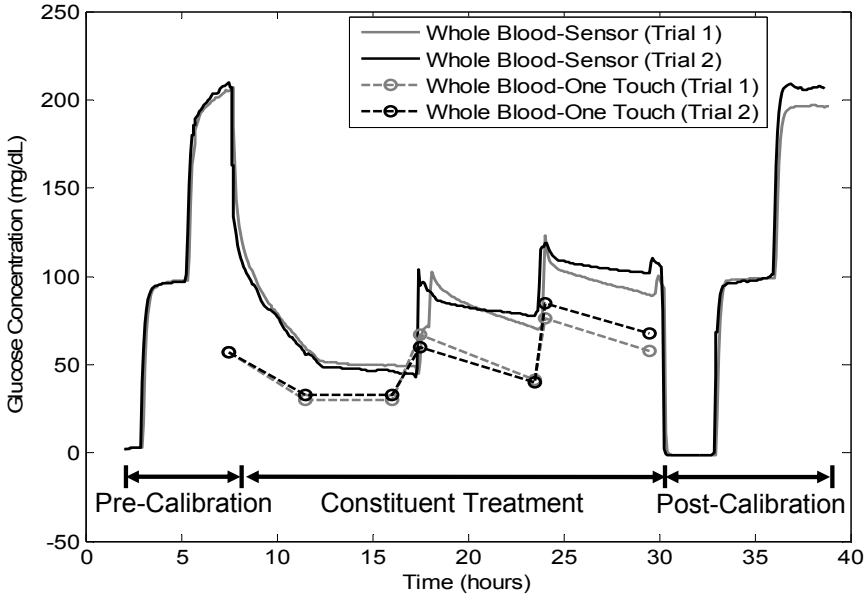

Figure 10: Sample behavior of Medtronic MiniMed sensors when incubated in whole blood.

Figure 11 shows mean continuous glucose sensor measurements in whole blood (blue solid trace), PPP (red solid trace) and dilute blood (black solid trace) derived from the same stock of whole blood, as well as discrete glucose concentrations sampled by test strips for each (open circles). After pre-calibration, one sensor was immersed in PPP and the other was immersed in whole blood. Using an ANCOVA, the slope of the initial sensor decline in whole blood was found to be statistically significantly different from the initial decline in the PPP case. Doubling the whole blood glucose at 16 hours and 24 hours caused jumps in sensor signal followed again by signal decays that were also statistically significant from their complementary PPP traces. Even though the magnitude of the corresponding test strip glucose concentrations was always lower, it is

important to note that the slopes of the signal declines were found to not be statistically significant from the corresponding test strip measurements.

The PPP-immersed sensor behaved essentially as if it was immersed in PBS. This finding suggests that no glucose was being removed from the system in PPP and that adsorption of plasma proteins to the sensor surface during whole blood immersion was not contributing to the decreased sensor response in whole blood. Because the only difference between PPP and whole blood is the population of cells, the observed declines in whole blood sensor signal relative to PPP would be the result of cells within the system consuming glucose.

The sensor in PPP-diluted blood exhibited an intermediate sensor response when compared to the whole blood case. Similar to the sensor in whole blood, the sensor in PPP-diluted whole blood exhibited signal declines upon immersion and following glucose bolus additions, albeit with slopes significantly less than whole blood for all three cases of decline ($p<0.05$). These results indicate that the cells in PPP-diluted blood were also consuming glucose but to a lesser extent than in whole blood presumably due to the effects of dilution, further demonstrating the effects of cellular consumption on sensor signal. These findings were also corroborated by test strip measurements at discrete time points.

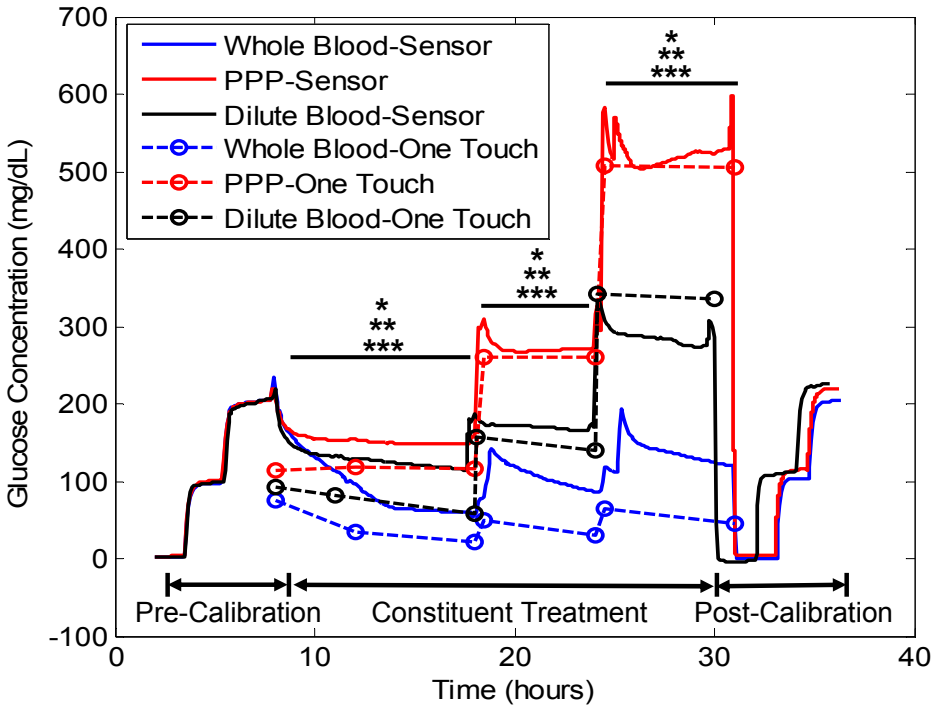

Figure 11: Comparison of mean glucose sensor readings in platelet poor plasma (red), whole blood (blue) and dilute blood (black) as a function of time (n=3). Sensor readings are corroborated by One Touch readings for each (-o-). * indicates statistically significant differences in slopes of sensor signals between whole blood and PPP incubations ($p<0.05$). ** indicates statistically significant differences in slopes of sensor signals between dilute blood and PPP incubations ($p<0.05$). * indicates statistically significant differences in slopes of sensor signals between dilute blood and whole blood incubations ($p<0.05$).**

4.4.2 Numerical Modeling

The dashed lines in Figure 12 display the maximal and minimal fractional experimental signal declines as derived from the data in Figure 11, where the sharper decline occurred following the initial sensor immersion and the shallower decline occurred following an addition of glucose. The space between them shaded grey is meant to represent the range of sensor declines observed when immersed in whole

blood. The solid lines in Figure 12 are simulated fractional declines in sensor signal with respect to time for five distinct scenarios of cellular presence around the sensor (Table 6).

The erythrocyte-only simulations – be they in the bulk (red), in the layer (cyan), or both (black) – all underestimate the initial ~60% sensor decline following the sensor immersion in whole blood and the ~40% experimental decline post glucose addition. However, when the simulations include just adherent macrophages, the simulations lie within the range of experimental sensor declines in whole blood. The simulation with adherent macrophages and bulk erythrocytes overestimates both experimental declines. These data suggest that adherent macrophages are more likely the primary mitigators of the initial sensor decline, and not adherent erythrocytes as originally suggested by Klueh et al. [23, 61].

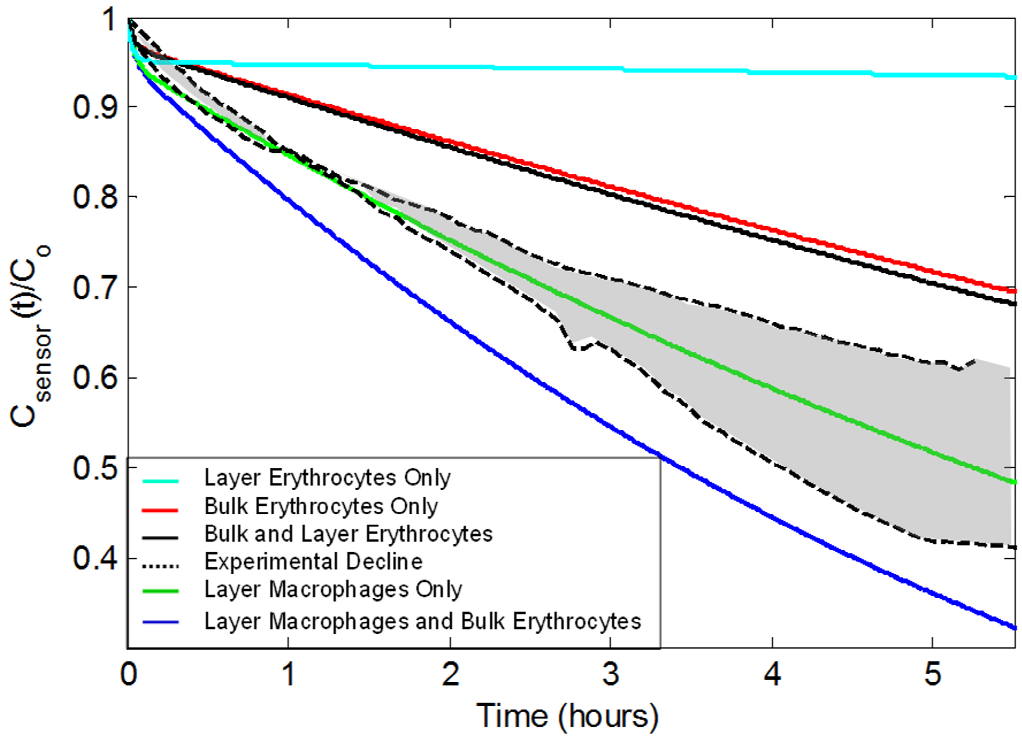

Figure 12: Simulated sensor reading as a function of time. The ordinate is represented as the fraction of initial glucose in the system and the abscissa is time in hours. The simulation compares five different scenarios against the range of maximal and minimal experimental sensor declines in whole blood from Figure 3 (shaded grey area bounded by dotted lines) to determine which group of cells contribute most to glucose depletion in each case. Scenario 1 (blue line) is represented by the presence of macrophages in the layer and erythrocytes in the bulk. Scenario 2 (green line) is represented by the presence of only macrophages in the layer and no cells in the bulk. Scenario 3 (red line) is represented by the presence of only erythrocytes in the bulk with no macrophages in the layer. Scenario 4 (black line) is represented by the presence of only erythrocytes in both the bulk and the layer. Scenario 5 (cyan line) is represented by the presence of only erythrocytes in the layer and no cells in the bulk.

The trends in Figure 12 suggest that the cell-embedded biofouling layer may result in the formation of a glucose depletion zone adjacent to the sensor surface. Figure 13 contains a family of normalized glucose concentration profiles as a function of

distance extending from the sensor surface, through a representative 75 μm thick biofouling layer. When erythrocytes exist as the only cell type within the biofouling layer (black dot), the radial decrease in glucose concentration relative to the initial concentration is imperceptible, with a decrease of $9x10^{-5}$ %. This finding is nearly identical to the case where $V_{max,layer}=0$ (red squares), representing an acellular protein biofouling layer. However, when macrophages are the only cell type within the biofouling layer and $V_{max,layer}=V_{max}$ for macrophages (blue dot), glucose concentrations do decrease towards the sensor surface, with concentrations dropping by 4% over the length scale. Moreover, a doubling of the macrophage V_{max} within the layer, which is meant to represent the increased presence of inflammatory cells at the site of implantation, increased the magnitude of depletion by causing concentrations to drop by 8% over the length scale.

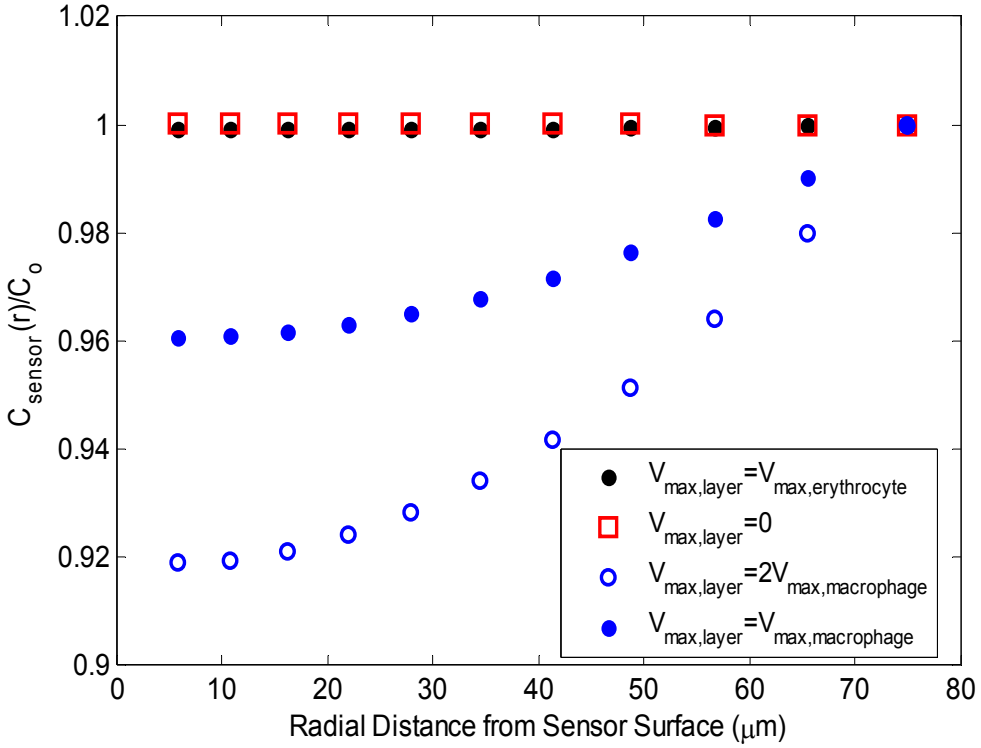

Figure 13: Simulated effects of adherent cell aggregation and glucose consumption on glucose concentration at the sensor surface as a function of distance. Increases in cell presence were modeled as an increase in $V_{max,layer}$ within the layer. When macrophages are the sole cell type in the adherent layer (blue circle), there is a depletion of glucose with respect to distance. This depletion increases as the number of macrophages increases, which is denoted by an increase in $V_{max,layer}$ to 2 $V_{max,macrophage}$ (blue open circle). When the adherent layer is populated by only erythrocytes (black circle), there is close to no radial depletion. This is similar to the acellular case where $V_{max,layer}=0$ (red open squares), indicating only a biofouling layer. Data presented as fractional signal decline.

Figure 14 displays a simulated fractional decline in sensor signal caused by the presence of an acellular protein adsorption layer with respect to time set against experimental sensor data from Figure 11 (black dashed line). Assuming a representative fibrin mat porosity of 0.91, the decrease in glucose concentration with respect to time

across the protein film was negligible. Dramatically decreasing the porosity to a physically unrealistic value of 0.1 had a more pronounced, but still small temporal effect on glucose transport to the sensor (>90% of the original value). Taken together, these results show that the protein film itself does not restrict the transport of glucose to the sensor surface.

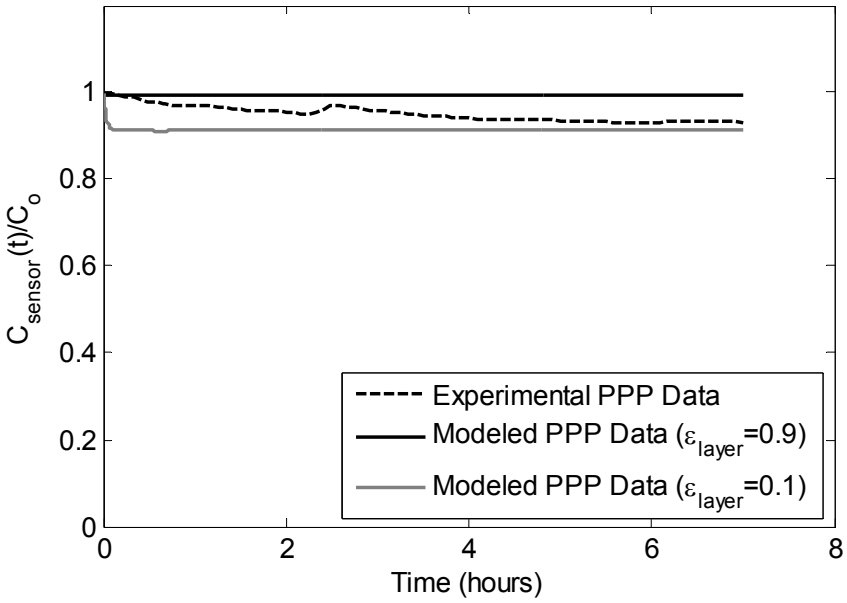

Figure 14: Simulated effects of the acellular biofouling layer as a diffusive barrier with respect to time. Data presented as a fractional signal decline.

4.5 Discussion

Building on the work of Klueh et al., the current study employed well-stirred whole blood as a simple *ex vivo* living system to approximate the environment in the first few hours of sensor implantation when bleeding, hemostasis and the adhesion of blood borne cells are dominant events around the sensor surface [23]. The use of whole

blood and PPP allowed for the separation of transport effects from metabolic effects arising from the accumulation of blood plasma proteins and blood borne cells at the sensor surface.

Trends in sensor values were compared across sensors by converting all sensor readouts from current to concentration. Post-calibration of sensors removed from whole blood or PPP as well as periodic glucose sampling taken with glucose test strips ensured that changes in sensor readings were an accurate reporting of glucose concentration in the surrounding milieu.

Figure 11 compares glucose readings for sensors immersed in whole blood, PPP, and diluted whole blood. With each addition of glucose into PPP, both the sensor and test strip readings registered steady step increases in glucose concentration. The results from the PPP incubation study were corroborated by a numerical simulation showing that the biofouling layer had little effect in limiting glucose transport to the sensor with respect to time (Fig. 14). This behavior in PPP was akin to measurements in buffered glucose solution, suggesting that the fouling of sensors by blood plasma proteins like those seen in the SEM image of Figure 15d was having no effect on the decrease in sensor signal.

In contrast, the sensor and test strip readings in whole blood registered sharp increases followed by declines after initial immersion and additions of glucose. Sensors in diluted whole blood exhibited a combination of step increases and signal declines

intermediate between that observed for PPP and whole blood. Clearly exposure to blood caused a decrease in blood glucose concentration that did not result from the accumulation of blood plasma proteins at the sensor surface or from a failure of the sensor to accurately read glucose; rather, these declines arose from a combination of sensor equilibration and cellular glucose consumption. As sensor output could be modulated by the concentration of cells within the blood, the role of cellular presence on sensor signal is apparent.

The ratio for erythrocytes to leukocytes in whole blood is roughly 1000:1; and as such, the SEM images of the biofouled sensor surface (Fig. 15) showed many more erythrocytes than leukocytes, but clearly not three orders of magnitude more [64]. In spite of their larger number, erythrocytes do not exhibit substantial metabolic requirements on a per cell basis as their net efflux of glucose is roughly that of the net influx [64, 72-74]. In contrast, activated immune cells have significant glucose demands [35, 36]. Therefore, it is reasonable to infer that accumulation of the more metabolically active leukocytes could more significantly affect the glucose concentration measured by the sensor. As Figure 12 demonstrates, the simulation that comprises adherent macrophages in the biofouling layer lies within the range of experimentally observed sensor declines. This suggests that inflammatory cells like macrophages, although fewer in number than erythrocytes, are the main determinant for a decrease in sensor signal with respect to time. It should be noted however that bulk erythrocytes, due to their

sheer number in blood, still consume a significant amount of glucose. However, the computational scenarios where only erythrocytes were present all underestimated the experimental sensor declines in whole blood.

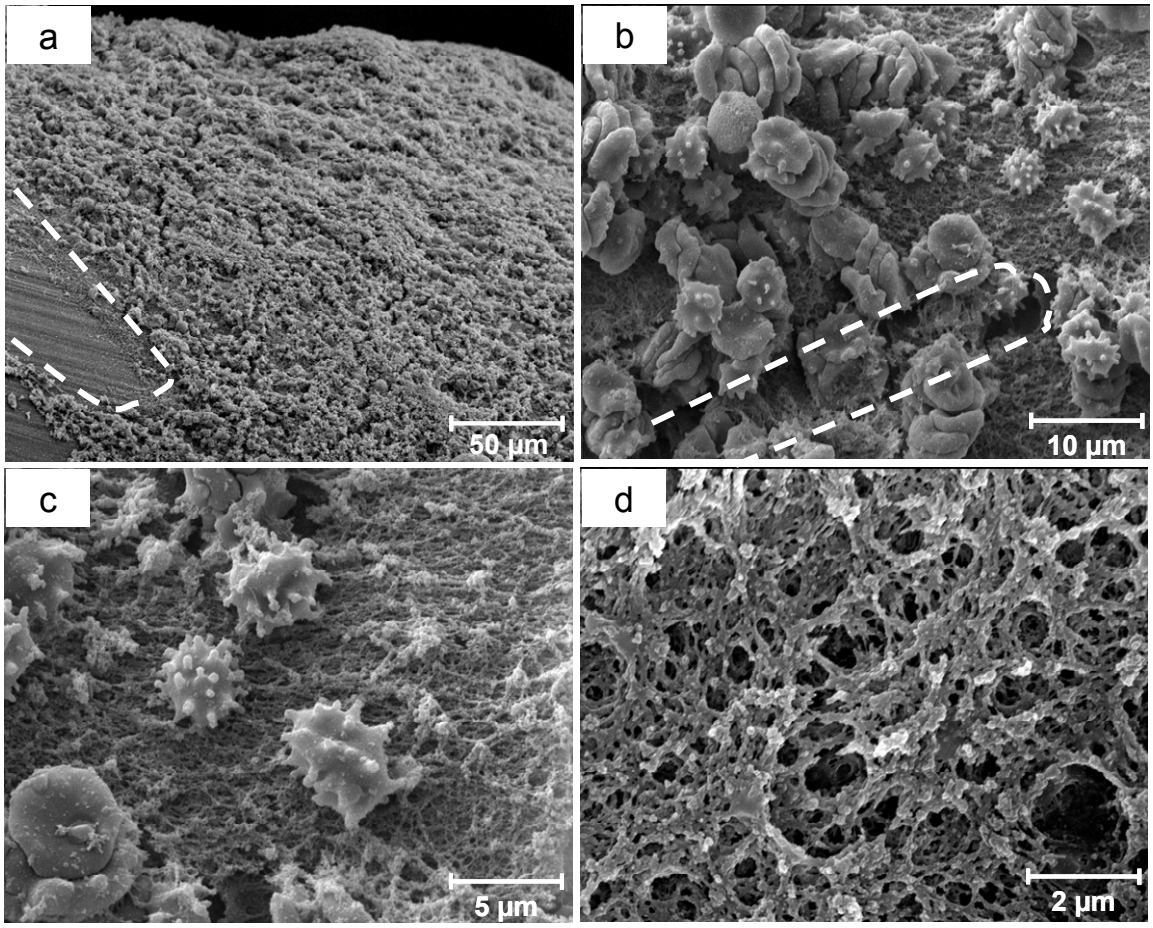

Figure 15: (a,b) SEM images of a blood clot on a sensor surface (1000x, 5000x).(c) SEM images of leukocyte adhesion on the sensor surface (10000x). (d) SEM image of protein adsorption layer on the sensor surface (20000x). Figure 15a shows the difference between regions covered in protein and cells and the bare sensor surface (outlined by dashed line). Note the infiltration of the active sensing region by cells and proteins in (b) (sensing region outlined by a dashed line).

Figure 13 further extends this conclusion by simulating the ability of erythrocytes and macrophages to induce a "glucose depletion zone" within the vicinity of the sensor

surface. When erythrocytes exist as the only cell type within the biofouling layer, the radial glucose concentration does not appreciably decrease, making it indistinguishable from the acellular case. Through this comparison, it is evident that erythrocytes do not create a glucose depletion zone. However, when macrophages are considered as the only cell type in the layer, depletion occurs with the magnitude of depletion increasing with increasing cellular presence. While the macrophage-mediated cases produce seemingly modest depletions, it should be noted that the time post-implantation at which these radial concentrations were modeled is merely hours after immersion of the sensor in whole blood. In an *in vivo* setting, this depletion in turn will inhibit the sensor from being able to accurately measure a patient's interstitial glucose.

Simulations were run to assess if the cellular component of the biofouling layer may have imposed some resistance to glucose transport. This increase in resistance due purely to the steric effects was addressed in Figure 14 where the porosity is decreased from 0.9 to 0.1. Even in this case, a steady state value of greater than 90% of the original glucose concentration was maintained throughout the length of the simulation. Such a finding suggests that while the presence of cells can confer transport resistance, the effects of this resistance are small compared to the consumptive effects seen in Figures 12 and 13.

Given the long-standing uncertainty of how the *in vivo* environment affects glucose sensor function, the current study provides a clearer picture of how protein and

cell accumulation at the sensor surface affects sensor performance in a living milieu. The whole blood, dilute blood and PPP studies in concert with the numerical findings suggest that while the sensors accurately measure the glucose that is able to freely diffuse to them, glucose consumption by inflammatory cells accumulated at the sensor surface consume the analyte before it can reach the sensor, thereby limiting sensing capability.

Finally, the sensors used in this study are specifically intended for insertion into subcutaneous tissue for continuous monitoring of interstitial glucose, and were not designed for sensing glucose in bulk blood. That said, these sensors accurately tracked accessible glucose in well-stirred whole blood and performed robustly throughout the study.

4.6 Conclusions

Whole blood, diluted whole blood, and PPP experiments indicated that decreases in sensor signal were attributable to the presence of glucose-consuming inflammatory cells proximal to the sensor surface. Moreover, the biofouling layer of adsorbed proteins on the sensor surface was shown to have no contribution to sensor signal declines. Computer simulations supported the experimental findings by demonstrating the effect that an aggregation of adhered cells has on creating a "glucose depletion zone" of glucose proximal to the sensor surface. The results of this body of work demonstrate that instead of sensors failing, as is often reported in the literature, that implant-

associated changes in the local environment are creating a scenario that inhibits otherwise functioning sensors from accurately sampling ambient interstitial glucose concentrations.

.

Chapter 5. Development of a Novel Biomimetic Construct of the *In Vivo* 3D Cellular Setting around the Sensor for the Focused *In Vitro* Investigation of Early Stage Effects of Implantation on Glucose Sensor Performance

5.1 Synopsis

Building upon the results of Chapter 4, the goal of Chapter 5 is to design, characterize and validate a novel benchtop *in vitro* system that can accurately recapitulate previously reported *ex vivo* results of sensor decline. To mimic the provisional matrix of proteins and inflammatory cells that forms around an implanted sensor, a cell-embedded fibrin gel was designed to surround the sensor. When embedded with macrophages, these fibrin gels contributed to sensor signal declines that were similar in both shape and magnitude to sensor signal declines when immersed in whole blood. Neither an acellular fibrin gel nor a gel embedded with cells whose glucose surface receptors had been blocked provided diffusive barriers to glucose transport, showing that the diminished signals from the presence of cell-embedded gels were metabolically-mediated. Additionally, gel constructs exhibited sensitivity to cell activation, as those embedded with macrophages that had been activated with both LPS and PMA demonstrated larger decreases in sensor signals than sensors surrounded by unstimulated macrophages. A computational model describing glucose transport through a cell-embedded fibrin gel was also built to validate the experimental findings by calculating the glucose uptake parameters necessary for such experimental declines.

5.2 Introduction

For implantable glucose sensors to be a more reliable and accessible option for diabetes management, their useful lives must be extended beyond the period of days that is the current standard in the industry. As all commercially available glucose sensors are approved by the FDA for no more than seven days *in vivo*, a small but growing body of literature is focusing on how tissue reactions in that time window occurring just days after implantation affect sensor function [75, 76]. Previously, work by the author demonstrated the negative impact that early stage inflammatory cell aggregation could have on sensor response in a whole blood *ex vivo* system [75]. Beyond creating a diminished signal with respect to time, the previous study demonstrated through computational modeling how the presence of a large amount of macrophages proximal to the sensor surface could create a "glucose depletion zone" where the interstitial concentration of glucose with respect to distance decreases near the sensor surface due to cellular glucose consumption.

Similarly, Klueh, et al. have investigated the potential deleterious effects of inflammatory cell aggregation on sensor response in a serious of studies [61, 75-78]. Using an *in vivo* murine system, Klueh, et al. have shown that sensors implanted in macrophage deficient and macrophage depleted mice demonstrated improved performance as compared to those implanted into normal mice [78]. A recent publication by the group also demonstrated the effect of macrophage presence on sensor

response *in vitro*. When simply injected near the sensor surface, macrophages generated enough of a consumptive sink to dramatically decrease sensor output relative to a non-treated sensor [77].

While both the work in Chapter 4 and the recent publications by Klueh, et al. are significant in elucidating the potential compromising effects of inflammatory cell accumulation on sensor response, each comes with caveats. With respect to the whole blood study, the mass of blood present as a result of implantation will be reabsorbed and cleared in a period of days *in vivo*, leaving inflammatory cells and blood borne proteins as the only capsular constituents present until the recruitment of fibroblasts and the deposition of extracellular matrix. A more physiologically relevant model of short term tissue response should include just the relevant proteins and cells. With respect to Klueh's *in vitro* assessment of macrophage presence, macrophages were simply ejected on to the sensor surface. A more complete *in vitro* model of early stage tissue response should incorporate all the relevant features of the provisional matrix in a three dimensional construct. In this way, the *in vivo* setting is more accurately recapitulated for analysis of sensor response.

In an attempt to build on the previous work in Chapter 4 as well as the recent advancements by Klueh, et al., we have developed a novel construct that can mimic the *in vivo* 3D cellular setting around the sensor for the focused *in vitro* investigation of early stage effects of implantation on glucose sensor performance vis-à-vis cellular glucose

consumption. This new *in vitro* construct is based upon a previously published technique for the fabrication of tissue engineered 3D muscle bundles from Bian, et al. [79]. This technique presents a number of features that can be used to create physiologically accurate, biomimetic surrogates of the provisional matrix surrounding an implanted sensor. First, the construct is comprised of a fibrin gel, making it particularly applicable for the study of glucose sensors as fibrin is the primary component of the protein biofouling layer that adsorbs onto the sensor surface immediately after implantation. Secondly, it is highly tunable and robust for both cell number and type. These cell-embedded gels have been demonstrated to be able to accommodate cellular concentrations over 10^7 cells/mL for various cell types including skeletal muscle, cardiomyocytes, stem cells and epithelial cells [79-82]. Lastly, cells within these fibrin gels have been shown maintain viability and functionality over a period of weeks post-fabrication [79].

With these design considerations in mind, we developed macrophage-embedded fibrin gels by incorporating a physiologically relevant 3D fibrin substrate with RAW 264.7 macrophages. Sensors were then inserted into these gels to examine their effects on sensor response. Results indicate that when inserted into macrophage-embedded gels, sensor declines mimic those declines reported in Chapter 4. Moreover, the sensor signal decline was shown to be metabolically regulated, and not an effect of limited diffusion of glucose to the sensor surface. These findings further demonstrate that the

environment around the sensor is acting as a sink for glucose, thus preventing the sensor from accurately sampling interstitial glucose. In the future, this well characterized *in vitro* surrogate for the provisional matrix may serve as a screening tool to test how different biologically-motivated surface design considerations could impact sensor response.

5.3 Materials and Methods

5.3.1 Fibrin Gel Fabrication

The design for the *in vitro* fibrin gel system is based upon a method developed by Bian, et al. for the construction of biomimetic three dimensional muscle tissue architectures [79]. Figure 16 outlines the experimental protocol for construction of the gels. The volume of these gels was specified to be 1 mL. Briefly, they were made by combining two solutions: (1) 200 μL bovine plasma fibrinogen (10 mg/mL, Sigma-Aldrich, St. Louis, MO), 100 μL Matrigel (BD Biosciences, Bedford, MA) and 480 μL of cells suspended in media at 4.2×10^6 cells/mL and (2) 240 μL of 2x cell media and 20 μL bovine thrombin (50 U/mL, Sigma-Aldrich, St. Louis, MO). Once diluted with the other reagents, the final cell concentration in the gel was 2×10^6 cells/mL. This value was chosen as it is representative of the histological density of inflammatory cells surrounding an area of inflammation and wound healing, as reported by Sisco, et al. [83]. The 2x media and thrombin solution was then pipetted into the cell solution to make a 1 mL volume. Once mixed, the full solution was quickly pipetted into a

cylindrical mold and allowed to crosslink for 30 minutes at 37°C. Before the addition of the non-crosslinked fibrin gel solution, each cylindrical mold was pre-treated with 0.2% (wt/vol) Pluronic F-127 (Sigma-Aldrich, St. Louis, MO) to prevent adhesion of the crosslinked gel to the mold. After fabrication, the gels were removed from the mold and incubated in cell media at 37°C for 24 hours before use. Cell viability within the gel was assessed and confirmed after experiments via fluorescent imaging. Hoechst 33342 dye, applied at a concentration of 1 μL/mL for 30 minutes at 37°C, was used to image all cell nuclei. Calcein AM dye, applied at a concentration of 2 μL/mL for 30 minutes at 37°C, was used to image all live cells. Ethidium homodimer-1, applied at a concentration of 2 μL/mL for 30 minutes at 37°C, was used to image all dead cells. All fluorescent reagents were purchased through Invitrogen (Eugene, OR).

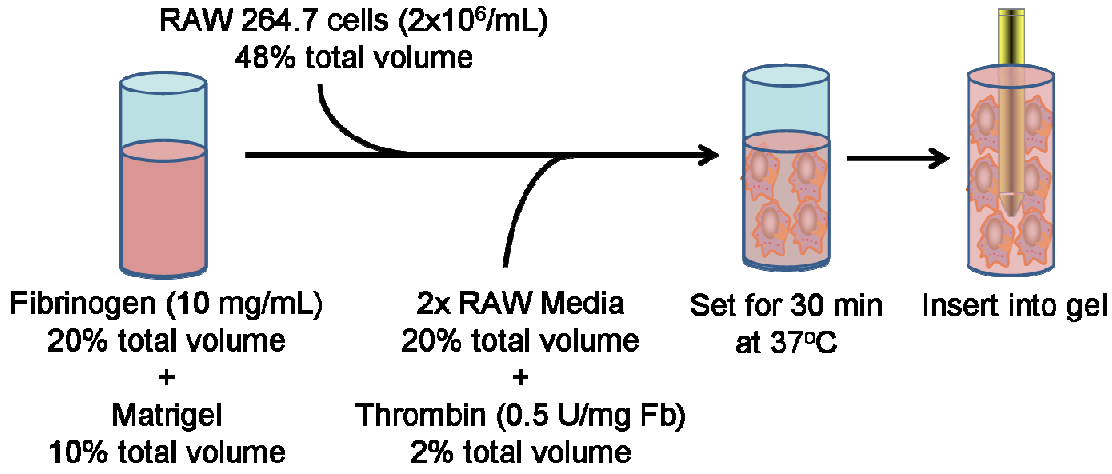

Figure 16: Outline of Fabrication of Cell-Embedded Fibrin Gels

5.3.2 Cell Culture

Two different cell types were incorporated into the fibrin gels for these studies. The first cell type was the RAW 264.7 murine macrophage cell line (ATCC, Manassas, VA). This cell type was chosen as the model inflammatory cell in this study. The second cell type was the 3T3 murine fibroblast/pre-adipocyte cell line and was used as an alternate cell type in the subsequent sensor studies to investigate the effects of cell type on sensor response. Both cell types were cultured in low glucose (100 mg/dL) Dulbecco's Modified Eagle's Medium (DMEM, Sigma Life Sciences, St. Louis, MO) supplemented with 10% (v/v) fetal bovine serum (Sigma-Aldrich, St. Louis, MO), penicillin (50 U/mL) and streptomycin (100 μg/mL) at 37°C and 5% CO_2.

5.3.3 Functional Sensor Testing with Fibrin Gels

The sensor used in this study was the same commercially available Medtronic Minimed SofSensor used in the studies outlined in Chapter 4. Similar to the protocols in Chapter 4, sensors went through a pre-treatment calibration stage to allow for sensor equilibration. In these instances, each sensor was incubated in low glucose (100 mg/dL) DMEM cell media for four hours to allow a steady state, baseline current to form. As sensors were not interrogated with subsequent additions of glucose, a multi-step calibration was not performed as in Chapter 4. Additionally, the findings of Chapter 4 verified the predictable, linear relationship between sensor current and calibration. Once a baseline current had been reached for a given sensor, the sensor probe would be

inserted into the top of a cylindrical fibrin gel. Special care was taken to ensure that the whole sensing region of the sensor was surrounded by the gel. The gel-covered sensor was then placed back in the low glucose media and allowed to gather current readings for 24 hours.

To test the capacity of cell-embedded fibrin gels to diminish sensor signals, four different cases were initially tested during the treatment phase: (1) treatment with a macrophage-embedded gel with a cell concentration of $2x10^6$ cells/mL, (2) treatment with a fibroblast-embedded gel with a cell concentration of $2x10^6$ cells/mL, (3) treatment with an acellular gel or (4) treatment with no gel on the sensor surface. Figure 17 represents the four different cases being tested. All media in which these cases were were well-stirred to avoid the formation of any boundary layers.

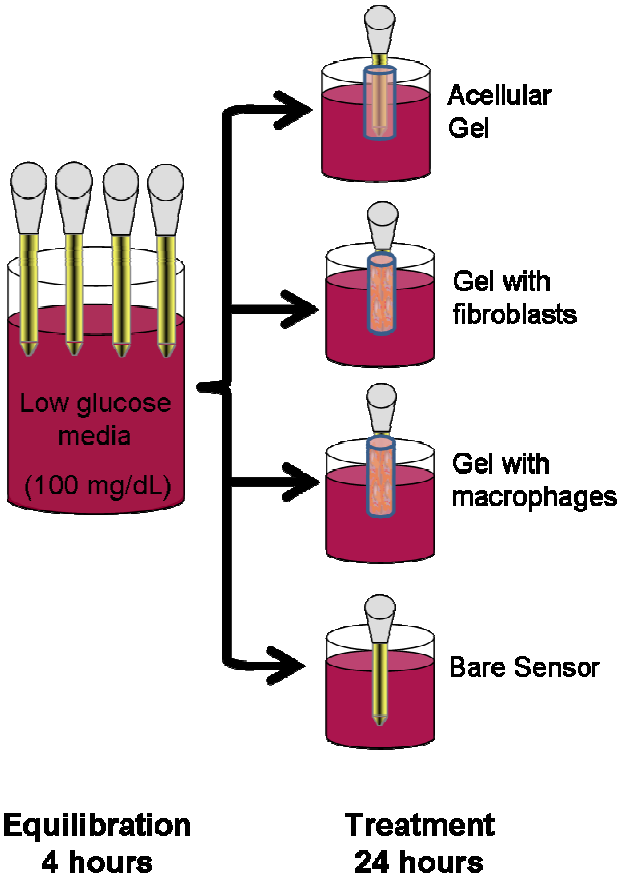

Figure 17: Outline of functional testing of the effect of fibrin gels on sensor performance

5.3.4 Effects of Inflammatory Activation of Macrophages on Sensor Signal

To more accurately recapitulate the *in vivo* post-implantation environment around the sensor, macrophages were activated to a more inflammatory phenotype before being embedded in gels. Macrophages were stimulated with either LPS (1 μg/mL, Sigma-Aldrich, St. Louis, MO) for 24 hours or PMA (50 nM, Sigma-Aldrich, St. Louis, MO) for 72 hours to activate inflammatory pathways and upregulate extracellular glucose uptake prior to gel fabrication. Stimulation times were based upon previously

reported protocols by Schutte, et al. [84]. Additionally, macrophages were stimulated with genistein, a naturally occurring isoflavone in soybeans and tyrosine kinase inhibitor that has been shown to decrease both inflammatory cytokine production as well as extracellular glucose uptake in LPS-stimulated RAW 264.7 macrophages [28, 85-87]. Macrophages were stimulated with genistein at a concentration of 100 μM for 24 hours before gel fabrication. In addition to testing the effects of cell activation, these cases further examined whether observed signal declines were a result of cellular glucose uptake or steric exclusion of the analyte due to decreased void space in the gel.

Similar to the protocol in the above section, once a baseline current had been reached for a given sensor, the sensor probe would be inserted into the top of a cylindrical fibrin gel. Special care was taken to ensure that the whole sensing region of the sensor was surrounded by the gel. The gel-covered sensor was then placed back in the low glucose media and allowed to gather current readings for 24 hours. All media in which these cells were incubated were well-stirred to avoid the formation of any boundary layers.

5.3.5 Statistical Analysis of Experimental Data

Each case described above was repeated to have a sample size of n=3. Data points were verified for being from a normal distribution using a Jarque-Bera test in MATLAB with the command "jbtest" for a value of $p<0.05$. This test is preferred over other normality tests when comparing datasets of small sample sizes as it minimizes the

occurrence of Type I errors. Data are presented as means ± standard deviation. A one-way repeated measures analysis of variance (ANOVA) was conducted to assess statistical significant differences amongst treatments ($p<0.05$) in MATLAB. Bonferroni's multiple comparison tests at a familywise error rate of 0.05 were then performed for post hoc analysis.

5.3.6 Validation of the *In Vitro* Fibrin Gel Results through Computational Modeling

To validate the experimental design, a numerical simulation of the experimental setup above was derived and implemented using MATLAB. Figure 18 presents a schematic representation of the model used in this study, which was modified from models presented in previous articles by the author [58, 75]. Briefly, transport of glucose through the environment surrounding the sensor was treated as a two compartment construct. The first compartment, the one closer to the sensor with respect to distance, was the gel layer (C_{gel}), a thin layer of the fibrin based gel and entrapped cells that surrounds the sensors during the experiment. The second compartment (C_{media}) was the media surrounding the sensor and gel. Values for all constants are defined in Table 7.

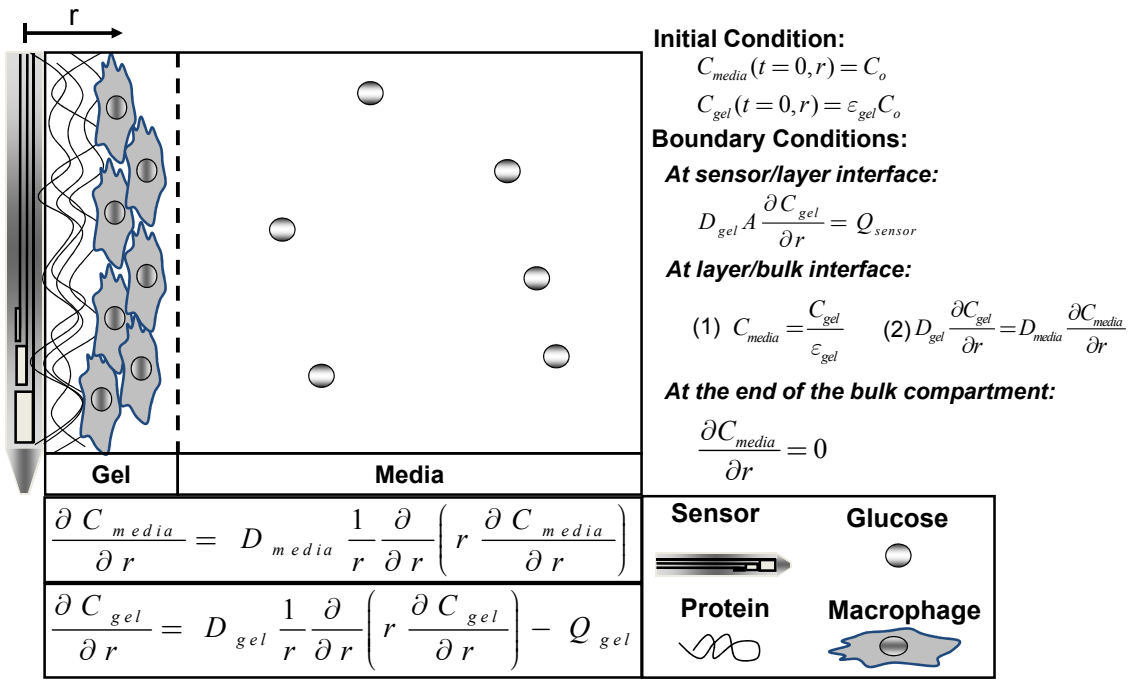

Figure 18: Schematic of computational model for the validation of fibrin gel results

Table 7: List of all baseline model parameters for computational model. Values listed with ** are calculated values with no previous citation.

Model Parameters	Parameter Values		
	Gel Layer	Media	Citation
Diffusion Coefficient (D) (cm^2/sec)	$6.8x10^{-6}$	$6.8x10^{-6}$	[88]
Porosity (ε) (unitless)	0.975	-	**
Layer Thickness (L) (cm)	0.43	-	**
Michaelis Menten Constant (K_M) (μM)	$6.13x10^{3}$		[28]
Maximal rate of cellular glucose uptake (V_{max}) (μmol/(cell-sec))	$4.88x10^{-11}$		[28]
Conversion constant (λ) (mol/(mM-sec))	$2.574x10^{-14}$	-	[58]
Cell Volume (z_{cell}) (L/cell)	$2.1x10^{-12}$	-	[89]
Glucose Sensor Radius (a) (cm)	0.07	-	[58]
Sensor Surface Area (A) (cm^2)	0.0058	-	[58]

The porosity of the fibrin capsule was calculated by finding the percent weight difference between a newly made, fully hydrated fibrin gel and fully lyophilized sample. The value of 0.975 represents a mean of three samples. Such a high porosity is similar to the calculated porosity of a fibrin biofouling layer (ε=0.91) in Chapter 4.

5.3.6.1 Governing Equations

The governing equation describing glucose concentration in the gel layer (C_{gel}) is a non-linear, uni-dimensional diffusion-reaction equation in cylindrical coordinates through a porous medium. It has a diffusion term and a sink term to describe uptake by adherent cells (Eq. 21).

$$\frac{\partial C_{gel}(r,t)}{\partial t} = \frac{D_{gel}}{r}\frac{\partial}{\partial r}\left(r\frac{\partial C_{gel}(r,t)}{\partial r}\right) - Q_{gel}(r,t) \tag{21}$$

Q_{gel} is defined as the rate of glucose uptake by cells in the layer and is modeled by Michaelis-Menten kinetics, where $V_{max,gel}$ is the maximum rate of consumption (μmol/(cell-sec)), $K_{M,gel}$ is the Michaelis-Menten constant (μmol/ L), ε_{gel} is the porosity of the gel layer (unitless), and z_{cell} is the volume of a macrophage within the gel layer (L/cell) (Eq. 22). Michaelis-Menten formalism was chosen because the process of facilitative transport via the uptake of glucose through GLUT-1 and GLUT-3 transporters in RAW 264.7 macrophages fit this model well in previous literature studies [28, 70]. In this model, the fibrin network and cells were assumed to be well mixed within the gel layer. Therefore, they were not considered separately.

$$Q_{gel}(r,t) = \frac{V_{\max,gel} C_{gel}(r,t)}{K_{M,gel}\varepsilon_{gel} + C_{gel}(r,t)} \left(\frac{1-\varepsilon_{gel}}{z_{cell}} \right) \tag{22}$$

The governing equation for glucose concentration in the media (C_{media}) is a non-linear, uni-dimensional diffusion-reaction equation in cylindrical coordinates through a porous medium (Eq. 23). As there are no cells in the media layer, there are no consumptive terms in the equation.

$$\frac{\partial C_{media}(r,t)}{\partial t} = \frac{D_{media}}{r} \frac{\partial}{\partial r} \left(r \frac{\partial C_{media}(r,t)}{\partial r} \right) \tag{23}$$

5.3.6.2 Initial and Boundary Conditions

For the initial condition, it was assumed that the diffusion time in the gel layer was much shorter than the time scale of simulation. Therefore, the initial condition for the system was a uniform glucose concentration (C_o) multiplied by the porosity of the gel compartment when the sensor is inserted into the media at t = 0 sec, a plausible assumption as there was no other intrinsic source of glucose once an experiment began. The boundary condition at the sensor/layer interface was that the flux of glucose diffusion in the gel layer times the surface area (A) was equal to the rate of glucose uptake by the sensor, Q_{sensor}. At the interface of the gel layer and media regions, it was assumed that there was no consumption or accumulation of glucose, so the concentrations normalized by the porosities and fluxes were continuous across the interface. No flux boundary conditions were assigned to the outer boundary condition at the end of the media compartment because glucose could not move into or out of the

boundary at the edge of the beaker, creating an insulating boundary and making the flux at the outer boundary equal to zero.

5.3.6.3 Utilizing Computational Modeling for Nonlinear Curve Fitting of Experimental Data

The goal of this computational model is to determine the glucose uptake parameters necessary to recreate experimental findings of sensor decline in the presence of cell-embedded gels. Q_{gel} is the only component with consumptive terms in the model and within that term, both the porosity of the gel and volume of a cell are assumed to be fixed in the experiment. Therefore, changes in the output of the model were dependent on only two terms, $V_{max,gel}$, the maximum rate of consumption of the cells within the gel (μmol/(cell-sec)) and $K_{M,gel}$,the Michaelis-Menten constant for the cells within the gel (μmol/ L). The computational model described above was thus automated to run using every possible combination of 20 different values of $V_{max,gel}$ and 20 different values of $K_{M,gel}$, all of which centered around reported values of V_{max} (4.88×10^{-11} μmol/(cell-sec), noted as $V_{max,o}$) and K_M (6.13×10^3 μM, noted as $K_{M,o}$) for RAW 264.7 macrophages at 37°C [28]. The output from each run of the model was the trace of the normalized glucose current as a function of time at the sensor surface, giving 400 different traces to be analyzed for a goodness of fit. Simulations were run for a timescale of 5 hours and compared to the first five hours of the experimental data. This modification was made because the computational model assumes that macrophages will continue to consume glucose as an endless sink. In reality though, analyte consumption will reach a maximal

level within the cell. It was assumed that during the first five hours that cells in the experiment would consume glucose before reaching a level of internal saturation. As the sensor was presupposed in this model to be perfectly efficient, the trace at the sensor surface was assumed to be the amount of glucose converted into current by the sensor.

Each of the 400 modeled declines in normalized sensor current was then compared to the experimental traces of sensor decline in the following three cases: (1) presence of an unstimulated macrophage-embedded gel, (2) presence of an LPS-stimulated macrophage-embedded gel, and (3) presence of a PMA-stimulated macrophage-embedded gel. The genistein case was not considered as it was meant to serve only as a negative control that demonstrated how the decline in signal was metabolically regulated. To determine the best modeled fits of the experimental data, coefficients of determination (R^2) were calculated to find the best fit for the three experimental conditions as one minus the residual sum of squares divided by the total sum of squares. Comparison of R^2 values was chosen for analysis at this metric quantifies how well a model describes the experimental data. Figure 19 outlines the flowchart to determine the best modeled fit of the experimental data.

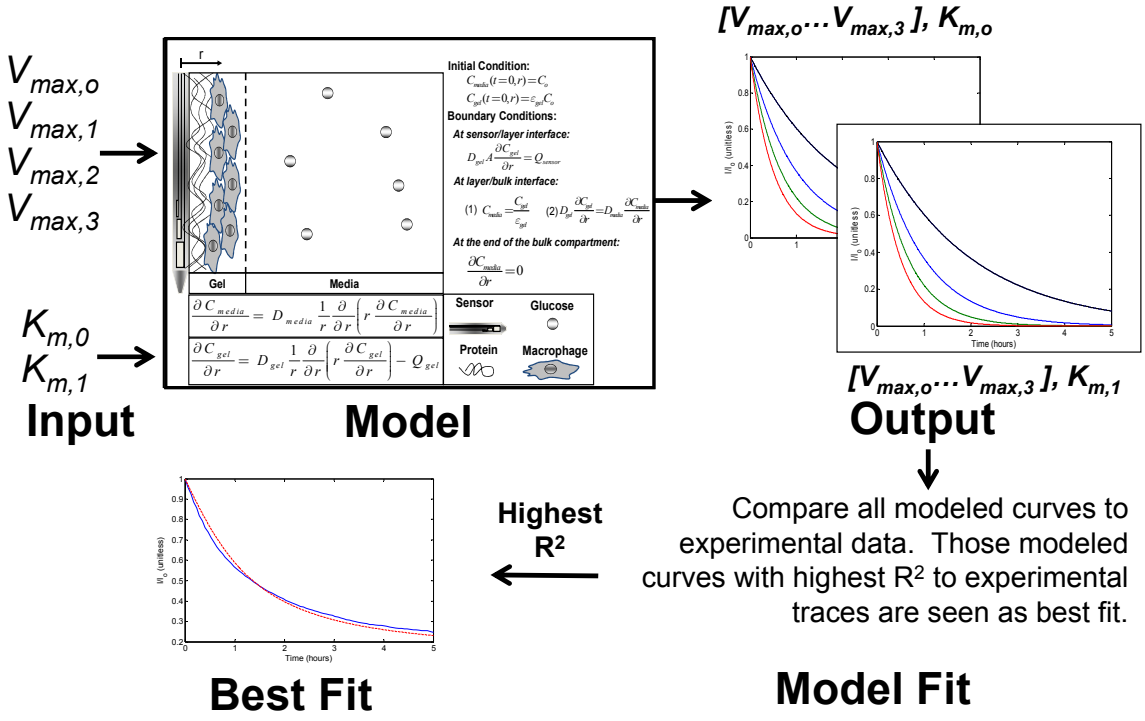

Figure 19: Computational flowchart to determine which glucose uptake parameters($V_{max,gel}$ and $K_{M,gel}$) best fit the experimental data when put into the model in this section. The above figure is generalized for four inputs of V_{max} and two of K_M.

5.3.7 Fluorescent Imaging of Glucose Uptake

To complement the data detailing the effect of cellular presence on sensor readings, fluorescent images of cellular glucose uptake were taken for each of the macrophage activation cases described above. The fluorescent glucose analog, 2-[N-(7-nitrobenz-2-oxa-1,3-diazol-4-yl) amino]-2-deoxy-D-glucose (2-NBDG) (Life Technologies, Eugene, OR), was used as the fluorescent tracer to image the uptake of the analyte. Unstimulated, LPS-stimulated (1 μg/mL for 24 hours), PMA-stimulated (50nM for 72 hours) and genistein-stimulated (100 μM for 24 hours) RAW 264.7 macrophages were seeded in different wells of a 24 well plate at a concentration of 10^5 cells/well in 1

mL low glucose DMEM (100 mg/dL) supplemented with 10% (v/v) fetal bovine serum (Sigma-Aldrich, St. Louis, MO), penicillin (50 U/mL) and streptomycin (100 μg/mL).

After 24 hours in the wells, the cell culture media in each well was aspirated and replaced with fresh low glucose DMEM supplemented with 100 μM 2-NBDG. This value has been previously reported as the optimal concentration for imaging of the tracer [90-92]. The 2-NBDG treated cells were then incubated for 30 minutes at 37°C. After incubation, the 2-NBDG-supplemented media was aspirated and each well was washed three times with sterile PBS to remove any potential background fluorescence in imaging. Fluorescent images were captured with a Nikon TE2000U microscope and NIS Elements software (Nikon) at a fixed exposure time to allow for qualitative comparisons across treatments. Images were post-processed in ImageJ.

5.4 Results

5.4.1 Assessing Cellular Viability and Distribution within the Gel Construct

To ensure cellular viability during both the fabrication of the gel as well as the experiments with glucose sensors, live/dead staining was performed in both cases. Figure 20 shows representative images of each case for an LPS-stimulated gel.

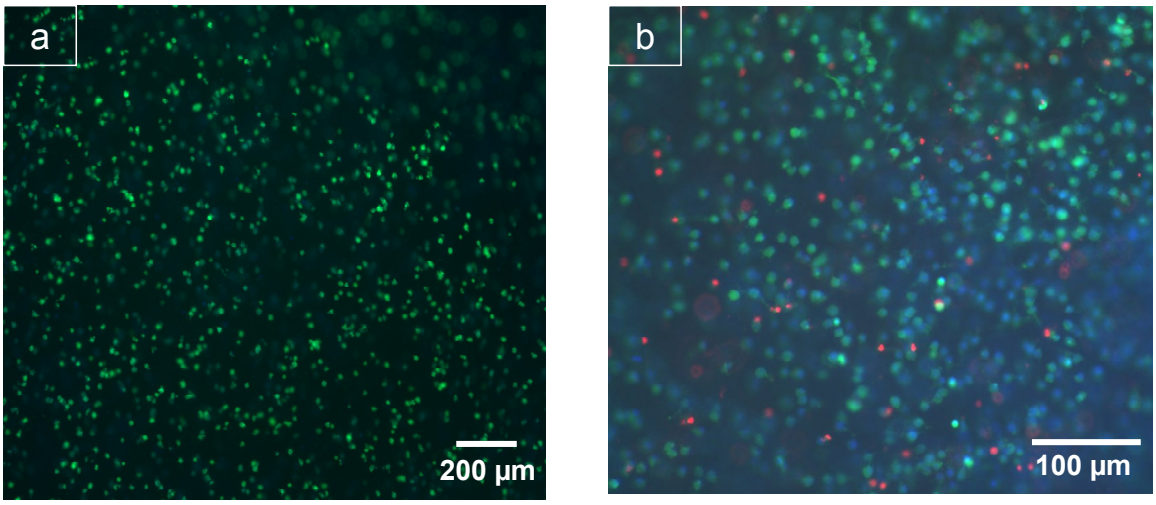

Figure 20: (a) Live/Dead assay of a cell-embedded fibrin gel 24 hours after fabrication (4x). (b) Live/Dead assay of a cell-embedded fibrin gel immediately following a 24 hour experiment when surrounding a glucose sensor (10x). Live cells are stained green, dead cells are stained red and all nuclei are stained blue.

From the staining in Figure 20a, it can be seen that process of fabricating these cell-embedded gels did not affect viability. Similarly, following 24 hour experiments, viability remained high, with few dead cells present in the image (Figure 20b).

Beyond the issue of viability, distribution of the cells within the gel was also of importance. A desirable gel should have a uniform distribution of cells throughout the gel so as to ensure that an equal amount of cells were present along the length of the sensor. This consideration ensures a uniform barrier to analyte transport to the sensor, negating any spatial heterogeneities in glucose consumption. Figure 21 shows an image of the distribution of live cells on the surface of a cell-embedded fibrin gel.

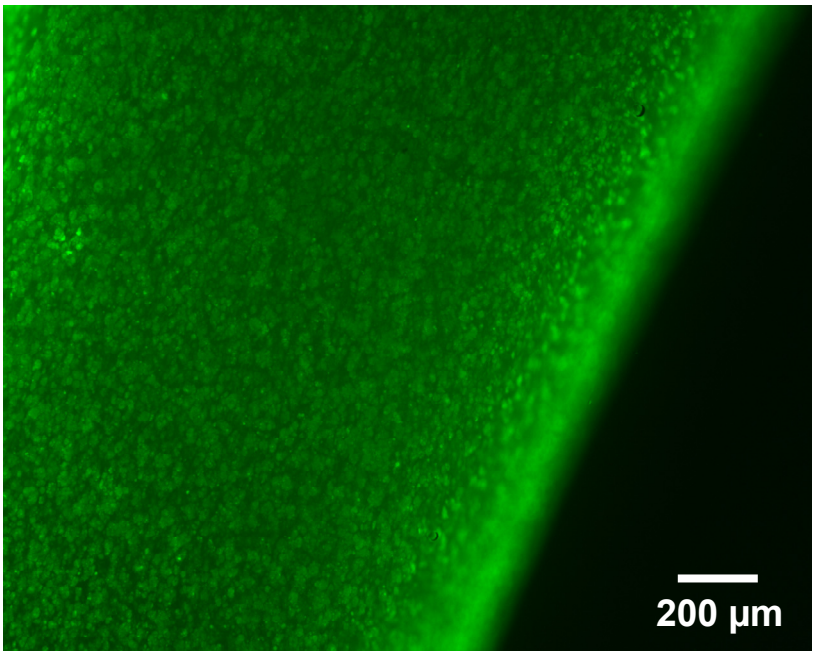

Figure 21: Live cell Calcein AM of distribution of cells on the surface of a cell-embedded fibrin gel (4x).

From the image above, it appears that cells are uniformly distributed throughout the gel, ensuring a uniform barrier to glucose transport along the length of the glucose sensor.

5.4.2 Assessing Sensor Performance in the Presence of Cell-Embedded Fibrin Gels

Glucose sensor response was assessed in the presence of four different treatments: (1) treatment with a macrophage-embedded gel with a cell concentration of $2x10^6$ cells/mL, (2) treatment with a fibroblast-embedded gel with a cell concentration of $2x10^6$ cells/mL, (3) treatment with an acellular gel or (4) treatment with no gel on the sensor surface (Figure 22). The data are presented as the mean of currents reported by the sensor divided by the steady state equilibration value of each sensor before

application of the gel on the sensor surface. Data were normalized for each run of the experiment to the respective baseline value because output currents of Medtronic Minimed sensors were not consistent from sensor to sensor in solutions with the same glucose concentration. This normalization therefore controlled for sensor-to-sensor variability and allowed for multiple traces to be plotted on one graph. For the ease of presentation, only the traces that were not statistically significant ($p<0.05$) from one another are labeled. Otherwise, it should be assumed that different treatments had statistically significant effects on sensor response.

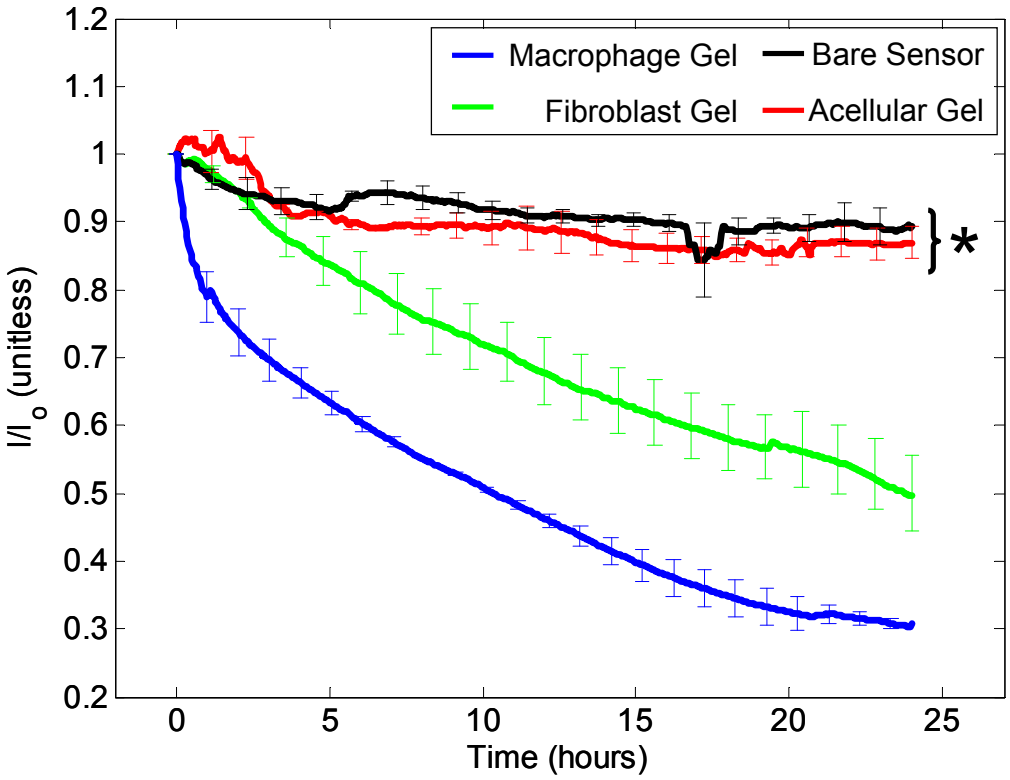

Figure 22: The effect of the presence of cell-embedded fibrin gels on glucose sensor performance. Data represented as mean normalized glucose sensor currents (n=3) ± standard deviation. * represents treatments that were not statistically significantly different from one another ($p<0.05$).

As expected, the bare sensor maintained its baseline signal during the treatment phase. Its reading in low glucose media never deviated to less than 90% of the baseline value. The small decrease in signal that did occur over that time could be attributable to consumption of glucose by the sensor itself. Sensor signals in the acellular gel case mimicked those of the bare sensor readings, indicating that the gel itself posed no barrier to glucose transport to the sensor surface. Both cellular gel traces (fibroblast and macrophage) were significantly different than the acellular gel and bare sensor cases,

elucidating the effect of cellular presence on sensor signal. Moreover, cell type was shown to have an effect on sensor signal, as the macrophage gel signal decreased more rapidly than the fibroblast signal.

5.4.3 Assessing the Effect of Macrophage Stimulation on Sensor Performance

Once the presence of cells was shown to contribute to sensor decline, the gel construct was modified to incorporate macrophages activated with both LPS and PMA, as their phenotypes more resemble those of macrophages during the *in vivo* inflammatory response to implantation. The effect of macrophage activation on sensor signal is shown in Figure 23.

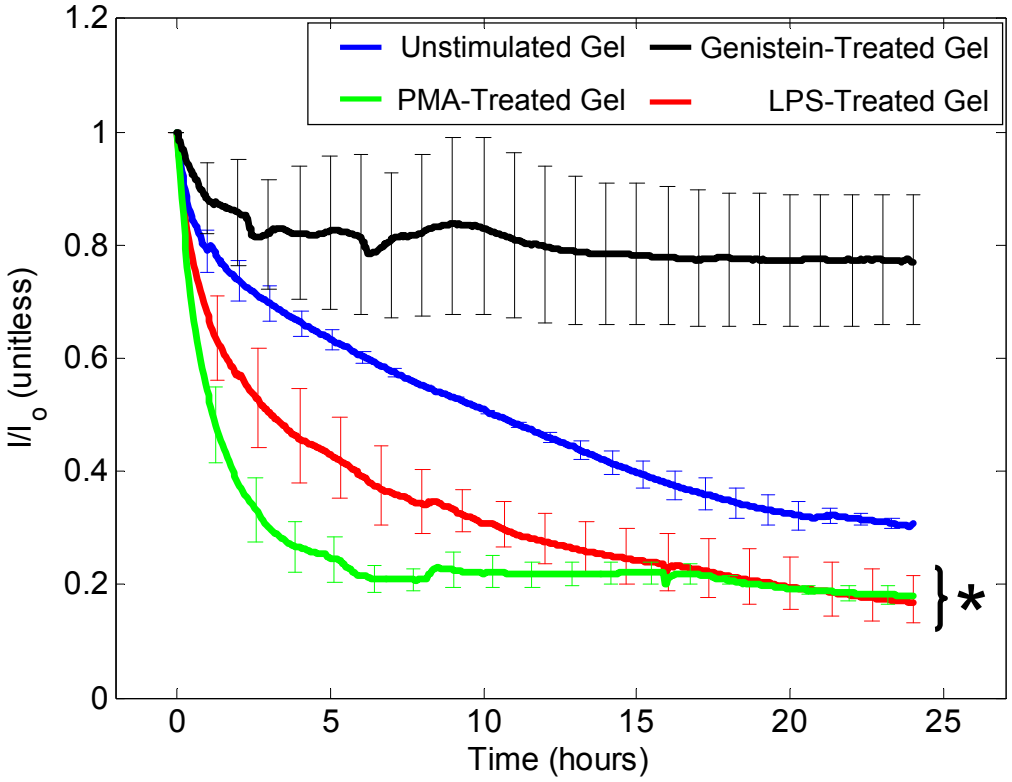

Figure 23: The effect of the presence of macrophage stimulation on glucose sensor performance. Data represented as mean normalized glucose sensor currents (n=3) ± standard deviation. * represents treatments that were not statistically significantly different from one another ($p<0.05$).

While the activation cases (PMA and LPS-stimulated gels) were not significant from one another, each was statistically different from the unstimulated macrophage case. The unstimulated, LPS-stimulated and PMA-stimulated gels were all statistically significant from the genistein-treated gel, which served as the negative treatment control for this experiment.

5.4.4 Comparison of Sensor Responses for Fibrin Gel System and Whole Blood System

In order to determine if the signal decreases seen in Figures 22 and 23 were physiologically relevant, they were compared to *ex vivo* sensor declines previously published by the author and collaborators [75]. Figure 24 compares sensor signals from both an unstimulated macrophage embedded gel and an LPS-stimulated macrophage embedded gel to signal declines in whole blood.

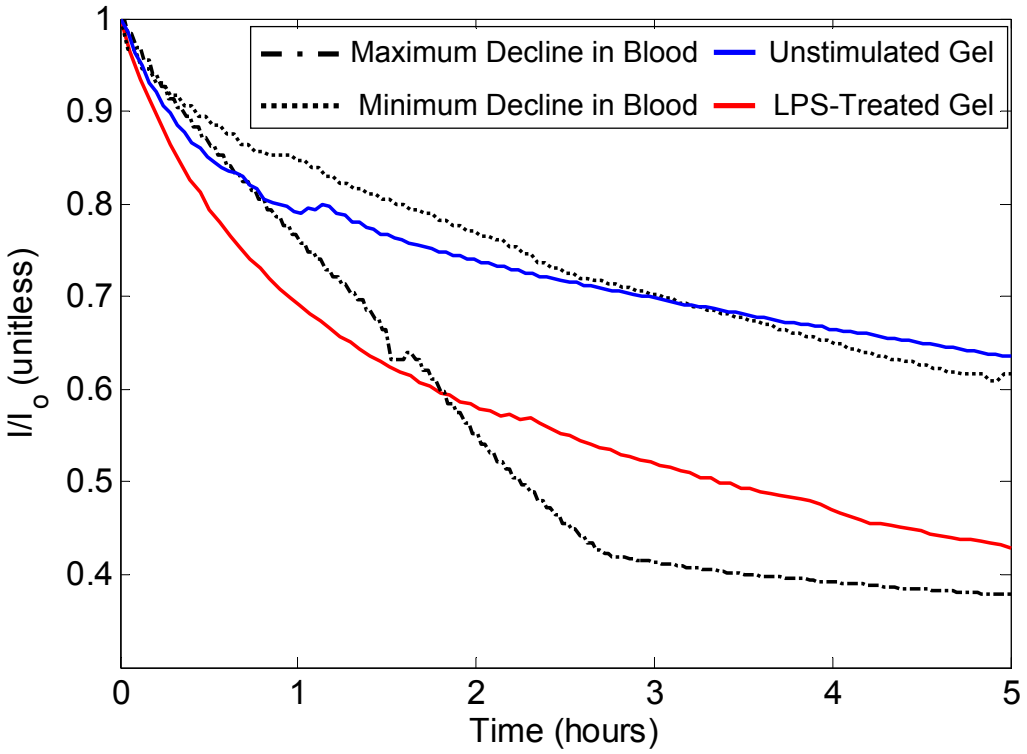

Figure 24: Comparison of sensor declines in whole blood to declines in the presence of macrophage-embedded fibrin gels.

Both the unstimulated and LPS-stimulated declines lie within the envelope of maximal and minimal sensor declines in whole blood. While these comparisons are

made through five hours and not the 24 hours displayed in the above figures, these whole blood data are still instructive to show that the declines in the fibrin gel case are comparable to those in the whole blood *ex vivo* case.

5.4.5 Validation of Fibrin Gel Results through Computational Modeling

To validate the experimental results presented above, a computational model was run to find the metabolic parameters necessary to produce such declines. Figure 25 presents each experimental case as well as its corresponding line of best fit for the unstimulated, LPS-stimulated and PMA-stimulated macrophage cases shown in Figure 23.

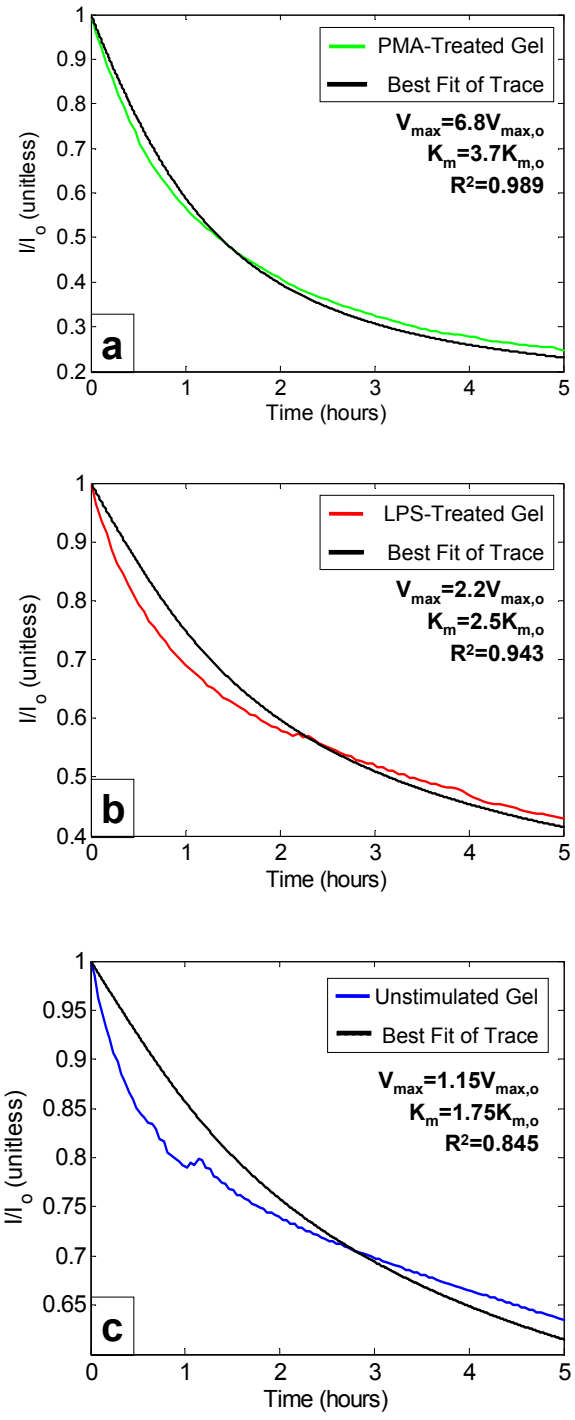

Figure 25: The computational best fit for cases where (a) a PMA-stimulated macrophage gel, (b) an LPS-stimulated macrophage gel and (c) an unstimulated macrophage gel surrounded a sensor.

Overall, modeled outcomes were found to be far more sensitive to changes in V_{max} than changes in K_M. The metabolic parameters of V_{max} and K_M necessary to produce the best fit for the unstimulated macrophage trace were within 15% and 75%, respectively, of the values reported by Ahmed, et al. for RAW 264.7 macrophages [28]. This proximity to literature values shows that the metabolic behavior of macrophages within the 3D gel construct is similar to their behavior in 2D monolayer. Additionally, the best fits of stimulated macrophages produced expected trends where the V_{max} values of LPS-stimulated ($2.2V_{max,o}$) and PMA-stimulated ($6.8V_{max,o}$) macrophage cases were elevated in comparison to the unstimulated case, which is in accord with physiological findings detailing the increased capacity for glucose found in activated macrophages [28, 70].

5.4.6 Fluorescent Imaging of Glucose Uptake

To visualize the differences in glucose consumption between the different cases of stimulation, each case of macrophage stimulation was dosed with the metabolizable glucose analog, 2-NBDG at 100 μM, and imaged 30 minutes after administration. All images were captured at the optimal exposure time for the PMA-treated cells, as those had the brightest overall signal, to allow for qualitative comparison across treatments. Qualitatively, the intensity of the intracellular glucose signal in each case correlates well with the glucose consumption observed in Figure 23. As would be predicted from the sensor signal traces immediately after treatment, both PMA-treated and LPS-treated

cells had brighter fluorescent signals than the unstimulated macrophage case, with the PMA-trace showing the brightest overall signal. Genistein-stimulated macrophages did not have much of a signal, showing that the negative control treatment worked in limiting cellular glucose uptake.

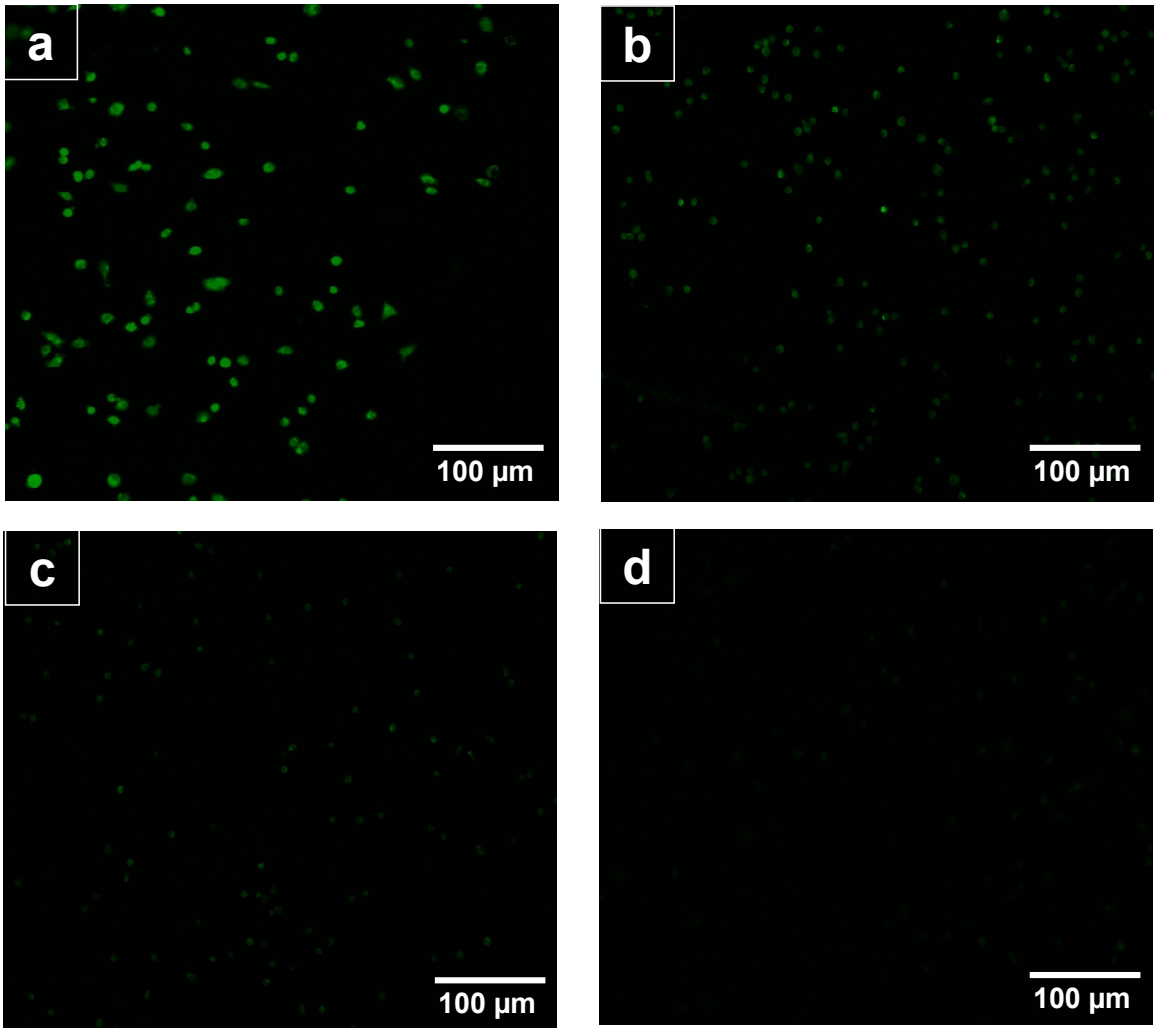

Figure 26: Fluorescent images of 100 µM 2-NBDG uptake 30 minutes after administration for (a) PMA-stimulated macrophages, (b) LPS-stimulated macrophages, (c) unstimulated macrophages and (d) genistein-stimulated macrophages.

5.5 Discussion

From a clinical perspective, the current utility of implantable glucose sensors for management of diabetes has been extremely limited due to their abbreviated useful lives *in vivo.* Indeed, the three to seven day window for which these devices are approved by the FDA only allows for continuous glucose monitoring as a feasible diabetes management strategy for those who require the most diligent of glucose observation. Functionally speaking, sensor behavior during this period would best be considered as anomalous and erratic, further limiting sensor efficacy even during the FDA-approved time window.

Beyond being a time scale for clinical approval, the three to seven day time window coincides with a period of highly pronounced implant-associated inflammation to the newly installed sensor, punctuated by the infiltration and interrogation of the sensor surface by inflammatory neutrophils and macrophages [14]. A growing amount of evidence in recent literature has pointed to the consumptive capacity of these inflammatory cells as a potential barrier to short term sensor accuracy [75-78]. To further investigate the causal link between inflammatory tissue reaction and sensor function, an *in vitro* biomimetic surrogate for the provisional matrix of proteins and inflammatory cells was fabricated.

The design specifications for this biomimetic surrogate were chosen to maximize its physiological relevance in recapitulating early stage tissue response to an implanted

sensor. First, this construct was composed of a fibrin gel. The formation of a fibrin network immediately surrounding the sensor is one of the major products of the coagulation cascade that is triggered upon insertion of the sensor into tissue and is a hallmark of the inflammatory response to sensor implantation [93-97]. Secondly, the gel constructs were embedded with an inflammatory cell type at a physiologically relevant density to recreate the inflammatory cell presence around the sensor. The RAW 264.7 murine macrophage was chosen as the candidate inflammatory cell type for the gel constructs as it is a ubiquitous cell type for biocompatibility and inflammatory studies in the literature and it responds appropriately to inflammatory activation [98-102]. The density of cells within the gel was based upon *in vivo* histology data of macrophage infiltration into areas of inflammation and was also within the range of 10^5 to 10^7 cells/mL used by Klueh, et al. for macrophage studies [77, 83]. Lastly, this construct has been shown to not negatively impact cell viability or functionality across a wide range of cell types.

Yet, as this construct has yet to be employed for embedding macrophages, cell viability had to be assessed before using the gels in an experiment with glucose sensors. Figure 20 shows fluorescent live/dead staining for macrophages embedded in a fibrin gel. Both following the fabrication of the gel and the completion of an experiment using the gel, viability remained high. Additionally, the cells within the gel maintained a uniform distribution through the gel, as evidenced by the image in Figure 21. This

consideration ensured that there would be an even barrier and resistance to analyte transport along the length of the active sensing region of the sensor. Such an even layer of inflammatory cells on the surface aligns well with *in vivo* histology images where a sensor is interrogated along its whole surface by macrophages [17].

As a first proof of concept that cell-embedded gels would decrease sensor response when surrounding a sensor, glucose sensors were tested in four different cases (Figure 22): (1) treatment with a macrophage-embedded gel with a cell concentration of $2x10^6$ cells/mL, (2) treatment with a fibroblast-embedded gel with a cell concentration of $2x10^6$ cells/mL, (3) treatment with an acellular gel or (4) treatment with no gel on the sensor surface. Fibroblasts served as the negative cellular control to ensure that any declines in sensor signal were not just in response to a bulk presence of cells, but instead were specific for cell type. The bare sensor case served as a control to examine if consumption of glucose by the sensor itself was a contributing factor to signal decrease. The acellular gel treatment served to examine if the gel itself was serving as a diffusion barrier to glucose transport to the sensor surface. Since there were no cells in these gels, the protocol was modified such that 480 μL of cell media was added to the gel formulation instead of a cellular solution of media.

Though the signal did decrease over the period of 24 hours in the bare sensor case, the signal never dropped below 90% of its pre-treatment baseline output signal. This effect could be due to consumption of the analyte by the sensor itself and is

negligible in comparison to the drops observed by sensors surrounded by cell-embedded gels. When inserted into acellular gels, sensors maintained signals that were redolent of a bare sensor in media. Indeed, the acellular gel case and the bare sensor case were not statistically significant from one another ($p<0.05$), making it the only case comparison in Figure 22 that was not statistically significantly different. From these data, it can be concluded that the gel itself does not provide any diffusive barrier to glucose transport to the sensor. This finding is not surprising given that greater than 97% of the gel is void space, which is comparable to the 91% void space calculated for a fibrin biofouling layer in Chapter 4. Additionally, the results of this case show that the gel does not have a deleterious impact on the enzyme activity of the sensor.

The presence of cell-embedded gels did have an impact on sensor signal in both the fibroblast and macrophage-embedded cases in Figure 22, causing declines to 50% and 30% of their respective original signals. Both cases were statistically significantly different from the bare sensor and acellular cases. Beyond the presence of cells, the presence of cell type also affected the sensor signal, as the macrophage-embedded gel case produced a significantly lower signal over the length of the experiment than the fibroblast-embedded case. This result was expected as pre-adipocyte fibroblasts do have a lower reported V_{max} (1.67×10^{-12} μmol/(cell-sec)) than macrophages (4.88×10^{-11} μmol/(cell-sec)) on a per-cell basis at 37°C, thereby providing a useful verification that the gel construct would also be sensitive to changes in cell type [28, 49, 103].

After the initial verification that cells could reliably maintain viability and produce a drop in signal that is sensitive to cell type, a more extensive study was conducted using activated macrophages. Four gel cases were employed in this study: (1) treatment with gels embedded with LPS-stimulated macrophages, (2) treatment with gels embedded with PMA-stimulated macrophages, (3) treatment with gels embedded with unstimulated macrophages and (4) treatment with gels embedded with geinstein-stimulated macrophages (Figure 23). The purposes of this study were twofold. First, these treatments served as verification that the observed decrease in signal was metabolically regulated instead of a case where the presence of cells in the void space of the sensor retarded glucose diffusion to the sensor via steric exclusion. Secondly, activated macrophages present a more physiologically correct model for macrophage phenotype and behavior within the site of implantation. Therefore, to provide a more complete *in vitro* model of sensor behavior, the effect of cell activation had to be considered.

As the negative control treatment, the genistein-treated case produced modest declines in signal, dropping only ~20% for the length of the experiment. This result is expected as genistein has been shown to be a competitive inhibitor of glucose uptake, decreasing the efficacy of two predominant facilitative glucose transporters, GLUT-1 and GLUT-3 to extracellular glucose across cell types [28, 104, 105]. Additionally, this

case displays that uptake of the analyte is mediated through facilitative diffusion and not passive diffusion through the cell membrane.

Macrophage activation through both LPS and PMA stimulation was shown to have an effect on sensor signal relative to both the unstimulated macrophage case and the genistein-stimulated macrophage case. However, the stimulated cases did not differ significantly from one another. Given the considerable metabolic demands that activated macrophages face during the foreign body response in the way of attempted phagocytosis, respiratory burst, cytokine production and cellular recruitment, it is plausible that these treatments would increase the uptake of glucose. Treatment with each activator has been shown to increase cell surface transporter affinities for extracellular glucose in macrophages, effectively raising the maximal rate of glucose uptake [36, 42, 43].

Qualitatively, the trends seen in Figure 23 can be confirmed with the images in Figure 26, which presents uptake of a fluorescent analog of glucose, 2-NBDG, in each of the four cases detailed above. 2-NBDG served as an ideal analog for glucose as its uptake has been shown to be facilitated through the same major transporters as glucose, thus providing an accurate basis for comparison [91]. As it is decomposed into a non-fluorescent constituent, the optimal staining time is a dynamic equilibrium between uptake and decomposition. For this cell type, the optimal staining time was determined to be 30 minutes for a 2-NBDG dose of 100 μM. The short time of incubation also

avoided the possibility of the fluorescent signal quenching with increased exposure to the tracer. At this time, the effects of activation on uptake are clear, as the intensities in both the LPS and PMA-stimulated cases are brighter than the unstimulated and genistein-stimulated traces just by inspection. The PMA-stimulated traces are brightest on a per-cell basis, which is consistent with the trends seen in the first 30 minutes of Figure 23. Predictably, the fluorescent signals in the genistein-stimulated case are faint and barely perceptible over the background, which is expected given that genistein is known to decrease GLUT transporter affinity to the analyte.

To add context to the results of the *in vitro* cell-embedded gel design, the unstimulated and LPS-stimulated macrophage cases were compared to the maximal and minimal *ex vivo* results for sensor decline presented in Chapter 4 (Figure 24). As the figure shows, both traces lie within the envelope outlined by the maximal and minimal *ex vivo* declines, demonstrating that the effects seen with the *in vitro* gel system are adequate representations of what would occur in a more realistic, clinical setting. Moreover, the magnitudes of decline seen in these cases are very similar to those reported in both *in vitro* and *in vivo* studies by Klueh, et al. for comparable (~24 hour) time frames [77]. In their *in vitro* studies, the group witnessed sensor declines to between approximately 20% and 35% of the pre-treatment signals over 24 hours. Similarly during *in vivo* studies where 2.5×10^6 macrophages were injected at the site of implantation in a mouse, signals declined in the same fashion over the period of 24

hours. Favorable comparisons between the results of Figure 24 and previously published reports of sensor decline in the presence of inflammatory cells demonstrate the utility that this construct could have as an *in vitro* screening tool for sensor biocompatibility.

As an additional validation of the fibrin gel design, a computational model of the experimental setup was designed and implemented to quantify the metabolic parameters necessary to produce the experimental declines seen in Figure 23. The major consideration in performing such a validation was due to the behavior of the cells once cultured in a 3D environment. Metabolic characteristics for macrophages, even RAW 264.7 macrophages in particular, are well characterized for a number of different conditions, including variations in temperature and treatment type [36, 42-44]. However, all of these studies have been based on macrophages cultured in a 2D monolayer on a substrate like tissue culture polystyrene that has been optimized for cell culture. When cell culture is moved from a 2D monolayer to a 3D construct like the fibrin gel presented above, a number of complex factors, from the physical forces on the cells themselves to the interaction between the cells and the surrounding microenvironment can alter cell phenotype and potentially negatively impact their functional capabilities relative to a 2D monolayer [106, 107]. Therefore, this model was implemented both to test whether the V_{max} and K_M values necessary to recreate the results from Figure 23 were reasonable relative to published literature values and to

determine whether changes in trends across treatments aligned with previously reported results.

Best fits were determined through a screening process where modeled results were compared to experimental traces through comparison of R^2 values. The best fits described the variations in the observed experimental data well, with R^2 values ranging from 0.845 in the unstimulated macrophage case to 0.989 in the PMA-stimulated macrophage case. The best fit for unstimulated macrophage case was found to have a V_{max} of $1.15V_{max,o}$ and a K_M of $1.75K_{M,o}$. These results agree well with the benchmark values of each reported by Ahmed, et al. and demonstrate that encapsulation within the 3D fibrin gel substrate does not adversely affect cell function with respect to glucose uptake [28].

Likewise, best fits of traces from activation of macrophages with LPS and PMA resulted in increased consumptive parameters in each case. The best fit of the PMA-stimulated macrophage case had a V_{max} of $6.8V_{max,o}$ and a K_M of $3.7K_{M,o}$. While there is not a direct comparison of fold increase in V_{max} and K_M from PMA-stimulated RAW 264.7 macrophages, Kiyotaki, et al. reported a two-fold increase in the V_{max} of J774 murine macrophages after only 3 minutes of PMA incubation at a concentration of 6 μg/mL when compared to unstimulated macrophages [35]. Ahmed, et al. reported a 4 fold increase in glucose transporter affinity to glucose when RAW 264.7 macrophages were cultured with PMA for 30 minutes [28]. The best fit of the LPS-stimulated

macrophage case had a V_{max} of $2.2V_{max,o}$ and a K_M of $2.5K_{M,o}$. These results agree well with the findings of both Gamelli, et al. and Fukuzumi, et al., who observed two to three-fold increases in maximal glucose consumption rate in macrophages stimulated with LPS [42, 43]. Overall, the increases in V_{max} calculated from the stimulated cases make sense from a physical perspective. With an increased demand for the analyte during inflammatory stimulation, cells would be expected to increase their rate of consumption to meet such metabolic demands. While it should be noted that the model was more sensitive to changes in V_{max} than K_M, it was nonetheless surprising that stimulation was met with increases in K_M. Increases in K_M suggest that the transporters are becoming less effective in their analyte uptake. For cases of inflammatory stimulation, one would think that K_M would decrease, as that is representative of an increase in transporter affinity to the analyte. Despite these decreases in the affinity with which the cells are taking up the analyte, their rate of maximal consumption on a per-cell basis is increased, which over time will translate to higher consumption in the provisional matrix. Taken in concert, these stimulated case model fits further demonstrate the utility of the fibrin gel construct by showing that stimulated cells in a 3D environment have similar increased glucose uptake profiles to stimulated cells in a 2D environment.

5.6 Conclusions

In this study, a biomimetic surrogate of early stage tissue reaction to implantation was fabricated and used as a tool to assess glucose sensor performance in the presence of pro-inflammatory macrophages proximal to the sensor surface. When inserted into macrophage-embedded fibrin gels, sensors produced declines over 24 hours that were comparable to previous *ex vivo* and *in vivo* studies with glucose uptake parameters that were similar to those reported in the literature. Additionally, the versatility of the design was demonstrated as gel constructs were shown to be responsive to cellular stimulation, as sensors inserted into both LPS and PMA-stimulated macrophage gels produced significant drops in signal relative to the unstimulated macrophage case. As the causal link between tissue reaction and sensor function continues to be clarified, this *in vitro* fibrin gel system presents an exciting and promising platform for assessing early stage sensor function without the need for immediate *in vivo* studies.

.

Chapter 6. Dissertation Overview and Future Directions

6.1 Dissertation Overview

The global hypothesis motivating this research is that implant-associated tissue reactions negatively impact *in vivo* glucose sensor performance. As the nature and extent of tissue reaction to sensor implantation changes over time, this research tackled the global issue of tissue reaction by examining two distinct temporal regimes of the overall process. The first regime examined late stage (weeks to months) interactions of a sensor with fully formed capsular tissue and served as the focus of Chapter 3. The second regime examined the ways in which early stage (days to weeks) acute inflammatory tissue reaction to sensor implantation could negatively impact sensor response, and served as the focus of Chapter 4. Building upon these results, the information in Chapter 5 presented a novel *in vitro* platform for recreating such acute inflammatory tissue around a sensor as a potential screening method for biocompatibility of future sensor designs.

With respect to late stage interaction, if a sensor signal is able to persist for weeks after implantation, its performance will be characterized by both high attenuation of the signal as well as a long lag time relative peak blood glucose readings. However, it is unknown which aspects of the foreign body capsule have the most pronounced effects in causing both signal attenuation and signal lag. Due to the well-characterized constituents, geometry and orientation of fully formed capsular tissue, a computational

model of glucose transport out of the capillaries, and through both the interstitial space in the subcutaneous tissue and fully formed capsular tissue to a functioning sensor was constructed. This model of glucose transport was able to recreate *in vivo* results for lag and attenuation with physiologically accurate parameters taken from literature. Using logarithmic sensitivity analysis, the sensitivities of signal attenuation and lag to five different parameters, (1) capsule diffusion coefficient, (2) capsule porosity, (3) vessel density, (4) maximal cellular glucose consumption rate in the capsule, and (5) capsule thickness, were calculated. Sensor signal lag was most sensitive to capsule thickness, demonstrating that lag is determined not by the contributions of the inner constituents of the capsule but by the macro length scale of the dense, avascular collagen capsule. Sensor signal attenuation was most sensitive to subcutaneous vessel density and capsule porosity proximal to the sensor. This finding was expected since vessels are the only source of glucose in the system. As a result, a decrease in the amount of glucose present will produce a concomitant decrease in the glucose to be measured relative to blood glucose values. Additionally, as the capsule becomes less porous, there are fewer pathways for glucose to traverse to get to the sensor, resulting in an accumulation of glucose within the foreign body capsule. Moreover, when the variations in parameters were analyzed to examine what aspects will produce an ideal situation of low signal lag and low signal attenuation, subcutaneous vessel density was identified as being the largest determinant for such a scenario.

Early stage sensor response to implantation is generally marked by erratic and anomalous signals that frequently drop quickly and obscure accurate glucose readings in the first days and weeks following implantation. As compared to late stage tissue reactions composed of a dense, avascular capsule, early stage tissue reactions are mediated by two processes: blood borne protein adsorption and inflammatory cell adhesion on the sensor surface. The goal of Chapter 4 was to elucidate the effects of these two processes on sensor response using an *ex vivo* whole blood system.

When incubated in whole blood, sensors reported a marked decrease in signal. However, when incubated in platelet poor plasma, the fraction of blood containing only protein and small molecules, the sensor signal maintained a steady state despite the adsorption of proteins onto the sensor surface. The platelet poor plasma trace, coupled with modeled results of glucose traveling through an acellular protein mat, demonstrate that protein adsorption is not the culprit in the anomalous and erratic sensor behavior seen immediately following implantation. As the only difference between whole blood and platelet poor plasma is the presence of cells, it could be assumed that cells within the blood were behaving as a glucose sink and consuming the analyte before it could reach the sensor. Moreover, computational models comparing the transport of glucose from a bulk blood phase through the provisional matrix of cells and protein found that the observed *ex vivo* decreases were a result of glucose consumption by inflammatory macrophages, not erythrocytes. Models also demonstrated how glucose consumption

by macrophages can induce a "depletion zone" of glucose with respect to distance from the sensor. As a result, otherwise functioning sensors are not able to sample more representative traces of interstitial glucose.

Buoyed by the work of Chapter 4 as well as the subsequent findings of Klueh, et al., Chapter 5 focused upon the design and validation of a novel construct that can mimic the *in vivo* 3D cellular setting around the sensor for the focused *in vitro* investigation of early stage effects of implantation [76-78]. The design was comprised of a physiologically relevant 3D fibrin gel substrate embedded with a RAW 264.7 murine macrophage cell line. The substrate itself was found to promote viability and function of the embedded cells while having no deleterious impact on sensor signal. Declines in sensor signal for sensors treated with macrophage-embedded gels fell within the range of those seen in the *ex vivo* studies of Chapter 4.

In total, it may be concluded from this dissertation that instead of sensors "failing" *in vivo*, as is often reported, that different physiological factors mediate long term sensor function by altering the environment around the implant. For times immediately following implantation, sensor signal is mediated by the presence of inflammatory macrophages adhered on the surface. When only proteins and these inflammatory cells are present on the surface of the sensor, the inflammatory cells consume interstitial glucose to meet the metabolic requirements of various innate immune defense mechanisms. However, at longer times post-implantation, sensor

signals are mediated not by the consumptive capacity of macrophages, but instead by the subcutaneous vessel density surrounding the sensor as well as the porosity and thickness of the foreign body capsule itself. A possible explanation of this transition away from cell consumption as time passes is that macrophages become more metabolically senescent within the capsule as it matures. Such a theory has been posed by Holt, et al. in *in vitro* studies [108].

As techniques for improving glucose sensing improve, so too must the biocompatibility of these devices in order to make implantable glucose sensors a viable option for diabetes management. By outlining the major processes that negatively impact short and long term sensor performance *in vivo*, this dissertation provides the basis for more rational, directed and biologically-motivated sensor designs to address and correct for these various modes of failure.

6.2 Future Studies

The conclusions reported in this dissertation provide direction for future research by examining the link between implant-associated tissue reactions and implantable sensor function. Using this work as a baseline, research into the specifics of innate immunity and macrophage biology as well as the consumption of oxygen, and not just glucose, by inflammatory cells will create a more complete profile for understanding implantable glucose sensor biocompatibility.

6.2.1 Investigating Oxygen Transport

As oxygen is a necessary input for glucose oxidase to produce a signal, a thorough examination of a depleted sensing environment should also include the interaction between tissue and oxygen proximal to the sensor. Inflammatory cells have elevated affinity for oxygen to facilitate anti-microbial defense mechanisms like respiratory burst. To further complicate matters, the tissue wounded from implantation is shown to have decreased oxygen tension relative to untreated tissue [32-34, 109]. Such an increased affinity for oxygen is exacerbated by the decreased amount of oxygen present in wounded tissue. Animal models have shown that 3-5 days post-injury, oxygen tension of the affected tissue dropped from 150 mmHg to 5-7 mmHg. It has been posited that such a drop could be due to the shunting of oxygen-providing blood to more patent vessels away from the injured tissue [110, 111]. Gough, et al. have demonstrated that oxygen permeability within tissue surrounding an implant decreases over time, with the steepest drop coming in the first week [110]. Additionally, the concentration of unbound oxygen in tissue is much lower than that of glucose, meaning that oxygen limits the glucose oxidase reaction in the body [112, 113]. This situation of both increased demand and limited supply of oxygen could negatively impact sensor function where the sensor cannot produce hydrogen peroxide despite the presence of glucose. In effect, the sensor would become more sensitive to oxygen than glucose.

Research from Gough, et al. has attempted to stem the potential negative impact of oxygen depletion by designing a different sensing regimen than that utilized by Medtronic [110-114]. A noticeable feature of the Medtronic sensing mechanism is that for every molecule of hydrogen peroxide produced, one oxygen molecule is consumed. In order to limit the consumption of oxygen, Gough et al. employed a two enzyme system [51]. Instead of reducing hydrogen peroxide like the Medtronic design, this design produces a glucose-dependent oxygen current from excess oxygen. This value can then be subtracted from a non-enzymatic oxygen reference electrode current to give a glucose dependent signal. Advantages of this design include (1) that half of the amount of oxygen is needed to produce a signal relative to the Medtronic design and (2) by producing a glucose current that is a relative measure to the ambient environment, the issue of decreased signal that is present in direct measurements may be avoided. As Medtronic's platform does not use this relative, oxygen based method for sensing glucose, it will be more susceptible to oxygen deficiencies.

However, despite different sensing platforms, previous research has only offered up suggestions as to how oxygen levels could affect sensor response. Hence, the focus of future studies should assess how oxygen levels, specifically hypoxic conditions, can alter sensor signals and well as the local environment. If depressed oxygen levels can create a decrease in sensor response, there could be a synergistic effect with glucose consumption that creates an environment ill suited for sensing.

6.2.2 Investigating Macrophage Plasticity as a Potential Therapeutic for Improved Biocompatibility

The hypoxic environment described previously around implants has been shown recently to induce expression of hypoxia inducible factor 1-alpha (HIF-1α) in macrophages. This transcription factor has been shown to upregulate cell proliferation, as well as encourage the production of pro-inflammatory cytokines and their receptors that drive the cell to the M1 phenotype [115-118]. The classic phagocytic activated macrophage, the M1 phenotype is elicited by cytokines including interferon-gamma (IFN-γ) and tumor necrosis factor (TNF) as well as by Gram-negative bacterial cell wall lipopolysaccharides (LPS). M1 macrophages generate large amounts of reactive oxygen species and inflammatory cytokines, which all serve to augment killing of phagocytosed intracellular parasites and local cell-mediated immune response (the Th1 response). While M1 macrophages are critical for the early response to injury and infection, prolonged or aberrant activation of M1 macrophages can also result in undesired tissue destruction and chronic inflammation [119].

The M2 macrophage phenotype describes macrophages in a broad category that encompasses macrophages activated in a manner different than the classic M1 macrophages, and includes macrophages activated by IL-4, IL-13, IL-10, immune complexes, and glucocorticoids [119-121]. M2 macrophages promote angiogenesis, tissue remodeling, parasite encapsulation, and can act as immunoregulators by suppressing the inflammatory response. While M2 macrophages can be activated via

different mechanisms, they are generally characterized by low levels of IL-12 and IL-23 secretion along with high levels of IL-10 secretion. M1 macrophages can be distinguished from M2 macrophages by the expression of distinct sets of chemokines and chemokine receptors [121]. It has been proposed that polarization of macrophages towards the M2 form can create an environment that is favorable towards wound healing, tissue regeneration and implantable biomaterial presence [122]. Consequently, the identification of pathways that can be modified to regulate macrophage polarization will be extremely beneficial for harnessing inflammation in pathologic states.

Stimulation of macrophages with the anti-inflammatory, pro-wound healing cytokine IL-10 has been shown to drive macrophages to the anti-inflammatory M2 phenotype. Within the realm of cancer biology, M2 phenotypes of tumor associated macrophages have been shown to not only be anti-inflammatory, but also pro-angiogenic, making them potential targets in cancer therapy [115, 123-125]. Using the information from the previous chapters and literature that both hypoxia and cellular consumption of analytes negatively impact the sensing region, treatments could be designed to hopefully reverse these effects. By adding therapeutic amounts of IL-10 to the *in vitro* model of sensor implantation in Chapter 5, one could show that macrophage phenotype can induce changes in sensor response. Furthermore, an environment rich in M2 macrophages could create a more advantageous sensing environment than an M1 environment through decreased ROS production and pro-inflammatory cytokine release

and increased release of pro-angiogenic factors. As vessel density proximal to the sensor has been previously shown to be paramount in the long term viability of implantable sensors in Chapter 3, the release of these factors could encourage vessel growth at an earlier stage and vascularize the foreign body capsule [13, 17, 58]. This information could provide a valuable amount of information on future therapeutic controlled release mechanisms for the extended useful lives of implantable glucose sensors.

6.2.3 Incorporation of Perfusion into the Fibrin Gel Model

Though the gel construct designed in Chapter 5 presents an exciting new *in vitro* biomimetic surrogate for the provisional matrix surrounding an implanted sensor, it could be modified and improved to become more physiologically relevant. For example, the construct in Chapter 5 sat in well-stirred cell media for 24 hours that was never replenished over the length of the experiment. In reality though, an implanted sensor is bathed in interstitial fluid whose solutes are constantly being consumed and replenished by the flow of fluid and nutrients out of the vasculature and into the interstitial space. A more accurate and physiologically relevant *in vitro* construct of the provisional matrix should incorporate this element of perfusion into the system. A flow loop with inlets and outlets to the chamber containing the gel covered sensor could be added to provide such perfusion. By allowing for the replenishment of nutrients to the gel system, this design would prevent against the depletion of nutrients in the bulk media phase surrounding the sensor and gel. Additionally, a series of inlets and outlets

would allow for the perfusion of different therapeutics to see their effect on sensor function.

6.2.4 Improving Aspects of the Computational Modeling

The computational models presented in this dissertation described the motion of glucose through a porous media with respect to only one spatial direction. While the assumption still allowed the models to provide very germane and useful information, a more complete model would incorporate more spatial components to account for spatial heterogeneities present in the encapsulating tissue. Additionally, in all the simulations presented, the sensor was assumed to be perfectly efficient in that two electrons would be produced within the sensor for every glucose molecule it encounters. While the focus of the research above was examining how tissue changes would alter the sensing of otherwise functioning sensors, terms could be incorporated to investigate how the biological environment could alter the efficiency by which the glucose oxidase enzyme converts glucose to an electrical signal. The effects of the material properties of the sensors themselves could also be incorporated and help shed light on how the extent of injury and subsequent downstream inflammation upon implantation can be affected by properties such as stiffness of the sensor.

6.2.5 Incorporating New Sensor Technology

While the Medtronic SofSensor has been an industry standard in continuous glucose monitoring, the current state of the art in clinical practice is transitioning to

newer technologies. With regards to Medtronic, the new state of the art design is the Enlite sensor design. This design has a sensor probe that is both smaller and more flexible than the earlier generation SofSensor platform [126]. These design considerations are meant to decrease both the size of the tissue affected by the implantation as well as the effects of micromotion in promoting chronic inflammation. Moving forward, both computational models and experimental designs should be geared towards incorporating new sensor designs.

Appendix A. MATLAB Code

A.1 Computational Model of Glucose Transport through a Fully Formed Capsule

A.1.1 Main Solver Routine, glucosecapsule_solve_c.m

```
function glucosecapsule_solve_c

clear all

global af bd bc lamb ep A D Dmac zc vm km SV P PSV kmac vmac w epmac ep_rat

D_rat a b d b1 b2 N M dy y

% This function is the main solver for solving for the transport of glucose

% out of vessels and through interstitium and the foreign body capsule to

% the surface of a glucose sensor. The program incorporates physiologically

% relevant values, fitted blood plasma values from literature and initial

% conditions from glucosecapsule_ic_c.m to examine the relative effects of the

% inflammation/wound healing process on glucose transport from vasculature

% to a sensor.

%% Definition of model parameters %%

tic

af = 1;              %sensor efficiency. assumed to be perfectly efficient.

bd = 3.02e2;         %uM/nA.

bc = 55.56;          %1 mg/dL = 55.56 uM.

lamb = 2.574e-14;    %mole/(mM-sec).
```

```
ep = 0.6;              %porosity of subcutaneous tissue.

A = 0.0058;            %surface area of sensor probe in cm^2.

D = 3.5e-6;            %diffusion coefficient of glucose in subcutaneous tissue. cm^2/sec.

Dmac = (1.87e-6);      %diffusion coefficient of glucose in FBC. cm^2/sec.

zc = 9.5e-13;          %volume of one cell. L/cell.

vm = 3e-11;            %Vmax of glucose for Michaelis-Menten consumption by adipocytes
in subcutaneous tissue. umol/cell/sec.

km = 6.2e3;            %Michaelis-Menten constant of adipocytes in subcutaneous tissue.
uM.

SV = 15.4;             %Surface to volume ratio of blood vessels. cm^-1.

P = 5e-5;              %Permeability constant for glucose through blood vessels in cm/sec.

PSV = P*SV;            %Product of permeability and surface to volume ratio. 1/sec.

kmac = 6.13e3;         %Michaelis-Menten constant of macrophages in FBC. uM.

vmac = (4.88e-11);     %Vmax of glucose for Michaelis-Menten consumption by
macrophages in FBC. umol/cell/sec.

w = 0.0075;            %Width of fibrous capsule layer in cm.

epmac = 0.6;           %Porosity of FBC. unitless.

ep_rat = ep/epmac;     %Ratio of subcutaneous porosity divided by FBC porosity. no
units.
```

```
D_rat = D/Dmac;        %Ratio of subcutaneous diffusion coefficient divided by FBC
diffusion coefficient. no units.
%==Blood Plasma Concentration for Initial Condition Vector==%
a=[];
b=[];
d=[];
%\\\\\\\\\from data from gough paper\\\\\\\\\\\\\\\\%
%\\\\\\data fit to sum of three gaussians\\\\\\%
%\\ Cp=a(1)*exp(-((t-b(1))/d(1)).^2) + a(2)*exp(-((t-b(2))/d(2)).^2)+a(3)*exp(-((t-
b(3))/d(3)).^2)\\%
a(1)=43.28;          %mg/dL
a(2)=102.2;          %mg/dL
a(3)=1.214e7;        %mg/dL
b(1)=41.38*60;       %sec
b(2)=65.9*60;        %sec
b(3)=5.021e4*60;     %sec
d(1)=12.23*60;       %sec
d(2)=21.73*60;       %sec
d(3)=1.427e4*60;     %sec
%% Mesh definition and solution of PDEs %%
```

```
b1 = 5.07;          %cm. Let y=b1(1-exp(-b2*x)) to make a nonlinearly spaced mesh to
better define behavior at short times.
M = 500;            %Number of spatial iterations in FBC layer.
N = 1000;           %Number of spatial iterations in subcutaneous layer.
yo=0.07;
y=linspace(yo,b1,N+1);
dy=y(2)-y(1);
b2 = (-1./(w)).*(log((b1-y(M))./b1));   %1/cm. equations for dc/dx will be analytically
transformed to make dc/dy.
t0 = 0;
tend = 10000;
t_interval = linspace(t0,tend,4000);    %Timespan of simulation in sec.
Cp = bc.*(a(1).*exp(-((t_interval-b(1))/d(1)).^2) + a(2).*exp(-((t_interval-b(2))/d(2)).^2) +
a(3).*exp(-((t_interval-b(3))/d(3)).^2));  %Blood glucose profile.
Co = [glucosecapsule_ic_c]; %Calls the initial condition vector from subroutine
glucosecapsule_ic_c.m. This routine is outlined below.
sol_init = Co(1:N);  %Initial condition vector. Baseline value in subcutaneous tissue layer.
[tnum,sol] = ode15s(@func, t_interval,sol_init);      %Solution of PDEs as a system of
ODEs.
%Making concentration matrix from solution matrix%
```

```
con_mat = [sol(:,(1:M)) ep_rat.*sol(:,M) sol(:,(M+1:N-1)) ep.*Cp']; %Pieces together the
FBC compartment, interface, native tissue and outer BC into solution matrix.
%Calculating time lag
xcp = find(ep.*Cp==max(ep.*Cp)); %Finds the index of the max value in the time trace at
the last point in the simulation.
tcp = t_interval(xcp)/60; %Uses the above index to find the time at which the peak value
of the time trace at the last point in the simulation occurs.
xg = find(con_mat(:,1)==max(con_mat(:,1))); %Finds the index of the max value in the
time trace at the first point in the simulation (at the sensor surface).
tg = t_interval(xg)/60; %Uses the above index to find the time at which the peak value of
the time trace at the first point in the simulation occurs.
lag = tg - tcp %Calculates lag as the difference between the times calculated above.
%Calculating the attenuation
atten = 1-con_mat(xg,1)./(ep.*Cp(xcp)) %Calculates attenuation as the quotient of the
peak sensor value divided by the peak value in the tissue.
%% Plotting solutions %%
%Plot trace of concentration at sensor surface versus at last point in
%simulation.
figure(1)
hold on
```

```
plot(t_interval/60,con_mat(:,1),'k--','LineWidth',2) %Sensor surface model results.

plot(t_interval/60,ep.*Cp,'k','LineWidth',2)        %Last point in simulation.

xlabel('Time (min)','fontsize',10)

ylabel('Glucose Concentration (\muM)','fontsize',10)

set(gca,'fontsize',10)

legend('C_{surface}(t)','\epsilonC_{p}(t)')

box on

toc

%% ODE-writing subroutine %%

function dcdt = func(t,c)

global af bd bc lamb ep A D Dmac zc vm km SV P PSV kmac vmac w epmac ep_rat

D_rat a b d b1 b2 N M dy y Cp

dcdt = [];

%=FBC equations=%

Cp = bc.*(a(1).*exp(-((t-b(1))/d(1)).^2) + a(2).*exp(-((t-b(2))/d(2)).^2)+ a(3).*exp(-((t-

b(3))/d(3)).^2));

%at y=0%

Qsensor = af.*lamb.*c(1)./epmac;

dcdy_o = Qsensor./(Dmac.*A.*(b1-y(1))*b2);

dcdy2_o=(2.*(c(2)-c(1)-dcdy_o.*dy))/(dy.*dy);
```

```
%Between y=0 and y=L
dcdt(1)=Dmac.*b2.*b2.*((y(1)-b1).^2).*dcdy2_o + Dmac.*b2.*b2.*(y(1)-b1).*(1+1./(log((b1-
y(1))./b1))).*dcdy_o-((vmac.*c(1))./(kmac.*epmac+c(1)).*((1-epmac)./zc));
for k=2:M-1
   dcdt(k)=Dmac.*b2.*b2.*((y(k)-b1).^2).*((c(k+1)-2.*c(k)+c(k-1))./(dy.*dy)) +
Dmac.*b2.*b2.*(y(k)-b1).*(1+1./(log((b1-y(k))./b1))).*(c(k+1)-c(k))./dy-
((vmac.*c(k))./(kmac.*epmac+c(k)).*((1-epmac)./zc));
end
dcdy2_L = (2.*(c(M-1)-c(M)+D_rat.*(c(M+1)-ep_rat.*c(M)))./(dy.*dy);
dcdt(M) = Dmac.*b2.*b2.*((y(M)-b1).^2).*dcdy2_L + Dmac.*(1+1./(log((b1-
y(M))./b1))).*(b2.^2).*((y(M)-b1)).*D_rat.*((c(M+2)-ep_rat.*c(M))./dy)-
((vmac.*c(M))./(kmac.*epmac+c(M)).*((1-epmac)./zc));
%for L<y<N%
%right side of y=L%
c2_1 = ep_rat.*c(M);
%second point of second compartment%
dcdt(M+1) = D.*b2.*b2.*((y(M+2)-b1).^2).*((c(M+2)-2.*c(M+1)+c2_1)./(dy.*dy)) +
D.*b2.*b2.*(y(M+2)-b1).*((c(M+2)-c(M+1))./dy).*(1+1./(log((b1-y(M+2))./b1)))-
((vm.*c(M+1))./(km.*ep+c(M+1)).*((1-ep)./zc)) + PSV.*(Cp-c(M+1)./ep);
for k=M+2:N-2
```

```
    dcdt(k) = D.*b2.*b2.*((y(k+1)-b1).^2).*((c(k+1)-2*c(k)+c(k-1))./(dy*dy)) +
D.*b2.*b2.*(y(k+1)-b1).*((c(k+1)-c(k))./dy).*(1+1./(log((b1-y(M))./b1)))-
((vm.*c(k))./(km.*ep+c(k)).*((1-ep)./zc)) + PSV.*(Cp-c(k)./ep);
end
%for y=N%
dcdy_N = (ep.*Cp-c(N-1))./dy;
dcdy2_N = (ep.*Cp-2*c(N-1)+c(N-2))./(dy*dy);
dcdt(N) = D.*b2.*b2.*((y(N)-b1).^2).*dcdy2_N + D.*b2.*b2.*((y(N)-
b1)).*(dcdy_N).*(1+1./(log((b1-y(N))./b1)))- (vm.*c(N-1))/(km*ep+c(N-1)).*((1-ep)./zc) +
PSV.*(Cp-c(N-1)./ep);
dcdt=dcdt';
```

A.1.2 Initial Condition Solver, glucosecapsule_ic_c.m

```
function [ss_trace]= glucosecapsule_ic_c
global af bd bc lamb ep A D Dmac zc vm km SV P PSV kmac vmac w epmac ep_rat
D_rat a b d b1 b2 N M dy y Cp_exp


% This program is used to find the initial condition for the main solver
% program, glucosecapsule_solve_ic.m. The simulation is run with initial
% conditions set to zero in the FBC layer and a baseline value from
% literature in the subcutaneous tissue to see at what point the system
```

```
% reaches steady state. This is because the FBC is assumed to have no
% vessels and vessels are the only source of glucose considered. The trace
% of concentration as a function of position at that point in time is then
% exported to the main solver to be used as the initial condition vector as
% the vector "ss_trace". It is thought that this vector is representative
% of the standard glucose trace in the tissue before a glucose challenge.


%==Definition of model parameters==%
tic
af = 1;                 %sensor efficiency. assumed to be perfectly efficient.
bd = 3.02e2;            %uM/nA.
bc = 55.56;             %1 mg/dL = 55.56 uM.
lamb = 2.574e-14;       %mole/(mM-sec).
ep = 0.6;               %porosity of subcutaneous tissue. unitless
A = 0.0058;             %surface area of sensor probe in cm^2.
D = 3.5e-6;             %diffusion coefficient of glucose in subcutaneous tissue. cm^2/sec.
Dmac = (1.87e-6);       %diffusion coefficient of glucose in FBC. cm^2/sec.
zc = 9.5e-13;           %volume of one cell. L/cell.
vm = 3e-11;             %Vmax of glucose for Michaelis-Menten consumption by adipocytes
in subcutaneous tissue. umol/cell/sec.
```

```
km = 6.2e3;            %Michaelis-Menten constant of adipocytes in subcutaneous tissue.
uM.
SV = 15.4;             %Surface to volume ratio of blood vessels. cm^-1.
P = 5e-5;              %Permeability constant for glucose through blood vessels in cm/sec.
PSV = P*SV;            %Product of permeability and surface to volume ratio. 1/sec.
kmac = 6.13e3;         %Michaelis-Menten constant of macrophages in FBC. uM.
vmac = (4.88e-11);     %Vmax of glucose for Michaelis-Menten consumption by
macrophages in FBC. umol/cell/sec.
w = 0.0075;            %Width of fibrous capsule layer in cm.
epmac = 0.6;           %porosity of FBC. unitless.
ep_rat = ep/epmac;     %Ratio of subcutaneous porosity divided by FBC porosity. no
units.
D_rat = D/Dmac;        %Ratio of subcutaneous diffusion coefficient divided by FBC
diffusion coefficient. no units.
%==Blood Plasma Concentration for Initial Condition Vector==%
a=[];
b=[];
d=[];
%\\\\\\\\\from data from gough paper\\\\\\\\\\\\\\\%
%\\\\\\data fit to sum of three gaussians\\\\\\%
```

```
%\\ Cp=a(1)*exp(-((t-b(1))/d(1)).^2) + a(2)*exp(-((t-b(2))/d(2)).^2)+a(3)*exp(-((t-
b(3))/d(3)).^2)\\%
a(1)=43.28;          %mg/dL
a(2)=102.2;          %mg/dL
a(3)=1.214e7;        %mg/dL
b(1)=41.38*60;       %sec
b(2)=65.9*60;        %sec
b(3)=5.021e4*60;     %sec
d(1)=12.23*60;       %sec
d(2)=21.73*60;       %sec
d(3)=1.427e4*60;     %sec
 %==Mesh definition and solution of PDEs==%
b1 = 5.07;              %cm. Let y=b1(1-exp(-b2*x)) to make a nonlinearly spaced mesh to
better define behavior at short times.
M = 500;             %Number of spatial iterations in FBC layer.
N = 1000;            %Number of spatial iterations in subcutaneous layer.
yo=0.07;
y=linspace(yo,b1,N+1);
dy=y(2)-y(1);
```

```
b2 = (-1./(w)).*(log((b1-y(M))./b1));   %1/cm. equations for dc/dx will be analytically
transformed to make dc/dy.
t0 = 0;
tend = 10000;
t_interval = linspace(t0,tend,5000);    %Timespan of simulation in sec.
dt = t_interval(2)-t_interval(1);
Cp_exp=a(1)*exp(-((t0-b(1))/d(1)).^2) + a(2)*exp(-((t0-b(2))/d(2)).^2)+a(3)*exp(-((t0-
b(3))/d(3)).^2);  %baseline value of glucose in vessels before bolus injection. Based on
Gough.
sol_init = [zeros(1,M) ep.*bc.*Cp_exp.*ones(1,N-M)];  %Initial condition vector. Zero in
FBC layer because no source. Baseline value in subcutaneous tissue layer
[tnum,sol] = ode15s(@func, t_interval,sol_init);      %Solution of PDEs as a system of
ODEs
%making concentration matrix from solution matrix%
con_mat = [sol(:,(1:M)) ep_rat.*sol(:,M) sol(:,(M+1:N-1))
ep.*bc.*Cp_exp.*ones(length(t_interval),1)];
%==ODE-writing subroutine==%
function dcdt = func(t,c)
global af bd bc lamb ep A D Dmac zc vm km SV P PSV kmac vmac w epmac ep_rat
D_rat a b d b1 b2 N M dy y Cp_exp
```

```
dcdt = [];

 %=FBC equations=%

Cp = bc.*Cp_exp;

%at y=0%

Qsensor = af.*lamb.*c(1)./epmac;

dcdy_o = Qsensor./(Dmac.*A.*(b1-y(1))*b2);

dcdy2_o=(2.*(c(2)-c(1)-dcdy_o.*dy))/(dy.*dy);

dcdt(1)=Dmac.*b2.*b2.*((y(1)-b1).^2).*dcdy2_o + Dmac.*b2.*b2.*(y(1)-b1).*(1+1./(log((b1-

y(1))./b1))).*dcdy_o-((vmac.*c(1))./(kmac.*epmac+c(1)).*((1-epmac)./zc));

for k=2:M-1

   dcdt(k)=Dmac.*b2.*b2.*((y(k)-b1).^2).*((c(k+1)-2.*c(k)+c(k-1))./(dy.*dy)) +

Dmac.*b2.*b2.*(y(k)-b1).*(1+1./(log((b1-y(k))./b1))).*(c(k+1)-c(k))./dy-

((vmac.*c(k))./(kmac.*epmac+c(k)).*((1-epmac)./zc));

end

dcdy2_L = (2.*(c(M-1)-c(M)+D_rat.*(c(M+1)-ep_rat.*c(M)))))./(dy.*dy);

dcdt(M) = Dmac.*b2.*b2.*((y(M)-b1).^2).*dcdy2_L + Dmac.*(1+1./(log((b1-

y(M))./b1))).*(b2.^2).*((y(M)-b1)).*D_rat.*((c(M+2)-ep_rat.*c(M))./dy)-

((vmac.*c(M))./(kmac.*epmac+c(M)).*((1-epmac)./zc));

%for L<y<N%

%right side of y=L%
```

```
c2_1 = ep_rat.*c(M);

%second point of second compartment%

dcdt(M+1) = D.*b2.*b2.*((y(M+2)-b1).^2).*((c(M+2)-2.*c(M+1)+c2_1)./(dy.*dy)) +

D.*b2.*b2.*(y(M+2)-b1).*((c(M+2)-c(M+1))./dy).*(1+1./(log((b1-y(M+2))./b1)))-

((vm.*c(M+1))./(km.*ep+c(M+1)).*((1-ep)./zc)) + PSV.*(Cp-c(M+1)./ep);

for k=M+2:N-2

   dcdt(k) = D.*b2.*b2.*((y(k+1)-b1).^2).*((c(k+1)-2*c(k)+c(k-1))./(dy*dy)) +

D.*b2.*b2.*(y(k+1)-b1).*((c(k+1)-c(k))./dy).*(1+1./(log((b1-y(M))./b1)))-

((vm.*c(k))./(km.*ep+c(k)).*((1-ep)./zc)) + PSV.*(Cp-c(k)./ep);

end

%for y=N%

dcdy_N = (ep.*Cp-c(N-1))./dy;

dcdy2_N = (ep.*Cp-2*c(N-1)+c(N-2))./(dy*dy);

dcdt(N) = D.*b2.*b2.*((y(N)-b1).^2).*dcdy2_N + D.*b2.*b2.*((y(N)-

b1)).*(dcdy_N).*(1+1./(log((b1-y(N))./b1)))- (vm.*c(N-1))/(km*ep+c(N-1)).*((1-ep)./zc) +

PSV.*(Cp-c(N-1)./ep);

dcdt=dcdt';
```

A.2. Computational Model of Transport through the Provisional Matrix in a Whole Blood Solution, glucosecapsule_noflux.m

```
function glucosecapsule_ic_time_noflux
```

```
global af bd bc lamb ep A D Dmac zc vm km SV P PSV kmac vmac w epmac ep_rat
D_rat a b d b1 b2 N M dy y Cp_exp


% This program is used to find the normalized concentration of glucose with
% respect to time at the sensor surface.


%==Definition of model parameters==%
tic
af = 1;              %sensor efficiency. assumed to be perfectly efficient.
bd = 3.02e2;         %uM/nA.
bc = 55.56;          %1 mg/dL = 55.56 uM.
lamb = 2.574e-14;    %mole/(mM-sec).
ep = 0.55;           %porosity of bulk blood. unitless
A = 0.0058;          %surface area of sensor probe in cm^2.
D = 3.5e-6;          %diffusion coefficient of glucose in bulk blood. cm^2/sec.
Dmac = (1.87e-6);    %diffusion coefficient of glucose in provisional matrix. cm^2/sec.
zc = 9.5e-13;        %volume of one cell. L/cell.
vm = 1.357e-12;      %Vmax of glucose for Michaelis-Menten consumption by
erythrocytes. umol/cell/sec.
km = 6.2e3;          %Michaelis-Menten constant of erythrocytes uM.
```

```
kmac = 6.13e3;          %Michaelis-Menten constant of macrophages in FBC. uM.
vmac = 4.88e-11;        %Vmax of glucose for Michaelis-Menten consumption by
macrophages. umol/cell/sec.
w = 0.0075;             %Width of provisional matrix layer in cm.
epmac = 0.91;           %porosity of provisional matrix. unitless.
ep_rat = ep/epmac;      %Ratio of subcutaneous porosity divided by FBC porosity. no
units.
D_rat = D/Dmac;         %Ratio of subcutaneous diffusion coefficient divided by FBC
diffusion coefficient. no units.
%==Mesh definition and solution of PDEs==%
b1 = 1.25;              %cm. Let y=b1(1-exp(-b2*x)) to make a nonlinearly spaced mesh to
better define behavior at short times.
M = 500;                %Number of spatial iterations in FBC layer.
N = 1000;               %Number of spatial iterations in subcutaneous layer.
yo=0.07;
y=linspace(yo,b1,N+1);
dy=y(2)-y(1);
b2 = (-1./(w)).*(log((b1-y(M))./b1))   %1/cm. equations for dc/dx will be analytically
transformed to make dc/dy.
 t0 = 0;
```

```
tend = 86400;

t_interval = linspace(t0,tend,5000);    %Timespan of simulation in sec.

dt = t_interval(2)-t_interval(1);

Cp_exp= 55./ep;  %baseline value of glucose in vessels before bolus injection. Based on
Gough.

sol_init = [bc.*Cp_exp.*ones(1,N)];

[tnum,sol] = ode15s(@func, t_interval,sol_init);      %Solution of PDEs as a system of
ODEs

%making concentration matrix from solution matrix%

con_mat = [sol(:,(1:M)) ep_rat.*sol(:,M) sol(:,(M+1:N))];

%==Plotting solutions==%

plot(t_interval((1:end))./3600,con_mat((1:end),1)./con_mat(1,1),'k--','LineWidth',2)

%==ODE-writing subroutine==%

function dcdt = func(t,c)

global af bd bc lamb ep A D Dmac zc vm km SV P PSV kmac vmac w epmac ep_rat
D_rat a b d b1 b2 N M dy y Cp_exp

dcdt = [];

 %=FBC equations=%

Cp = bc.*Cp_exp;

%at y=0%
```

```
Qsensor = af.*lamb.*c(1)./epmac;
dcdy_o = Qsensor./(Dmac.*A.*(b1-y(1))*b2);
dcdy2_o=(2.*(c(2)-c(1)-dcdy_o.*dy))/(dy.*dy);
dcdt(1)=Dmac.*b2.*b2.*((y(1)-b1).^2).*dcdy2_o + Dmac.*b2.*b2.*(y(1)-b1).*(1+1./(log((b1-
y(1))./b1))).*dcdy_o-((vmac.*c(1))./(kmac.*epmac+c(1)).*((1-epmac)./zc));
for k=2:M-1
   dcdt(k)=Dmac.*b2.*b2.*((y(k)-b1).^2).*((c(k+1)-2.*c(k)+c(k-1))./(dy.*dy)) +
Dmac.*b2.*b2.*(y(k)-b1).*(1+1./(log((b1-y(k))./b1))).*(c(k+1)-c(k))./dy-
((vmac.*c(k))./(kmac.*epmac+c(k)).*((1-epmac)./zc));
end
dcdy2_L = (2.*(c(M-1)-c(M)+D_rat.*(c(M+1)-ep_rat.*c(M)))./(dy.*dy);
dcdt(M) = Dmac.*b2.*b2.*((y(M)-b1).^2).*dcdy2_L + Dmac.*(1+1./(log((b1-
y(M))./b1))).*(b2.^2).*((y(M)-b1)).*D_rat.*((c(M+2)-ep_rat.*c(M))./dy)-
((vmac.*c(M))./(kmac.*epmac+c(M)).*((1-epmac)./zc));
%for L<y<N%
%right side of y=L%
c2_1 = ep_rat.*c(M);
%second point of second compartment%
```

```
dcdt(M+1) = D.*b2.*b2.*((y(M+1)-b1).^2).*((c(M+2)-2.*c(M+1)+c2_1)./(dy.*dy)) +
D.*b2.*b2.*(y(M+1)-b1).*((c(M+2)-c(M+1))./dy).*(1+1./(log((b1-y(M+1))./b1)))-
((vm.*c(M+1))./(km.*ep+c(M+1)).*((1-ep)./zc));
for k=M+2:N-1
   dcdt(k) = D.*b2.*b2.*((y(k)-b1).^2).*((c(k+1)-2*c(k)+c(k-1))./(dy*dy)) + D.*b2.*b2.*(y(k)-
b1).*((c(k+1)-c(k))./dy).*(1+1./(log((b1-y(k))./b1)))-((vm.*c(k))./(km.*ep+c(k)).*((1-ep)./zc));
end
%for y=N%
dcdy_N = 0; %because no flux boundary condition
dcdy2_N = (2.*(c(N-1)-c(N)))./(dy*dy);
dcdt(N) = D.*b2.*b2.*((y(N)-b1).^2).*dcdy2_N - (vm.*c(N))/(km*ep+c(N)).*((1-ep)./zc);
dcdt=dcdt';
```

A.3 Computational Model of Glucose Flux through Fibrin Gel, glucosegel_noflux_vmac.m

```
function [con_mat] = glucosegel_noflux_vmac(vmac)
clear all
global af bd bc lamb ep A D Dmac zc vm km SV P PSV kmac vmac w epmac ep_rat
D_rat a b d b1 b2 N M dy y Cp_exp epgel
```

```
% This program is used to the find the normalized concentration of glucose  on the
sensor surface with respect to time for a varying number of values of Vmax in the gel.
These values will then be compared to experimental traces in model_compare.m.


%==Definition of model parameters==%
tic
af = 1;                %sensor efficiency. assumed to be perfectly efficient.
bd = 3.02e2;           %uM/nA.
bc = 55.56;            %1 mg/dL = 55.56 uM.
lamb = 2.574e-14;      %mole/(mM-sec).
ep = 1;                %porosity of bulk fluid. unitless
A = 0.0058;            %surface area of sensor probe in cm^2.
D = 6.8e-6;            %diffusion coefficient of glucose in fluid. cm^2/sec.
Dmac = 6.8e-6;         %diffusion coefficient of glucose in gel. cm^2/sec.
zc = 2.1e-12;          %volume of one cell. L/cell.
kmac = [6.13e3];       %Michaelis-Menten constant of macrophages in gel. uM.
% vmac = [input from the function line];     Vmax of glucose for Michaelis-Menten
consumption by macrophages in FBC. umol/cell/sec.
w = 0.43;              %Width of gel in cm.
epmac = 1-0.0257;      %fraction of gel that is cells. unitless.
```

```
ep_rat = ep/epmac;      %Ratio of fluid porosity divided by gel porosity. no units.

D_rat = D/Dmac;         %Ratio of fluid diffusion coefficient divided by gel diffusion
coefficient. no units.

%==Mesh definition and solution of PDEs==%

b1 = 1.1;               %cm. Let y=b1(1-exp(-b2*x)) to make a nonlinearly spaced mesh to
better define behavior at short times.

M = 250;                %Number of spatial iterations in gel layer.

N = 500;                %Number of spatial iterations in media layer.

yo=0.07;

y=linspace(yo,b1,N+1);

dy=y(2)-y(1);

b2 = (-1./(w)).*(log((b1-y(M))./b1));   %1/cm. equations for dc/dx will be analytically
transformed to make dc/dy.


t0 = 0;

tend = 7200;

t_interval = linspace(t0,tend,1000);    %Timespan of simulation in sec.

dt = t_interval(2)-t_interval(1);

Cp_exp= 100;  %baseline value of glucose

sol_init = [bc.*Cp_exp.*ones(1,length(vmac)*N)];
```

```
[tnum,sol] = ode15s(@func, t_interval,sol_init);      %Solution of PDEs as a system of
ODEs
%=Making concentration matrix from solution matrix=%
con_mat=[];
con_mat(:,(1:N+1)) = [sol(:,(1:M)) ep_rat.*sol(:,M) sol(:,(M+1:N))];
for i=1:length(vmac)-1
    con_mat(:,(i*N+i+1:(i+1).*N+i+1)) = [sol(:,(i.*N+1:i*N+M)) ep_rat.*sol(:,i*N+M)
sol(:,(i*N+M+1:(i+1)*N))];
end
 % %==Plotting solutions==%
hold all
for i=1:length(vmac)-1
    plot(t_interval./3600,con_mat(:,1)./bc./Cp_exp,'--','LineWidth',2)
    plot(t_interval./3600,con_mat(:,i*N+i+1)./bc./Cp_exp,'--','LineWidth',2)
    box on
end
toc
%==ODE-writing subroutine==%
function dcdt = func(t,c)
```

```
global af bd bc lamb ep A D Dmac zc vm km SV P PSV kmac vmac w epmac ep_rat
D_rat a b d b1 b2 N M dy y Cp_exp epgel
dcdt = [];


%=FBC equations=%
Cp = bc.*Cp_exp;
%at y=0%
Qsensor = af.*lamb.*c(1)./epmac;
dcdy_o = Qsensor./(Dmac.*A.*(b1-y(1))*b2);
dcdy2_o=(2.*(c(2)-c(1)-dcdy_o.*dy))/(dy.*dy);
dcdt(1)=Dmac.*b2.*b2.*((y(1)-b1).^2).*dcdy2_o + Dmac.*b2.*b2.*(y(1)-b1).*(1+1./(log((b1-
y(1))./b1))).*dcdy_o-((vmac(1).*c(1))./(kmac.*epmac+c(1)).*((1-epmac)./zc));
for k=2:M-1
   dcdt(k)=Dmac.*b2.*b2.*((y(k)-b1).^2).*((c(k+1)-2.*c(k)+c(k-1))./(dy.*dy)) +
Dmac.*b2.*b2.*(y(k)-b1).*(1+1./(log((b1-y(k))./b1))).*(c(k+1)-c(k))./dy-
((vmac(1).*c(k))./(kmac.*epmac+c(k)).*((1-epmac)./zc));
end
dcdy2_L = (2.*(c(M-1)-c(M)+D_rat.*(c(M+1)-ep_rat.*c(M)))./(dy.*dy);
```

```
dcdt(M) = Dmac.*b2.*b2.*((y(M)-b1).^2).*dcdy2_L + Dmac.*(1+1./(log((b1-
y(M))./b1))).*(b2.^2).*((y(M)-b1)).*D_rat.*((c(M+2)-ep_rat.*c(M))./dy)-
((vmac(1).*c(M))./(kmac.*epmac+c(M)).*((1-epmac)./zc));
%for L<y<N%
%right side of y=L%
c2_1 = ep_rat.*c(M);
%second point of second compartment%
dcdt(M+1) = D.*b2.*b2.*((y(M+1)-b1).^2).*((c(M+2)-2.*c(M+1)+c2_1)./(dy.*dy)) +
D.*b2.*b2.*(y(M+1)-b1).*((c(M+2)-c(M+1))./dy).*(1+1./(log((b1-y(M+1))./b1)))-
((vm.*c(M+1))./(km.*ep+c(M+1)).*((1-ep)./zc));
for k=M+2:N-1
   dcdt(k) = D.*b2.*b2.*((y(k)-b1).^2).*((c(k+1)-2*c(k)+c(k-1))./(dy*dy)) + D.*b2.*b2.*(y(k)-
b1).*((c(k+1)-c(k))./dy).*(1+1./(log((b1-y(k))./b1)))-((vm.*c(k))./(km.*ep+c(k)).*((1-ep)./zc));
end
%for y=N%
dcdy_N = 0; %because no flux boundary condition
dcdy2_N = (2.*(c(N-1)-c(N)))./(dy*dy);
dcdt(N) = D.*b2.*b2.*((y(N)-b1).^2).*dcdy2_N - (vm.*c(N))/(km*ep+c(N)).*((1-ep)./zc);
%=for the other values of vmac=%
for i=1:length(vmac)-1
```

```
    Qsensor1 = af.*lamb.*c(i*N+1)./epmac;
    dcdy_o1 = Qsensor1./(Dmac.*A.*(b1-y(1))*b2);
    dcdy2_o1=(2.*(c(i.*N+2)-c(i.*N+1)-dcdy_o1.*dy))/(dy.*dy);
    dcdt(i.*N+1)=Dmac.*b2.*b2.*((y(1)-b1).^2).*dcdy2_o1 + Dmac.*b2.*b2.*(y(1)-
b1).*(1+1./(log((b1-y(1))./b1))).*dcdy_o1-
((vmac(i+1).*c(i*N+1))./(kmac.*epmac+c(i*N+1)).*((1-epmac)./zc));
    for k=2:M-1
        dcdt(i.*N+k)=Dmac.*b2.*b2.*((y(k)-b1).^2).*((c(i.*N+k+1)-2.*c(i.*N+k)+c(i.*N+k-
1))./(dy.*dy)) + Dmac.*b2.*b2.*(y(k)-b1).*(1+1./(log((b1-y(k))./b1))).*(c(i.*N+k+1)-
c(i.*N+k))./dy-((vmac(i+1).*c(i.*N+k))./(kmac.*epmac+c(i.*N+k)).*((1-epmac)./zc));
    end
    dcdy2_L = (2.*(c(i.*N+M-1)-c(i.*N+M)+D_rat.*(c(i.*N+M+1)-
ep_rat.*c(i.*N+M)))))./(dy.*dy);
    dcdt(i.*N+M) = Dmac.*b2.*b2.*((y(M)-b1).^2).*dcdy2_L + Dmac.*(1+1./(log((b1-
y(M))./b1))).*(b2.^2).*((y(M)-b1)).*D_rat.*((c(i.*N+M+2)-ep_rat.*c(i.*N+M))./dy)-
((vmac(i+1).*c(i.*N+M))./(kmac.*epmac+c(i.*N+M)).*((1-epmac)./zc));
    c2_1 = ep_rat.*c(i.*N+M);
    %second point of second compartment%
    dcdt(i.*N+M+1) = D.*b2.*b2.*((y(M+1)-b1).^2).*((c(i.*N+M+2)-
2.*c(i.*N+M+1)+c2_1)./(dy.*dy)) + D.*b2.*b2.*(y(M+1)-b1).*((c(i.*N+M+2)-
```

```
c(i.*N+M+1))./dy).*(1+1./(log((b1-y(M+1))./b1)))-
((vm.*c(i.*N+M+1))./(km.*ep+c(i.*N+M+1)).*((1-ep)./zc));
   for k=M+2:N-1
      dcdt(i.*N+k) = D.*b2.*b2.*((y(k)-b1).^2).*((c(i.*N+k+1)-2*c(i.*N+k)+c(i.*N+k-
1))./(dy*dy)) + D.*b2.*b2.*(y(k)-b1).*((c(i.*N+k+1)-c(i.*N+k))./dy).*(1+1./(log((b1-
y(k))./b1)))-((vm.*c(i.*N+k))./(km.*ep+c(i.*N+k)).*((1-ep)./zc));
   end
   dcdy_N = 0; %because no flux boundary condition
   dcdy2_N = (2.*(c((i+1).*N-1)-c((i+1).*N)))./(dy*dy);
   dcdt((i+1).*N) = D.*b2.*b2.*((y(N)-b1).^2).*dcdy2_N -
(vm.*c((i+1).*N))/(km*ep+c((i+1).*N)).*((1-ep)./zc);
end
dcdt=dcdt';
```

A.4 Algorithm for Finding Best Fit of Experimental Data from glucosegel_noflux_vmac, model_compare.m

```
%model_compare.m

%This program compares modeled normalized sensor traces to experimentally
%observed traces by calculating the R^2 values between experimental and modeled
cases.  Those fits with the highest R^2 values to experimental traces are considered to be
best fits.
```

```
s=openfig('MeanMacValues_with_error_gen.fig'); %Loads the experimental traces
h=findobj(s,'type','line');
x=get(h,'xdata');
y=get(h,'ydata');

mac=cell2mat(y(2,1)); %Turns experimental sensor trace into numerical vector from a
cell
pma=cell2mat(y(3,1));
lps=cell2mat(y(4,1));

model_trace=glucosegel_noflux_vmac; %Load modeled results
N=500; %Number of spatial iterations in modeled results
for i=1:length(vmac)-1
   sensor_model=[model_trace(:,1) con_mat(:,i*N+i+1)];
end
%Calculate the total sum of squares for each case
sst_mac = sum((mac-mean(mac)).^2);
sst_pma = sum((pma-mean(pma)).^2);
sst_lps = sum((lps-mean(lps)).^2);
```

```
%Calculate the residual sum of squares for each case
for i=1:size(sensor_model,2)
    ssr_mac(:,i) = sum((mac-sensor_model(:,i)).^2);
    ssr_pma(:,i) = sum((pma-sensor_model(:,i)).^2);
    ssr_lps(:,i) = sum((lps-sensor_model(:,i)).^2);
end
%Calculate the R^2 value for each case
for i=1:size(sensor_model,2)
    r2_mac(:,i) = 1-ssr_mac(:,i)./sst_mac;
    r2_pma(:,i) = 1-ssr_pma(:,i)./sst_pma;
    r2_lps(:,i) = 1-ssr_lps(:,i)./sst_lps;
end
```

References

1. National Diabetes Fact Sheet, 2007. Department of Health and Human Services 2007.

2. Economic Costs of Diabetes in the U.S. in 2007. American Diabetes Association, 2008. p. 596-615.

3. Bloomgarden ZT. Treatment Issues in Type 1 Diabetes. Diabetes Care 2002;25(1):230-238.

4. Buckingham B, Caswell K, Wilson DM. Real-time continuous glucose monitoring. Current Opinion in Endocrinology, Diabetes and Obesity 2007;14(4):288-295.

5. Product News: Low Glucose Suspend Technology for Insulin Pumps. Nurse Practicioner 2013;38(12):53.

6. Garg SK. The future of continuous glucose monitoring. Diabetes Technol Ther 2009 Jun;11 Suppl 1:S1-3.

7. Skyler JS. Continuous glucose monitoring: an overview of its development. Diabetes Technol Ther 2009 Jun;11 Suppl 1:S5-10.

8. Wisniewski N, Klitzman B, Miller B, Reichert WM. Decreased analyte transport through implanted membranes: Differentiation of biofouling from tissue effects. Journal of biomedical materials research 2001;57(4):513-521.

9. Wilson GS, Gifford R. Biosensors for real-time in vivo measurements. Biosensors & bioelectronics 2005;20(12):2388-2403.

10. Reichert WM, Sharkawy AA. Active Implants: Biosensors. Handbook of Biomaterials Evaluation: Scientific, Technical, and Clinical Testing of Implant Materials. Philadelphia, PA: Taylor and Francis, 1999. p. 439-460.

11. Frost MC, Meyerhoff ME. Implantable chemical sensors for real-time clinical monitoring: progress and challenges. Current Opinion in Chemical Biology 2002;6(5):633-641.

12. Clark H, Barbari TA, Stump K, Rao, G. Histologic evaluation of the inflammatory response around implanted hollow fiber membranes. Journal of biomedical materials research 2000;52(1):183-192.

13. Dungel P, Long N, Yu B, Moussy Y, Moussy F. Study of the effects of tissue reactions on the function of implanted glucose sensors. Journal of biomedical materials research 2007;85A(3):699-706.

14. Anderson JM. Biological Responses to Materials. Annual review of materials science 2001;31(1):81.

15. Rebrin K, Fischer U, Hahn von Dorsche H, von Woetke T, Abel P, Brunstein E. Subcutaneous glucose monitoring by means of electrochemical sensors: fiction or reality? Journal of biomedical engineering 1992 Jan;14(1):33-40.

16. Gerritsen M, Jansen JA, Kros A, Vriezema DM, Sommerdijk NAJM, Nolte RJM, et al. Influence of inflammatory cells and serum on the performance of implantable glucose sensors. Journal of biomedical materials research 2001;54(1):69-75.

17. Koschwanez HE, Yap FY, Klitzman B, Reichert WM. In vitro and in vivo characterization of porous poly-L-lactic acid coatings for subcutaneously implanted glucose sensors. Journal of biomedical materials research 2008;87A(3):792-807.

18. Yu B, Ju Y, West L, Moussy Y, Moussy F. An investigation of long-term performance of minimally invasive glucose biosensors. Diabetes technology & therapeutics 2007;9(3):265-275.

19. Norton LW, Koschwanez HE, Wisniewski NA, Klitzman B, Reichert WM. Vascular endothelial growth factor and dexamethasone release from nonfouling sensor coatings affect the foreign body response. Journal of biomedical materials research Part A 2007;81(4):858-869.

20. Patil SD, Papadmitrakopoulos F, Burgess DJ. Concurrent delivery of dexamethasone and VEGF for localized inflammation control and angiogenesis. Journal of Controlled Release 2007;117(1):68-79.

21. Gerritsen M, Jansen JA, Lutterman JA. Performance of subcutaneously implanted glucose sensors for continuous monitoring. Netherlands journal of medicine 1999;54(4):167-179.

22. Gifford R, Kehoe JJ, Barnes SL, Kornilayev BA, Alterman MA, Wilson GS. Protein interactions with subcutaneously implanted biosensors. Biomaterials 2006;27(12):2587-2598.

23. Klueh U, Liu Z, Ouyang T, Cho B, Feldman B, Henning TP, et al. Blood-Induced Interference of Glucose Sensor Function in Vitro: Implications for in Vivo Sensor Function. Journal of Diabetes Science and Technology 2007;1(6):842-849.

24. Wisniewski N, Moussy F, Reichert WM. Characterization of implantable biosensor membrane biofouling. Fresenius' journal of analytical chemistry 2000;366(6-7):611-621.

25. Zhang Y, Hu Y, Wilson GS, Moatti-Sirat D, Poitout V, Reach G. Elimination of the Acetaminophen Interference in an Implantable Glucose Sensor. Analytical Chemistry 1994;66(7):1183-1188.

26. Bindra DS, Zhang Y, Wilson GS, Sternberg R, Thevenot DR, Moatti D, et al. Design and in vitro studies of a needle-type glucose sensor for subcutaneous monitoring. Analytical Chemistry 1991;63(17):1692-1696.

27. Moatti-Sirat D, Velho G, Reach G. Evaluating in vitro and in vivo the interference of ascorbate and acetaminophen on glucose detection by a needle-type glucose sensor. Biosensors and Bioelectronics 1992;7(5):345-352.

28. Ahmed N, Kansara M, Berridge MV. Acute regulation of glucose transport in a monocyte-macrophage cell line: Glut-3 affinity for glucose is enhanced during the respiratory burst. Biochemical Journal 1997;327:369-375.

29. Jones RG, Thompson CB. Revving the Engine: Signal Transduction Fuels T Cell Activation. Immunity 2007;27(2):173-178.

30. Blagih J, Jones RG. Polarizing Macrophages through Reprogramming of Glucose Metabolism. Cell Metabolism 2012;15(6):793-795.

31. Haschemi A, Kosma P, Gille L, Evans Charles R, Burant Charles F, Starkl P, et al. The Sedoheptulose Kinase CARKL Directs Macrophage Polarization through Control of Glucose Metabolism. Cell Metabolism 2012;15(6):813-826.

32. Kindt T, Osborne B, Goldsby R. Kuby Immunology. 6th ed. New York, New York: W.H. Freeman and Co., 2006.

33. Babior BM. Oxygen-Dependent Microbial Killing by Phagocytes. The New England Journal of Medicine 1978;298(12):659-668.

34. Fubini B, Hubbard A. Reactive oxygen species (ROS) and reactive nitrogen species (RNS) generation by silica in inflammation and fibrosis. Free Radical Biology and Medicine 2003;34(12):1507-1516.

35. Kiyotaki C, Peisach J, Bloom BR. Oxygen metabolism in cloned macrophage cell lines: glucose dependence of superoxide production, metabolic and spectral analysis. Journal of immunology 1984;132(2):857-866.

36. Rist RJ, Jones GE, Naftalin RJ. Effects of macrophage colony-stimulating factor and phorbol myristate acetate on 2-D-deoxyglucose transport and superoxide production in rat peritoneal macrophages. Biochemical Journal 1991;278:119-128.

37. Thomsen P, Gretzer C. Macrophage interactions with modified material surfaces. Current Opinion in Solid State and Materials Science 2001;5(2-3):163-176.

38. Schwende H, Fitzke E, Ambs P, Dieter P. Differences in the state of differentiation of THP-1 cells induced by phorbol ester and 1,25-dihydroxyvitamin D3. Journal of leukocyte biology 1996;59(4):555-561.

39. Sweet MJ, Hume DA. Endotoxin signal transduction in macrophages. Journal of leukocyte biology 1996;60(1):8-26.

40. Haeffner A, Thieblemont N, Deas O, Marelli O, Charpentier B, Senik A, et al. Inhibitory effect of growth hormone on TNF-alpha secretion and nuclear factor-kappaB translocation in lipopolysaccharide-stimulated human monocytes. The Journal of Immunology 1997;158(3):1310-1314.

41. Heumann D, Roger T. Initial responses to endotoxins and Gram-negative bacteria. Clinica Chimica Acta 2002;323(1-2):59-72.

42. Fukuzumi M, Shinomiya H, Shimizu Y, Ohishi K, Utsumi S. Endotoxin-induced enhancement of glucose influx into murine peritoneal macrophages via GLUT1. Infection and Immunity 1996;64(1):108-112.

43. Gamelli RL, Liu H, He LK, Hofmann CA. Augmentations of glucose uptake and glucose transporter-1 in macrophages following thermal injury and sepsis in mice. Journal of leukocyte biology 1996;59(5):639-647.

44. Sherry CL, O'Connor JC, Kramer JM, Freund GG. Augmented Lipopolysaccharide-Induced TNF-Alpha Production by Peritoneal Macrophages in Type 2 Diabetic Mice Is Dependent on Elevated Glucose and Requires p38 MAPK. The Journal of Immunology 2007;178(2):663-670.

45. Pedley KC, Jones GE, Magnani M, Rist RJ, Naftalin RJ. Direct observation of hexokinase translocation in stimulated macrophages. Biochemical Journal 1993;291:515-522.

46. Clark HR, Barbari TA, Rao G. Modeling the response time of an in vivo glucose affinity sensor. Biotechnology progress 1999;15(2):259-266.

47. Sharkawy AA, Klitzman B, Truskey GA, Reichert WM. Engineering the tissue which encapsulates subcutaneous implants. I. Diffusion properties. Journal of Biomedical materials research 1997;37(3):401-412.

48. Yuan F. Transvascular drug delivery in solid tumors. Seminars in radiation oncology 1998 Jul;8(3):164-175.

49. Ciaraldi TP, Kolterma OG, Siegel JA, Olefsky JM. Insulin-stimulated glucose transport in human adipocytes. American journal of physiology: Gastrointestinal and liver physiology 1979;236(6):621-625.

50. Koschwanez HE. The Effect of Porous Ploy-L-Lactic Acid Coatings on Tissue Response and Subsequent Glucose Sensor Performance [PhD Dissertation]. Durham, NC USA: Duke University; 2009.

51. Armour JC, Lucisano JY, McKean BD, Gough DA. Application of chronic intravascular blood glucose sensor in dogs. Diabetes 1990;39(12):1519-1526.

52. Kholodenko BN, Hoek JB, Westerhoff HV, Brown GC. Quantification of information transfer via cellular signal transduction pathways. Febs Letters 1997;419(2):430-434.

53. Updike SJ, Shults MC, Rhodes RK, Gilligan BJ, Luebow JO, von Heimburg D. Enzymatic glucose sensors. Improved long-term performance in vitro and in vivo. Asaio J 1994 Apr-Jun;40(2):157-163.

54. Sieminski AL, Gooch KJ. Biomaterial-microvasculature interactions. Biomaterials 2000;21(22):2233-2241.

55. Sharkawy AA, Klitzman B, Truskey GA, Reichert WM. Engineering the tissue which encapsulates subcutaneous implants. III. Effective tissue response times. Journal of biomedical materials research 1998;40(4):598-605.

56. Ward WK, Wood MD, Troupe JE. Understanding Spontaneous Output Fluctuations of an Amperometric Glucose Sensor: Effect of Inhalation Anesthesia and Use of a Nonenzyme Containing Electrode. Asaio J 2000;46(5):540-546.

57. Dewhirst MW, Tso CY, Oliver R, Gustafson CS, Secomb TW, Gross JF. Morphologic and Hemodynamic Comparison of Tumor and Healing Normal Tissue

Microvasculature. International Journal of Radiation Oncology Biology Physics 1989 Jul;17(1):91-99.

58. Novak MT, Yuan F, Reichert WM. Modeling the relative impact of capsular tissue effects on implanted glucose sensor time lag and signal attenuation. Analytical and Bioanalytical Chemistry 2010;398(4):1695-1705.

59. Ginsberg BH. The FDA Panel Advises Approval of the First Continuous Glucose Sensor. Diabetes technology & therapeutics 1999;1(2):203-204.

60. Mastrototaro JJ. The MiniMed Continuous Glucose Monitoring System. Diabetes technology & therapeutics 2000;2(Supplement 1):S13-S18.

61. Klueh U, Liu Z, Feldman B, Henning TP, Cho B, Ouyang T, et al. Metabolic Biofouling of Glucose Sensors *in Vivo*: Role of Tissue Microhemorrhages. Journal of Diabetes Science and Technology 2011;5(3):583-595.

62. Hartley PS, Savill J, Brown SB. The death of human platelets during incubation in citrated plasma involves shedding of CD42b and aggregation of dead platelets. Thrombosis and Haemostasis 2006;95(1):100-106.

63. Hirsh J, Anand SS, Halperin JL, Fuster V. Guide to Anticoagulant Therapy: Heparin : A Statement for Healthcare Professionals From the American Heart Association. Circulation 2001;103:2994-3018.

64. Turgeon ML. Clinical Hematology: Theory and Procedures. 4 ed. Philadelphia, PA: Lippincott Williams and Wilkins, 2005.

65. Carr ME, Shen LL, Jan H. Mass-length ratio of fibrin fibers from gel permeation and light scattering. Biopolymers 1977;16(1):1-15.

66. Truskey GA, Yuan F, Katz DF. Transport Phenomena in Biological Systems. 1 ed. Upper Saddle River, NJ: Pearson Prentice Hall, 2004.

67. Collet J-P, Shuman H, Ledger RE, Lee S, Weisel JW. The elasticity of an individual fibrin fiber in a clot. Proceedings of the National Academy of Science 2005;102(26):9133-9137.

68. Yang H, Wang D, Engelstad K, Bagay L, Wei Y, Rotstein M, et al. Glut1 deficiency syndrome and erythrocyte glucose uptake assay. Annals of Neurology 2011;70(6):996-1005.

69. Nefesh I, Bauskin AR, Alkalay I, Golembo M, Ben-Neriah Y. IL-3 facilitates lymphocyte hexose transport by enhancing the intrinsic activity of the transport system. International Immunology 1991;3(8):827-831.

70. Tan AS, Ahmed N, Berridge MV. Acute Regulation of Glucose Transport After Activation of Human Peripheral Blood Neutrophils by Phorbol Myristate Acetate, fMLP, and Granulocyte-Macrophage Colony-Stimulating Factor. 1998. p. 649-655.

71. Nurdin N, Francois P, Mugnier Y, Krumeich J, Moret M, Aronsson BO, et al. Haemocompatibility evaluation of DLC-and SiC-coated surfaces. European Cells and Materials 2003;5:17-28.

72. Carruthers A, Melchior DL. Transport of alpha- and beta-D-glucose by the intact human red cell. Biochemistry 1985;24(15):4244-4250.

73. Carruthers A. Facilitated diffusion of glucose. Physiological Reviews 1990;70(4):1135-1176.

74. Cloherty EK, Levine KB, Carruthers A. The Red Blood Cell Glucose Transporter Presents Multiple, Nucleotide-Sensitive Sugar Exit Sites. Biochemistry 2001;40(51):15549-15561.

75. Novak MT, Yuan F, Reichert WM. Predicting Glucose Sensor Behavior in Blood Using Transport Modeling: Relative Impacts of Protein Biofouling and Cellular Metabolic Effects. Journal of Diabetes Science and Technology 2013;7(6):1547-1560.

76. Klueh U. Analysis: On the Path to Overcoming Glucose-Sensor-Induced Foreign Body Reactions. Journal of Diabetes Science and Technology 2013;7(2):452-454.

77. Klueh U, Frailey JT, Qiao Y, Antar O, Kreutzer DL. Cell based metabolic barriers to glucose diffusion: Macrophages and continuous glucose monitoring. Biomaterials 2014;35(10):3145-3153.

78. Klueh U, Qiao Y, Frailey JT, Kreutzer DL. Impact of macrophage deficiency and depletion on continuous glucose monitoring in vivo. Biomaterials 2014;35(6):1789-1796.

79. Bian W, Liau B, Badie N, Bursac N. Mesoscopic hydrogel molding to control the 3D geometry of bioartificial muscle tissues. Nat Protocols 2009;4(10):1522-1534.

80. Hansen A, Eder A, Bonstrup M, Flato M, Mewe M, Schaaf S, et al. Development of a Drug Screening Platform Based on Engineered Heart Tissue. Circulation Research 2010 July 9, 2010;107(1):35-44.

81. Sakar MS, Neal D, Boudou T, Borochin MA, Li Y, Weiss R, et al. Formation and optogenetic control of engineered 3D skeletal muscle bioactuators. Lab on a Chip 2012;12(23):4976-4985.

82. Sung JH, Yu J, Luo D, Shuler ML, March JC. Microscale 3-D hydrogel scaffold for biomimetic gastrointestinal (GI) tract model. Lab on a Chip 2012;11(3):389-392.

83. Sisco M, Chao JD, Kim I, Mogford JE, Mayadas TN, Mustoe TA. Delayed wound healing in Mac-1–deficient mice is associated with normal monocyte recruitment. Wound Repair and Regeneration 2007;15(4):566-571.

84. Schutte RJ, Parisi-Amon A, Reichert WM. Cytokine profiling using monocytes/macrophages cultured on common biomaterials with a range of surface chemistries. Journal of Biomedical Materials Research Part A 2009;88A(1):128-139.

85. Vera JC, Reyes AM, Carcamo JG, Velasquez FV, Rivas CI, Zhang RH, et al. Genistein Is a Natural Inhibitor of Hexose and Dehydroascorbic Acid Transport through the Glucose Transporter, GLUT1. Journal of biological chemistry 1996;271(15):8719-8724.

86. Ji G, Zhang Y, Yang Q, Cheng S, Hao J, Zhao X, et al. Genistein Suppresses LPS-Induced Inflammatory Response through Inhibiting NF-kB Following AMP Kinase Activation in RAW 264.7 Macrophages. PLoS ONE 2012;7(12):e53101.

87. Mezei O, Banz WJ, Steger RW, Peluso MR, Winters TA, Shay N. Soy isoflavones exert antidiabetic and hypolipidemic effects through the PPAR pathways in obese Zucker rats and murine RAW 264.7 cells. The Journal of Nutrition 2003;133(5):1238-1243.

88. Tanaka H, Matsumura M, Veliky IA. Diffusion characteristics of substrates in Ca-alginate gel beads. Biotechnology and Bioengineering 1984;26(1):53-58.

89. Melmed RN, Karanian PJ, Berlin RD. Control of cell volume in the J774 macrophage by microtubule disassembly and cyclic AMP. The Journal of Cell Biology 1981;90(3):761-768.

90. Leira F, Louzao MC, Vieites JM, Botana LM, Vieytes MR. Fluorescent microplate cell assay to measure uptake and metabolism of glucose in normal human lung fibroblasts. Toxicology in Vitro 2002;16(3):267-273.

91. Millon S, Ostrander J, Brown JQ, Raheja A, Seewaldt V, Ramanujam N. Uptake of 2-NBDG as a method to monitor therapy response in breast cancer cell lines. Breast Cancer Research and Treatment 2011;126(1):55-62.

92. O'Neil RG, Wu L, Mullani N. Uptake of a Fluorescent Deoxyglucose Analog (2-NBDG) in Tumor Cells. Molecular Imaging and Biology 2005;7(6):388-392.

93. Mannucci PM. Mechanisms, markers and management of coagulation activation. British Medical Bulletin 1994;50(4):851-870.

94. Wolberg AS. Thrombin generation and fibrin clot structure. Blood Reviews 2007;21(3):131-142.

95. Wolberg AS, Campbell RA. Thrombin generation, fibrin clot formation and hemostasis. Transfusion and Apheresis Science 2008;38(1):15-23.

96. Standeven KF, Ariens RAS, Grant PJ. The molecular physiology and pathology of fibrin structure/function. Blood Reviews 2005;19(5):275-288.

97. Weisel JW. The mechanical properties of fibrin for basic scientists and clinicians. Biophysical Chemistry 2004;112(2):267-276.

98. Panilaitis B, Altman GH, Chen J, Jin H-J, Karageorgiou V, Kaplan DL. Macrophage responses to silk. Biomaterials 2003;24(18):3079-3085.

99. Li Y, Schutte RJ, Abu-Shakra A, Reichert WM. Protein array method for assessing in vitro biomaterial-induced cytokine expression. Biomaterials 2005;26(10):1081-1085.

100. Becker ML, Bailey LO, Wooley KL. Peptide-Derivatized Shell-Cross-Linked Nanoparticles. 2. Biocompatibility Evaluation. Bioconjugate Chemistry 2004;15(4):710-717.

101. Chou T-C, Fu E, Shen EC. Chitosan inhibits prostaglandin E2 formation and cyclooxygenase-2 induction in lipopolysaccharide-treated RAW 264.7 macrophages. Biochemical and Biophysical Research Communications 2003;308(2):403-407.

102. Huang H, Pierstorff E, Osawa E, Ho D. Protein-Mediated Assembly of Nanodiamond Hydrogels into a Biocompatible and Biofunctional Multilayer Nanofilm. ACS Nano 2008;2(2):203-212.

103. Harrison SA, Buxton JM, Clancy BM, Czech MP. Evidence that erythroid-type glucose transporter intrinsic activity is modulated by cadmium treatment of mouse 3T3-L1 cells. Journal of biological chemistry 1991;266(29):19438-19449.

104. Perez A, Ojeda P, Ojeda L, Salas Mn, Rivas CI, Vera JC, et al. Hexose transporter GLUT1 harbors several distinct regulatory binding sites for flavones and tyrphostins. Biochemistry 2011;50(41):8834-8845.

105. Ojeda P, Perez A, Ojeda L, Vargas-Uribe M, Rivas CI, Salas M, et al. Noncompetitive blocking of human GLUT1 hexose transporter by methylxanthines

reveals an exofacial regulatory binding site. American journal of physiology-Cell Physiology 2012;303(5):C530-C539.

106. Carletti E, Motta A, Migliaresi C. Scaffolds for tissue engineering and 3D cell culture. 3D cell culture: Springer, 2011. p. 17-39.

107. Wendt D, Riboldi SA, Cioffi M, Martin I. Potential and bottlenecks of bioreactors in 3D cell culture and tissue manufacturing. Advanced Materials 2009;21(32-33):3352-3367.

108. Holt DJ, Grainger DW. Senescence and quiescence induced compromised function in cultured macrophages. Biomaterials 2012;33(30):7497-7507.

109. Klegeris A, McGeer PL. Rat brain microglia and peritoneal macrophages show similar responses to respiratory burst stimulants. Journal of Neuroimmunology 1994;53(1):83-90.

110. Gough DA, Kumosa LS, Routh TL, Lin JT, Lucisano JY. Function of an Implanted Tissue Glucose Sensor for More than 1 Year in Animals. Science Translational Medicine 2010;2(42).

111. Makale MT, Jablecki MC, Gough DA. Mass Transfer and Gas-Phase Calibration of Implanted Oxygen Sensors. Analytical Chemistry 2004;76(6):1773-1777.

112. Leypoldt JK, Gough DA. Model of a two-substrate enzyme electrode for glucose. Analytical Chemistry 1984;56(14):2896-2904.

113. Gough DA, Lucisano JY, Tse PHS. Two-dimensional enzyme electrode sensor for glucose. Analytical Chemistry 1985;57(12):2351-2357.

114. Gough DA, Armour JC, Baker DA. Advances and prospects in glucose assay technology. Diabetologia 1997;40(0):S102-S107.

115. Imtiyaz HZ, Williams EP, Hickey MM, Patel SA, Durham AC, Yuan L-J, et al. Hypoxia-inducible factor 2-alpha regulates macrophage function in mouse models of acute and tumor inflammation. The Journal of Clinical Investigation 2010;120(8):2699-2714.

116. Gordon S. Alternative activation of macrophages. Nat Rev Immunol 2003;3(1):23-35.

117. Cramer T, Yamanishi Y, Clausen BE, Forster I, Pawlinski R, Mackman N, et al. HIF-1-alpha Is Essential for Myeloid Cell-Mediated Inflammation. Cell 2003;112(5):645-657.

118. Peyssonnaux C, Datta V, Cramer T, Doedens A, Theodorakis EA, Gallo RL, et al. HIF-1-alpha expression regulates the bactericidal capacity of phagocytes. The Journal of Clinical Investigation 2005;115(7):1806-1815.

119. Gordon S. Alternative activation of macrophages. Nature reviews Immunology 2003;3(1):23-35.

120. Mantovani A, Sica A, Sozzani S, Allavena P, Vecchi A, Locati M. The chemokine system in diverse forms of macrophage activation and polarization. Trends in immunology 2004;25(12):677-686.

121. Mosser D. The many faces of macrophage activation. Journal of leukocyte biology 2003;73(2):209-212.

122. Deonarine K, Panelli MC, Stashower ME, Jin P, Smith K, Slade HB, et al. Gene expression profiling of cutaneous wound healing. Journal of translational medicine 2007;5(1):11.

123. Crowther M, Brown NJ, Bishop ET, Lewis CE. Microenvironmental influence on macrophage regulation of angiogenesis in wounds and malignant tumors. Journal of leukocyte biology 2001;70(4):478-490.

124. Kelly J, Khan AA, Yin J, Ferguson TA, Apte RS. Senescence regulates macrophage activation and angiogenic fate at sites of tissue injury in mice. The Journal of Clinical Investigation 2007;117(11):3421-3426.

125. Lamagna C, Aurrand-Lions M, Imhof BA. Dual role of macrophages in tumor growth and angiogenesis. Journal of leukocyte biology 2006;80(4):705-713.

126. Calhoun P, Lum J, Beck RW, Kollman C. Performance comparison of the Medtronic Sof-Sensor and Enlite glucose sensors in inpatient studies of individuals with type 1 diabetes. Diabetes technology & therapeutics 2013;15(9):758-761.

Biography

Matthew Thomas Novak was born to noted Fayette County, Pennsylvania celebrity and engineer's engineer, Thomas Novak, and celebrated Italian-American gerontologist and Pittsburgher, Debra Santo-Novak, on July 19th 1985 in Tuscaloosa, Alabama. He lived out the first two years of his life in relative tranquility until the birth of his brother, noted Hall and Oates scholar and LEAN Six Sigma Yellow Belt, Gregory Thomas Novak in 1987. While memorizing the screenplays of "Tommy Boy", and "A Christmas Story," Matthew spent his childhood consuming encyclopedias and watching The Weather Channel, accumulating a wealth of what some may consider useless knowledge that propelled him to victory in the 1999 Alabama State Geography Bee; an award that remains his most decorated professional honor to date.

After graduating from Blacksburg High School in 2003, Matthew matriculated to Duke University and the Pratt School of Engineering. Channeling his father's calling as an engineer and his mother's passion for improving the lives of medical patients, Matthew majored in biomedical engineering, earning his bachelor's degree with departmental distinction in 2007. On the heels of an enlightening and successful undergraduate research experience in the lab of Duke biomedical engineering professor Monty Reichert, Matthew decided to pursue a PhD in Dr. Reichert's lab, and has been sitting in the same desk ever since. In his time at Duke, Matthew authored or co-

authored six peer reviewed journal articles, and presented his research numerous times in such exotic locales as Hartford, Connecticut and Pittsburgh, Pennsylvania.

Motivated by a global health class he took in graduate school, Matthew completed an internship at the World Health Organization in Geneva, Switzerland during the summer of 2012. While there, he worked with his advisor, Dr. Francis Moussy, to investigate methods to increase access of diabetes diagnostics to the developing world, and served as first author for a peer-reviewed manuscript on low cost diagnostic technologies for low and middle income countries.

Matthew has always displayed a curiosity towards all things culinary. As an undergraduate, he began to apply his passion for cooking and held the prestigious position of dishwasher at a restaurant in his hometown before working his way up to prep cook and then line cook. He most recently worked as a part-time cook at Four Square Restaurant, a AAA four diamond restaurant in Durham, N.C., as an outlet from the world of research. Instead of using his time off for traditional vacations, he has done unpaid cooking stints at such world renowned restaurants as Michelin 3-star restaurant, Alinea in Chicago and minibar by José Andrés in Washington, DC to gain exposure to more varied types of cuisine. During his time at Alinea, he kept detailed notes about the inner workings of the restaurant. These notes subsequently turned into a series of articles published by the San Francisco Chronicle entitled "Staging at Alinea." An avid

baker, Matthew was named the 2014 champion bread baker of Durham, North Carolina; an award that he's already planning on defending in the years to come.

Publications:

Novak, M.T., Yuan, F, and Reichert, W.M., "The design of a macrophage embedded fibrin gel as a novel *in vitro p*latform for assessing implantable glucose sensor performance" (in preparation).

Novak, M.T., Yuan, F, and Reichert, W.M., "Predicting glucose sensor behavior in blood using transport modeling: Relative impacts of protein biofouling and cellular metabolic effects," *Journal of Diabetes Science and Technology* 2013; 7(6): 1547-1560.

Novak, M.T., Kotanen, C.N., Carrara S., Guiseppi-Elie, A., Moussy, F.G., "Diagnostic tools and technologies for infectious and non-communicable diseases in low-and-middle income countries," *Health and Technology* 2013; 3(8): 1-11.

Novak, M.T., Yuan, F, and Reichert, W.M., "Modeling the relative impact of capsular tissue effects on implanted glucose sensor time lag and signal attenuation," *Analytical and Bioanalytical Chemistry* 2010; 398(4): 1695-1705.

Anamelechi, C.C., Clermont, E., **Novak, M.T**., and Reichert, W.M., "Dynamic seeding of perfusing HUVECs onto Teflon-AF surfaces adsorbed with RGD-SA and biotinylated fibronectin," *Langmuir*, 2009; 25 (10): 5725-5730.

Novak, M.T., Bryers J.D., and Reichert, W.M., "Biomimetic strategies based on viruses and bacteria for the development of immune evasive biomaterials," *Biomaterials*, 2009; 30(11): 1989-2005.

Kim, D.H., **Novak, M.T.**, et al., "Response of monocytes exposed to phagocytosable particles and discs of comparable surface roughness," *Biomaterials*, 2007. **28**(29): 4231-4239.